

The A-Dependence of Pion Absorption in the Energy Region of the $\Delta(1232)$ Resonance

by

David Cedric Rowntree

A.B. in Physics
Princeton University
June 1988

Submitted to the Department of Physics
in partial fulfillment of the requirements for the degree of
Doctor of Philosophy

at the

MASSACHUSETTS INSTITUTE OF TECHNOLOGY

June 1995

© Massachusetts Institute of Technology 1995

Signature of Author.....

Department of Physics
May 5, 1995

Certified by.....

Robert P. Redwine
Professor of Physics
Thesis Supervisor

Accepted by

.....
Professor George F. Koster
Chairman of the Graduate Committee
MASSACHUSETTS INSTITUTE OF TECHNOLOGY

JUN 26 1995

LIBRARIES

Science

The A-Dependence of Pion Absorption in the Energy Region of the $\Delta(1232)$ Resonance

by

David Cedric Rowntree

Submitted to the Department of Physics
on May 5, 1995, in partial fulfillment of the
requirements for the degree of
Doctor of Philosophy

Abstract

The absorption of π^+ at 118, 162, and 239 MeV on ^3He , ^4He , N, and Ar has been studied using the Large Acceptance Detector System (LADS) at the Paul Scherrer Institute in Villigen, Switzerland. LADS has a solid angle coverage of over 98% of 4π steradians and an energy threshold of less than 20 MeV for protons, making it an almost ideal detector for studying multi-nucleon final states following pion absorption. The total absorption cross sections at the three energies are, in millibarns: ^3He - 24.8 ± 2.1 , 24.2 ± 3.1 , and 8.1 ± 2.7 ; ^4He - 49.5 ± 3.1 , 48.0 ± 3.8 , and 21.9 ± 4.1 ; N - 181.6 ± 9.9 , 163.4 ± 10.5 , and 107.0 ± 9.9 ; Ar - 393.2 ± 20.6 , 366.1 ± 21.8 , and 281.8 ± 21.1 . With the exception of ^3He , these are the most accurate measurements reported to date. In addition, the breakup into channels with different numbers of energetic final state nucleons has been determined. The average number of nucleons participating in the absorption reaction has been found to increase more slowly with A than previously reported. Differential spectra show clear signatures of small contributions from initial state interactions, and indicate the presence of at least some final state interactions.

Thesis Supervisor: Robert P. Redwine
Title: Professor of Physics

Acknowledgements

In any collaboration as large as LADS, many people are involved in each facet. This was certainly true for the work behind my thesis, which had essential contributions from many members of the collaboration. The construction and operation of the detector, the development of the analysis tools, the insights into the physics, and the critical discussions all depended on the varied individual strengths and uniform enthusiasm of the members. They all deserve thanks.

Special mention must be made of the few who had the most influence on my work. Quentin Ingram provided leadership, experience, and a willingness to constructively argue on almost any topic. Bob Redwine, my advisor, exuded optimism whenever my outlook turned dark. Art Mateos was an inspiration to all with his tireless search for new ways to look at the data, and Nik Gregory always recharged my batteries when I wound down during the middle of the day.

The person I worked most closely with was Kevin Wilson. From showing me the partially built detector the first time I visited PSI, to endless discussions of fine points in the data analysis, he was always kind, courteous, dedicated, and intelligent. He will always have my respect and my friendship.

Outside of the LADS collaboration, there are the myriad of people who provide the framework that defines one's life. These include: Julie Kyle, my girl friend during my early years at MIT; Wilson Fong and Marla Dowell, co-workers who always entertained; Mike Klein and Peter Lieberman, bridge partners and frequent hotelmates; Debbie Ulbrich and Suzanne Hamby, my dance teachers; and Anna Mayor, my dance partner and good friend whose company I enjoy immensely.

My formative years were guided by my parents, Peter and Ellen Rowntree, and my sister, Bis. They have continued to provide support during the years since I have left home, and show an interest in my life that is phenomenal. I even believe that my mother intends to read this thesis - a true labor of love.

Finally, the person who has provided me the most comfort, support, excitement, and elation during the past two years is Christina Haage. The burdens she was willing to shoulder during the late stages of my graduate career were a continual source of surprise, none surpassing the fact that she has already read this thesis in its entirety. Soon she will be Christina Rowntree. No more needs to be said.

Contents

1	Introduction	17
1.1	Early Absorption Experiments	22
1.2	The Development of Two-Nucleon Absorption (2NA) as the Dominant Absorption Process	24
1.3	The Move to the Meson Factories	30
1.4	Recent Developments: The Eighties and Nineties	38
2	The LADS Detector	51
2.1	Design Motivation and Goals	51
2.2	Overview	53
2.3	Scintillators and PMT's	54
2.3.1	Cylinder	56
2.3.2	Endcaps	58
2.3.3	Readout	60
2.4	Multi-Wire Proportional Chambers (MWPC's)	61
2.5	Target	65
2.6	The Pion Beam: Creation and Definition	67
2.7	Trigger	71
2.8	Data Acquisition and Storage	75
3	Analysis Software and Performance	77
3.1	Particle Reconstruction	80
3.2	Trajectory Reconstruction	81
3.3	Calibration	83
3.4	Particle Identification	86
3.5	Energy Loss	89

4	Particle Multiplicities	94
4.1	Separation of Events Originating in the Target	95
4.2	Modifications to the Experimental Definition of a Particle	97
4.3	Charged Pion Identification	98
4.3.1	Additional E-TOF Cut	99
4.3.2	dE/dx for Punchthrough Particles	99
4.3.3	PID for "Neutral" Charged Particles	99
4.4	SCX Subtraction	102
4.5	Reaction Corrections	110
4.6	Pion Contamination	114
4.7	Beam Normalization	117
4.8	Number of Target Scatterers	122
4.9	Dead Time and Prescale Factors	123
4.10	Uncertainties	124
4.11	Results: Charged Multiplicities	126
5	Neutrons and Deuterons	129
5.1	Neutron Identification	129
5.1.1	Defining a Detected Neutron	130
5.1.2	Obtaining the Detected Neutron Cross Sections	132
5.1.3	The Neutron Detection Efficiency	136
5.1.4	Correcting for the Neutron Efficiency	139
5.2	Detected Deuterons	141
6	Discussion and Conclusions	147
6.1	Summary of Acceptance Limitations	147
6.2	The Results of the Multiplicity Analysis	149
6.3	Differential Investigations	157
6.3.1	Total Detected Energy	158
6.3.2	The Search for ISI	165
6.3.3	The Search for FSI	175
6.4	Conclusions	178

List of Figures

1-1	The energy dependence of the total $\pi^+ - {}^{12}\text{C}$ cross section and its breakup into channels; from reference [1].	19
1-2	The energy dependence of various pion scattering processes; from reference [2].	20
1-3	The energy distribution of <30 MeV protons following the absorption of stopped π^- in photographic emulsion. The dashed line shows the expected distribution from evaporation. The figure is from reference [3] as reproduced in [4].	23
1-4	The total cross section for the absorption of π^+ on ${}^2\text{H}$. The measurements shown all pre-date 1960, but the curve is a parameterization of the world's data in 1990.	26
1-5	The energies of neutrons detected after the absorption of stopped π^- on ${}^{12}\text{C}$ from reference [5]. The insert shows the agreement between the low energy spectra and the predicted $E^{5/11}$ dependence from evaporation.	28
1-6	The Treiman-Yang angle for the absorption of 76 MeV π^+ on ${}^4\text{He}$ from reference [6]. The data were separated into three regions of the missing mass, as indicated in the figure. The distributions are also shown for the recoil momentum less than 110 MeV/c. The dashed lines result from phase space simulations.	31
1-7	The missing mass distribution for the reaction ${}^6\text{Li}(\pi^+, pp)$ from reference [6]. The lower figure has the restriction that the recoil momentum is less than 110 MeV/c. The dashed curves are the result of phase space simulations.	32
1-8	Missing mass distributions for the absorption of 76 MeV π^+ on five targets from reference [6]. The right side has the restriction that the recoil momentum is less than 110 MeV/c.	34
1-9	The charged prong multiplicity after the absorption of 130 MeV π^+ on ${}^{12}\text{C}$ from reference [7].	35
1-10	The spectra of detected γ -rays following the absorption of π^- on ${}^{31}\text{P}$ from reference [8]. The upper curve is for 0 MeV pions, and the lower is for 60 MeV pions. The nuclei corresponding to the individual peaks is identified.	36
1-11	The energies of protons from the absorption of 100 and 220 MeV π^\pm on ${}^{62}\text{Ni}$ from reference [9]. The top spectra were measured at 45° and the bottom at 94° . The π^- results have been multiplied by a factor of three.	37

1-12	A rapidity plot for the absorption of 220 MeV π^- on ^{181}Ta from reference [10].	38
1-13	The A-dependence of the average number of nucleons participating in the absorption of π^+ (solid circles) and for π^- (open circles) from reference [10]. The results are averaged over the incident pion energies of 100, 160, and 220 MeV.	39
1-14	The A-dependence of the absorption cross section for π^+ around 165 MeV. The diamond is from Neganov and Parfenov [11], the circle is from Baumgartner <i>et al.</i> [12], and the triangles are from Ashery <i>et al.</i> [1].	40
1-15	A Dalitz plot for the absorption of stopped π^- on ^3He from reference [13]. Region (A) corresponds to nn-FSI, (B) and (F) to $\pi^-pp \Rightarrow pn$ QFA, (C) and (E) to pn-FSI, and (D) to $\pi^-pn \Rightarrow nn$ QFA.	42
1-16	The angular distribution of an outgoing proton from the reaction $^{16}\text{O}(\pi^+,pp)$ at 165 MeV with the other proton detected at 120° [14]. The differential cross section is fit by the sum of two gaussians.	43
1-17	The angular distribution of a proton when another was detected at 117° after the absorption of 120 MeV π^+ on ^3He [15]. The distribution labeled MC is the results of a three-body phase space simulation.	44
1-18	The energies of protons at 8° after the absorption of 242 MeV π^+ on ^{12}C from reference [16]. The arrow shows the energy that a proton would have after a free scattering process.	47
1-19	In plane angular distributions for a proton with the other detected at $+50^\circ$ after the reaction $^{16}\text{O}(\pi^+,2p)^{14}\text{N}$ with 116 MeV pions from reference [17]. The various measurements are to specific nuclear final states with the specified excitation energies and angular momenta. The dotted line at -108° shows the quasi-free angle.	48
2-1	The LADS detector, adapted from reference [18].	53
2-2	The downstream endcap.	59
2-3	Three views of the MWPC's are shown. The left-most shows the position of the chambers in the detector. The top-right shows an end-on view of a slice through a chamber, and the bottom-right shows the orientations of the cathode strips and anode wires.	63
2-4	The high pressure gas target [19].	66
2-5	The πM1 channel at PSI.	68
2-6	A diagram of the beam defining scintillators.	69
2-7	A timing diagram for the beam defining electronics [20].	70
2-8	A diagram of the trigger electronics, from reference [19].	73
2-9	A diagram of the data acquisition system.	75

3-1	A flow of the major components of the LADYBIRD data analysis package. . . .	78
3-2	MWPC reconstruction of the position along the z-axis at which a reaction occurred.	84
3-3	MWPC reconstruction of the position in the x-y plane at which a reaction occurred in a 20 cm slice in z around the center of the target.	84
3-4	An E-dE/dx plot for cylinder particles with MWPC trajectory information. The data are from 239 MeV π^+ incident on N. The curves show the tests used for PID.	87
3-5	E-dE/dx plots following the interaction of 239 MeV π^+ 's with N. The top figure shows the calculation for the cylinder without using MWPC data, the middle figure is for the endcaps with MWPC data, and the bottom figure is for the endcaps without MWPC information.	88
3-6	E-TOF plots following the interaction of 239 MeV π^+ 's with N. The top left figure shows the calculation for the cylinder using MWPC information, the top right is for the cylinder without using the MWPC's, the lower left figure is for the endcaps with MWPC data, and the lower right figure is for the endcaps without MWPC information. The hyperbolic lines show the cuts used to separate pions, protons, and deuterons.	90
4-1	The too-fast cut is shown as the lower curve on each figure; the upper is the normal PID cut. The data are from the interaction of 239 MeV π^+ 's with N, with pions identified by the basic PID machinery already removed. The top left figure shows the calculation for the cylinder using MWPC information, the top right is for the cylinder without using the MWPC's, the lower left figure is for the endcaps with MWPC data, and the lower right figure is for the endcaps without MWPC information.	100
4-2	The punchthrough cut is shown on each figure as the lower curve; also shown is the normal E-dE/dx cut as the upper curve. The data are from the interaction of 239 MeV π^+ 's with N, with pions identified by the basic PID machinery already removed. The top figure shows E-dE/dx for the endcaps using MWPC information, and the lower is for the endcaps without using the MWPC's.	101
4-3	The reduced TOF spectrum for neutrals detected after the interaction of 162 MeV π^+ 's with Ar. The cut used to separate γ 's from neutrons is shown as a dotted line.	103
4-4	The spectrum of detected light for photons after the interaction of 162 MeV π^+ 's with Ar. The cut used to separate evaporation γ 's from SCX γ 's is shown as a dotted line.	105
4-5	The kinetic energy of a charged particle when only one charged particle was detected.	109

4-6	The proton reaction correction factor as a function of proton energy for events with MWPC information. The dotted line is the fit used to correct the data. . .	111
4-7	The proton reaction correction factor as a function of proton energy for events without MWPC information. The dotted line is the fit used to correct the data. . .	112
4-8	The total detected light of absorption events selected by the MWPC's following the interaction of 239 MeV π^+ 's with ^3He . The line is an exponential fit to the reaction tail, used to determine the pion contamination.	113
4-9	S_{beam} 's TDC spectrum for beam events at 118 MeV incident pion energy.	118
4-10	S_{beam} 's ADC spectrum for events with an incident pion energy of 118 MeV. The dotted line shows the cut separating "good" beam pions from "bad" beam pions.	119
4-11	The ratio of the number of events with a vertex within 2 cm of the beam axis to the number of events within 4 cm of the beam axis, used to determine the fraction of the π^+ beam which misses the target. The data are for a 162 MeV beam and a ^4He target.	121
5-1	The minimum opening angle between the trajectory of a detected neutron and the missing momentum is shown. The data are from the absorption of 239 MeV π^+ 's by ^4He . The dotted line shows the 30° cutoff used when calculating the efficiency.	137
5-2	The calculated neutron detection efficiency is shown as a function of the neutron's reconstructed kinetic energy. The dotted line shows the value of the efficiency used in the analysis.	138
5-3	The calculated neutron detection efficiency is shown as a function of the neutron's theta, for neutrons with a kinetic energy greater than 40 MeV. The dotted line shows the value of the efficiency used in the analysis.	140
5-4	The missing mass calculated from the two known protons for a set of <i>ppd</i> events with some <i>pppn</i> contamination. The curves and lines are described in the text. . .	145
6-1	The total detected cross sections are shown as a function of A. The triangles are for an incident pion energy of 118 MeV; the circles, 162 MeV; and the squares 239 MeV. Uncertainties are included, but are frequently smaller than the size of the symbol.	150
6-2	A comparison between the total absorption cross sections from this work and those from previous experiments in the vicinity of 165 MeV. The stars show the current results, the diamond is from Neganov and Parfenov [11], the circle is from Baumgartner <i>et al.</i> [12], and the triangles are from Ashery <i>et al.</i> [1].	151

6-3	The total absorption cross sections are shown as a function of the incident π^+ energy. The solid triangles are for ^3He , the circles for ^4He , the squares for N, and the open triangles for Ar. The curves are a parameterization of the ^2H cross section [21].	153
6-4	The detected charge multiplicities following the absorption of π^+ are shown in millibarns.	154
6-5	The average number of final state energetic nucleons are shown as a function of A.	156
6-6	The summed energies of all charged particles.	159
6-7	The energy of a charged particle when only one charged particle was detected.	160
6-8	The summed energies of two charged particles when no other charged particles were detected.	162
6-9	The summed energies of three charged particles when no other charged particles were detected.	163
6-10	The missing momentum calculated from all of the detected charged particles.	164
6-11	The relationship between the momenta and polar angles of the protons for events in which three protons are detected, with each $T_p > 30$ MeV. The incident π^+ energy is 118 MeV.	166
6-12	The relationship between the momenta and polar angles of the protons for events in which three protons are detected, with each $T_p > 30$ MeV. The incident π^+ energy is 162 MeV.	167
6-13	The relationship between the momenta and polar angles of the protons for events in which three protons are detected, with each $T_p > 30$ MeV. The incident π^+ energy is 239 MeV.	169
6-14	The relationship between the momenta and polar angles of the protons for events in which three protons are detected, with each $T_p > 30$ MeV. In addition, $E_{\text{miss}} < 75$ MeV. The incident π^+ energy is 118 MeV.	170
6-15	The relationship between the momenta and polar angles of the protons for events in which three protons are detected, with each $T_p > 30$ MeV. In addition, $E_{\text{miss}} < 75$ MeV. The incident π^+ energy is 162 MeV.	171
6-16	The relationship between the momenta and polar angles of the protons for events in which three protons are detected, with each $T_p > 30$ MeV. In addition, $E_{\text{miss}} < 75$ MeV. The incident π^+ energy is 239 MeV.	173
6-17	An illustration of the definition of the pseudo-invariant mass.	174
6-18	The square of the pseudo-invariant mass is shown for events with three detected protons, each over 30 MeV.	176
6-19	The momentum of a proton between 130° and 140° when there are three protons detected, each is over 30 MeV, and $E_{\text{miss}} < 75$ MeV.	177

6-20 The opening angles between each of the three possible pairs of protons when there are three detected protons, each over 30 MeV, and $E_{\text{miss}} < 75$ MeV. 179

List of Tables

2.1	LADS's characteristics.	54
2.2	Relevant MWPC parameters, from reference [20].	64
3.1	All thicknesses are given for a trajectory normal to the beam line. Adapted from reference [20].	92
4.1	The magnitudes of the total detected SCX cross sections (mb) are given, broken up by the number of charged particles detected. The requirement exists that at least one charged particle be detected in LADS, with the restrictions on the acceptance described in the text.	108
4.2	The cross sections for detecting a charged pion with the acceptance limitations described in the text are given in millibarns.	115
4.3	The cross sections for each charge multiplicity are given in millibarns. All corrections have been applied as described in the text. No corrections have been made for missing acceptance. Both systematic and statistical uncertainties are included.	127
4.4	The MWPC and no-MWPC components of the absorption cross section (mb) are given as a fraction.	128
5.1	Detected neutron multiplicities (mb). All corrections described in the text have been made with the exception of that for the neutron detection efficiency.	134
5.2	Detected neutron multiplicities (mb). All corrections described in the text have been made with the exception of that for the neutron detection efficiency.	135
5.3	An illustration of the correction for the neutron detection efficiency. The data are from the absorption of 162 MeV π^+ 's on Ar with two charged particles detected in the final state. Column (a) shows the detected multiplicities, and column (b) has been corrected for the neutron detection efficiency as described in the text. Columns (c) through (f) illustrate the impreciseness of this procedure. (c) and (d) have been calculated with $\epsilon_n = \epsilon_n \pm \sigma$, or 32% and 40%. (e) and (f) show the effect of changing the detected 3N cross section by ± 0.1 mb.	141

5.4	The neutron multiplicities in millibarns, after the correction for the neutron detection efficiency has been applied.	142
5.5	The neutron multiplicities in millibarns, after the correction for the neutron detection efficiency has been applied.	143
5.6	Multiplicities in millibarns of final states including a deuteron, before corrections for mistaken PID have been applied.	144
5.7	The multiplicities (mb) of final states including a deuteron after all corrections described in the text have been applied.	146
6.1	Very rough estimates of the fractional contribution of ISI to the strength with three detected protons, each above 30 MeV, and $E_{\text{miss}} < 75$ MeV.	172

Chapter 1

Introduction

The existence of the pion was first postulated in 1935 by Yukawa [22] as an element in his field theory for the strong nuclear force. As the particle is exchanged between nucleons in this theory, several of its characteristics are determined. It must be a boson since, among other reasons, the number of pions could not be a conserved quantity. Also, its approximate mass was determined by the short range of the nuclear strong force. The strong force was known to have a range of about 1.5 fm, and the Heisenberg uncertainly principle can be used to determine the approximate mass:

$$Et \approx \frac{Ed}{c} \approx \hbar \implies E \approx 130 \text{ MeV}$$

As this mass is intermediate between that of the electron and the proton, these particles became known as mesons, which means “of middle-weight.”

During the next year experimenters discovered a particle of mass 105 MeV in cosmic rays and associated it with Yukawa’s pion [23]. A decade later, in 1946, it was shown that this particle did not interact strongly, and thus could not be the pion [24]. It turned out to be a lepton, but the association with the pion was already strongly formed and it was named the mu-meson, or muon for short. The search began again.

In 1947, another cosmic ray particle of approximately the right mass was observed [25]. It was clearly separated from the muon as its decay into the latter particle was observed in photographic emulsion experiments. This particle was identified as the pion. The pion had remained successfully hidden for so long because most of the cosmic ray pions decay into muons in the upper atmosphere. The experiments which finally discovered it took place at the top of a mountain.

In the next several years various properties of the pion were measured. It has three charge states (+1,0,-1) and thus an isospin of one. The mass of the charged pions is 139.57 MeV and of the neutral pion is 135.0 MeV. Its spin was determined by applying the law of detailed balance to the reaction $p+p \Rightarrow \pi^+ + d$ and its inverse. The ratio of these two cross sections should be proportional to $(2S_\pi + 1)$ multiplied by known factors. Measurements in the early 1950's used this fact to determine that the charged pion spin is 0 [26, 27]. That the neutral pion has the same spin was determined from the fact that in high energy nucleon-nucleon collisions, the three pion types are produced in equal numbers.

The parity of the pion was determined when it was discovered by spectroscopic analysis that the reaction $\pi^- + d \Rightarrow n + n$ occurs from an $L=0$ state. The two neutrons thus have total spin one, the Pauli principle tells us that their orbital angular momentum is one, and the parity of the final state is odd. The parity of the initial state, and thus the pion, is odd as well. The charged pions decay via the weak force primarily into a muon and a neutrino with a lifetime of 2.6×10^{-8} s. The neutral pion decays via the electromagnetic force primarily into two photons, with a lifetime of 8.7×10^{-17} s.

A consequence of the hadronic and bosonic natures of the pion is that these particles can be created and destroyed in strong nuclear interactions. In the latter case, the pion is said to be "absorbed". Figure 1-1 shows the total cross section for $\pi^+ - {}^{12}\text{C}$ and its breakup into various channels. Two things are immediately apparent: First, the absorption cross section constitutes a significant fraction of the total. Second, the absorption cross section has a resonant behavior peaking in the vicinity of 165 MeV. The position of this resonant peak is consistent with the excitation of a $\Delta(1232)$ in the nucleus. The $\Delta(1232)$ is the first excited state of the nucleon. It is a $J^\pi = 3/2^+$ isospin 3/2 particle. It has a mass of 1232 MeV with a width of 115 MeV. Its primary decay path is to πN with a mean life on the order of 10^{-23} s. In the energy region where the Δ is excited, it dominates the π -nucleon interaction. This fact has some readily calculable consequences. For example, Clebsch-Gordon coefficients can be used to calculate the relative importance of processes which are different only in isospin. Figure 1-2 shows the cross sections for $\pi^+ p \Rightarrow \pi^+ p$, $\pi^- p \Rightarrow \pi^- p$, and $\pi^- p \Rightarrow \pi^0 n$. The solid lines show the calculated contribution from the Δ -resonance, and the 9:1:2 ratio predicted from the Clebsch-Gordon coefficients is closely followed.

The free absorption reaction $\pi + N \Rightarrow N$ is forbidden by energy and momentum conservation, and thus other particles need to be present for an absorption to occur. Absorption on a single nucleon is allowed in the presence of the other nucleons of a nucleus, but the large momentum required for the absorbing nucleon (>500 MeV/c), in comparison to typical Fermi-momenta,

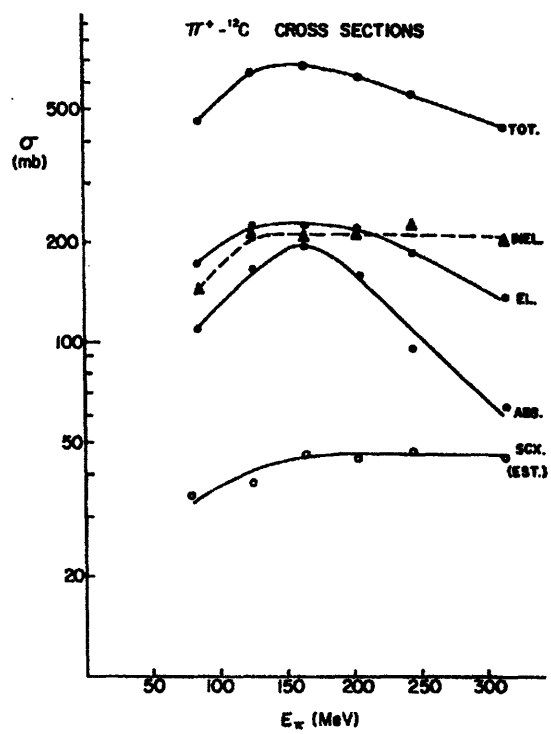


Figure 1-1: The energy dependence of the total $\pi^+ -^{12}\text{C}$ cross section and its breakup into channels; from reference [1].

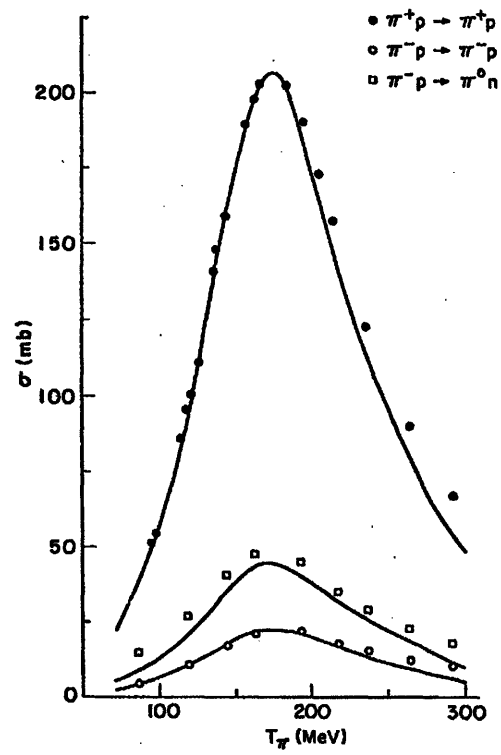


Figure 1-2: The energy dependence of various pion scattering processes; from reference [2].

means that this reaction is suppressed. Thus, the smallest nuclear system that is significant for pion absorption consists of two nucleons. The only bound two nucleon system is the deuteron, and studying absorption on the deuteron has played a major role in determining the properties of the absorption process. As more nuclei are added to the absorbing system, the possibility arises that more than two nucleons play a role in the absorption process. Therefore the characteristics of absorption on heavier nuclei could prove to be significantly different than for absorption on deuterium.

The LADS detector was designed and built at the Paul Scherrer Institute (PSI) in Villigen, Switzerland, to study cases in which more than two nucleons share the energy released by the absorption of a pion. It has close to 4π solid angle coverage with enough granularity to detect the outgoing nucleons separately, energy and angular resolution sufficient to determine the energy and momentum of the residual system, and the ability to detect neutrons in the final state. There have been three experimental runs: A detector tune-up run in 1989; the first data run in 1991 which measured absorption on ^2H , ^3He , ^4He , N, and Ar at 118, 162, and 239 MeV; and a second data run in 1993 which added Xe to the targets and 70 and 331 MeV to the energies. Emphasis was placed on the helium isotopes to determine the effects of adding an additional one or two nucleons to the essentially understood two nucleon absorbing system.

This thesis will present results from the author's area of primary responsibility, namely absorption on N and Ar at 118, 162, and 239 MeV, with comparisons made to results on ^3He and ^4He .

Pion absorption has proven to be a difficult field of study, prompting one author almost to despair in 1975: "Work in pion absorption is like fighting the mythological Hydra. This beast has many heads, each of which, if cut off, grows back as two. For pion absorption: each new experiment creates more problems than it solves [28]." Progress in the last 20 years has answered some of these questions, but has not disappointed, as it has continued to raise many more. To set the scene for the present work, the history of experiments in pion absorption is reviewed below. Where experiments using pions in the energy range considered in this work are available, experiments using stopped pions, or pions with other energies, are ignored. Also, considerations of space and effort will restrict the descriptions of experiments before 1980 to being less than complete, with more attention given to the last 15 years.

1.1 Early Absorption Experiments

Given the number of questions still open in pion absorption, it is surprising how fast initial progress was made in the field. In a book published in 1952, Marshak [4] reviews the first five years of study of the properties of the pion, including pion absorption. The difficulty of experiments in that period was the lack of stable, high intensity pion beams. There were pion beams with $T_\pi \leq 100$ MeV available at the Columbia and Berkeley cyclotrons, and at the Cornell synchrotron. More energetic pions were available in cosmic ray experiments at high altitudes, but the energy and purity of these "beams" were not well known in this case. Therefore it was much harder to separate pion absorption from other reactions, and the experiments using these "natural" pions tended to look for characteristics like total elastic and total inelastic reaction cross sections.

Because of the low intensities of the available beams, and the relatively small cross section for the absorption of pions in flight, many of the early experiments were performed with stopped pions. A low energy π^- is captured by a nucleus in a high energy shell. Through a combination of x-ray and Auger emission, the pion de-excites to the K or L shell of the nucleus. At this point the overlap between the pion and the nuclear wave functions is large enough to allow hadronic interactions, and the pion is absorbed. The majority of experiments stopped the pion in a photographic emulsion, which was used to identify and measure the energies of the charged particles emitted by the "star" created by an absorption. The absorbing nucleus was identifiable as being among the light (C, O, or N) or heavy (Br or Ag) nuclei present in the emulsion.

Among the early experiments were Menon *et al.* [3] and Adelman [29] which examined 2500 and 1500 stars respectively. Their data showed that a star has an average of 1.6 charged "prongs", or energetic charged particles, associated with it. Since absorption of π^- on a pn pair would lead to two neutrons, and on a pp pair would lead to only one proton, the implication was that more than two nucleons were participating in the absorption. However, Menon *et al.* also measured the energy distribution of final state protons under 30 MeV. The results, shown in figure 1-3, fit the expected distribution from a statistical theory of evaporation in which the residual nucleus is left in a highly excited state which decays via nucleon emission. Now, evaporation could either be a direct result of the absorption process if the entire nucleus plays a role sharing the energy equally, or it could be a side effect, resulting from a spectator nucleus left in a highly excited state after absorption on a small subset of its nucleons. Thus, the 1.6 prongs may not be a true indication of the number of particles directly involved in the process.

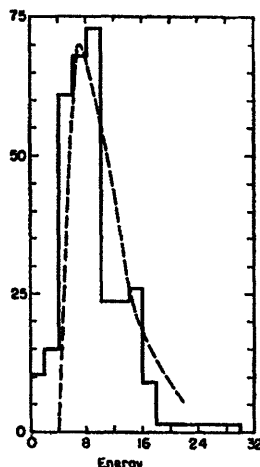


Figure 1-3: The energy distribution of <30 MeV protons following the absorption of stopped π^- in photographic emulsion. The dashed line shows the expected distribution from evaporation. The figure is from reference [3] as reproduced in [4].

In about 10% of the events a proton of over 30 MeV was observed by Adelman. The statistics available were poor, as was the energy resolution of the protons, so it is difficult to draw clear conclusions. In a significant fraction of the events, however, these protons carried away a kinetic energy equal to about one-half of the rest mass of the pion, possibly indicating absorption on a pp pair.

Another interesting result of these early experiments was that the number of energetic α particles emitted from the light nuclei, C, N, and O were about equal to the number of energetic protons. On the heavier emulsion nuclei, there were only a third as many α 's as protons. This could also be due to evaporation and the difference in potential barriers of the nuclei.

Another line that early experiments took was the search for high-energy γ 's after stopped π^- absorption. The goal was to determine the relative importance of hadronic absorption in which the energy is shared by two or more nucleons, radiative absorption where the energy is mainly carried by a single photon, and what was called mesic absorption where the π^- undergoes a single-charge exchange reaction with a neutron and the resulting π^0 decays into two (usually) photons. Panofsky *et al.* [30] determined that mesic and radiative were about equally likely for absorption on H. Mesic absorption was insignificant for absorption on ^2H , while hadronic was about twice as likely as radiative. By ^4He , the only significant absorption channel is the hadronic.

There were also some experiments measuring pion absorption in flight at the accelerator facilities mentioned above. The first measurements of cross sections for π^+ absorption on the deuteron were performed by Clark *et al.* [26] and by Durbin *et al.* [27] in 1951. The authors took data using scintillation counters to identify the outgoing protons at a few angles, and then extended over unmeasured regions by using distributions determined from π^+ production in pp collisions. These experiments, as mentioned above, were used to determine the spin of the pion.

Bernardini *et al.* [31] measured π^- absorption in photographic emulsions up to 110 MeV. The authors determined that the cross section was increasing with energy in this regime, and also that it was increasing in relative importance to elastic scattering. Bernardini and Levy [32] measured the absorption of 70 MeV π^+ 's in photographic emulsion. The average number of charged prongs for the π^+ absorption was 3.2, in comparison to 1.5 for π^- at the same energy. Interestingly, there was at least one proton with more than 30 MeV kinetic energy in 85% of the stars, but there were two or more in only 30%. This is a strong indication that more than two nucleons are usually involved in the reaction process.

Fowler *et al.* [33] performed a diffusion cloud chamber experiment studying the interaction of 60 and 105 MeV pions with hydrogen and helium. The authors were able to use some general arguments about the expected characteristics of absorption to separate this channel from single charge exchange. They estimated absorption cross sections of 15 and 20 mb at 60 and 105 MeV respectively, with no estimation of uncertainties.

There is one result in this period not specifically measuring the absorption process which deserves mention. Along with Bernardini *et al.* [31], Bradner and Rankin [34] found that the A -dependence of the total cross section for strong pion-nucleus interactions is close to geometrical. That is, the nucleus acts like a black disk to the pion—if it passes through the boundaries, a hadronic interaction of some type will occur. The implication is that the mean free path of the pion in the nucleus is small in comparison to the nuclear dimensions.

1.2 The Development of Two-Nucleon Absorption (2NA) as the Dominant Absorption Process

The next period we will discuss runs from about 1953 through 1969. Reviewed by Koltun [35], these seventeen years saw an increase in the accuracy of the experiments. Bubble and cloud

1.2. The Development of Two-Nucleon Absorption (2NA) as the Dominant Absorption Process 25

chamber experiments were performed with better statistics and improved energy resolution. Also, counter experiments emphasizing specific final states became more popular. Many of the experiments were still performed using stopped π^- as the available pion beams still had low fluxes.

The most significant indication as to the nature of the reaction process came through the study of the deuterium absorption cross sections. The work begun by Clark *et al.* [26] and Durbin *et al.* [27] mentioned previously was carried on through the 1950's. Total cross sections were measured by Stadler [36] in 1954 at 91 and 114 MeV; by Cohn [37] in 1957 at 144 MeV; by Sachs *et al.* [38] in 1958 at 38 and 61 MeV; and by Neganov and Parfenov [11] also in 1958 at 174, 200, 227, 262 and 307 MeV. These measurements are shown in figure 1-4. They demonstrate the existence of a resonance in the energy spectra with a peak at about 140 MeV. More experiments have since been performed and much more data collected, especially in the vicinity of the peak of the resonance. Ritchie [21] has parameterized the world's data up to 1990 and the result is shown as the solid curve in the figure. Of the early experiments, Neganov and Parfenov also measured differential cross sections of sufficient accuracy to show that they can be expressed as $A+B\cos^2\theta$.

The implication of the peaking around 140 MeV is that the $\Delta(1232)$ resonance, the first excited state of the nucleon mentioned above, plays a dominant role in the absorption process in this energy region. Spin and parity arguments require that a pion be absorbed from a relative angular momentum $L=1$ state, which is consistent with the differential cross sections reported above. Thus, the picture emerged in the 1950's that the pion was absorbed on the deuteron from an $L=1$ state, forming a ΔN pair which subsequently decayed into two nucleons. Away from the resonance region—for example, π^- at rest—the reaction did not tend to proceed through a Δ , and $L=0$ absorption would be possible. Thus, experiments from the different energy regions are not directly comparable (although they can shed light on each other) as different underlying mechanisms are involved.

The late 1950's, into the beginning 1960's, saw several results on the number of energetic charged particle prongs after a star resulting from pion absorption. The results were at best qualitative however, and even the qualitative results showed significant variations between experiments. In 1956, Demur *et al.* [39] measured stopped π^- absorption in photographic emulsions. They found that in about 35% of the events there were no energetic charged particles. For the events with such particles, the average number of prongs found was three for absorption on C, N, or O, and one for absorption on Ag or Br. The authors also estimated that for about

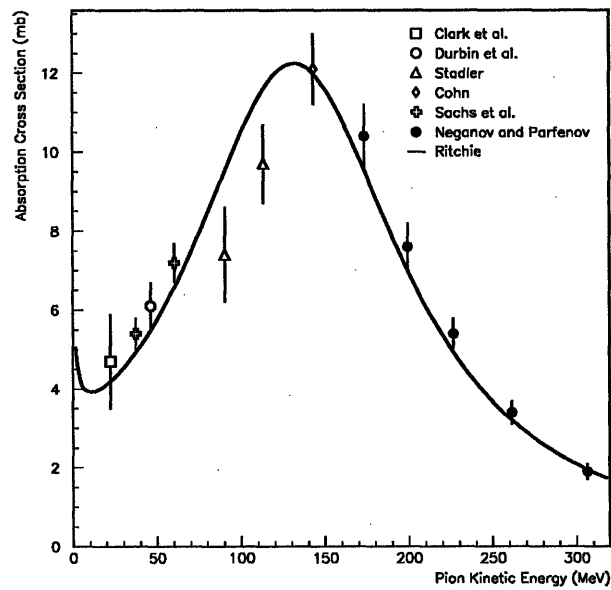


Figure 1-4: The total cross section for the absorption of π^+ on ^2H . The measurements shown all pre-date 1960, but the curve is a parameterization of the world's data in 1990.

1.2. The Development of Two-Nucleon Absorption (2NA) as the Dominant Absorption Process 27

20% of the absorption events on the light nuclei there are no final state particles heavier than an α , *i.e.*, complete breakup of the nucleus occurs.

Azimov *et al.* [40] in the same year found the same average numbers of prongs as Demur *et al.*, although the experiments differed in the distribution of the number of prongs. Ammiraju and Lederman [41] in 1956 found that complete breakup occurs for C and N approximately 30% of the time. A later but similar experiment by Fedotov [42] in 1965 found the significantly different value of 60%. Another experimental result which has undergone several fluctuations is the branching ratio for the reaction $\pi^- + {}^4\text{He} \Rightarrow t + n$. The first measurement of this channel determined a ratio less than 2% [41]. It then moved as high as 35% [43] before settling at just under 20% [44, 45].

Studies of the interaction of pions with helium continued with diffusion cloud chambers, although difficulties in the separation of absorption and single charge exchange limited the accuracy with which these experiments could determine absorption cross sections. In 1960, Kozodaev *et al.* [46] studied these interactions at 273 and 330 MeV. They estimated a range of between 8 and 21 mb for the magnitude of the absorption of π^+ at 273 MeV. They also examined the energies of the outgoing protons and concluded that absorption on a deuteron pair dominates the process. Budagov *et al.* [47] examined the interactions of π^- at 153 MeV. They estimated an absorption cross section of 61 mb.

In the 1960's, experimental techniques improved to the point that statistically significant measurements of single particle energy spectra became possible. One of the most complete experiments in this period was that of Anderson *et al.* [5] (1964) who used time-of-flight counters to measure neutron energies from stopped π^- absorption on C, Al, Cd, Pb, and U. In addition to measuring the energy spectra, this experiment also found that the average number of neutrons with energies ≤ 2 MeV varied from 2.8 for C to 5.0 for U. In the previous section the process of evaporation was mentioned. The nucleus is left in a highly excited state which de-excites through nucleon emission, mainly neutrons because of the Coulomb barrier. The energy spectra of the evaporation neutrons can be calculated by statistical theory, and this had been done by Le Couteur [48, 49] in the early 1950's. When the experimental neutron energies were compared to this theory, as in figure 1-5, it was found that the low energy neutrons had the predicted energy dependence. The calculation could then be used to correct the average number of neutrons mentioned above, and the result was two energetic neutrons for each of the above targets. The emerging picture is one of two-nucleon absorption (2NA) which frequently leaves the residual nucleus in an excited state.

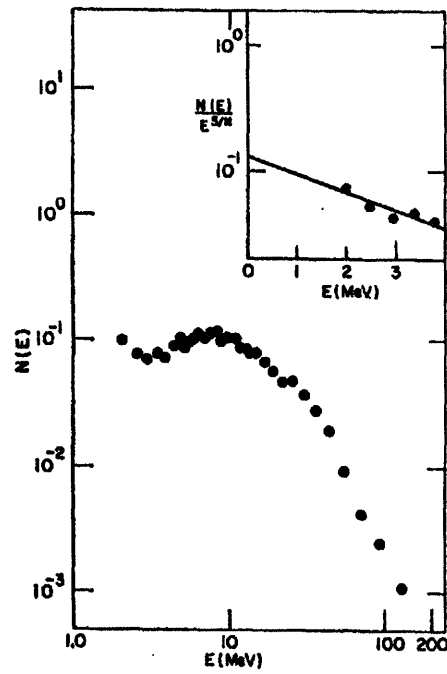


Figure 1-5: The energies of neutrons detected after the absorption of stopped π^- on ^{12}C from reference [5]. The insert shows the agreement between the low energy spectra and the predicted $E^{5/11}$ dependence from evaporation.

1.2. The Development of Two-Nucleon Absorption (2NA) as the Dominant Absorption Process 29

In 1965 Afanasev and Ostroumov [50] performed an emulsion experiment to examine the reaction $^{14}\text{N}(\pi^+, 2p3\alpha)$. They found that the energies of the three α 's was equivalent to that of a residual ^{12}C nucleus plus about 13 MeV of excitation energy. Thus, even in the complete breakup reactions two nucleons carry off the bulk of the energy.

More characteristics of 2NA were also examined. In 1960, Ozaki *et al.* [51] measured the ratio of the frequency of detecting nn pairs over the frequency of detecting pn pairs after the absorption of stopped π^- 's in C and Al. The authors found nn pairs more likely by a factor of 5 in C and 4 in Al, indicating the enhancement of absorption by T=0 pairs over T=1 pairs. Evidence for 2NA was also found for low energy π^+ 's absorbed in flight in C. The experiment, published by Balandin *et al.* [52] in 1964, used 40–70 MeV π^+ 's and found the average number of energetic protons emitted to be 2.2. In 1968 Nordberg *et al.* [53] measured the energy spectra of protons detected in coincidence with a neutron after the absorption of stopped π^- 's in C and found that the distribution peaked at one-half the total energy of the system, indicating that the rest of the nucleus acted as a spectator. This is in contrast to the singles spectrum measured by Fowler [54] in 1965 which peaked at extremely low energies and was presumably dominated by evaporation. Charpak *et al.* [55] reported an experiment in 1967 which measured the summed energies of two coincident protons after the absorption of π^+ on a variety of nuclei. With the exception of ^{14}N , they found clear peaks corresponding to two-nucleon absorption with the residual nucleus left in the ground state. Bressani *et al.* [56] determined that (π^+, pp) on ^4He and ^{16}O has the same angular dependence as $\pi^+ + d \Rightarrow p + p$ in 1969.

Lest the reader think the picture was becoming clear, it is important to point out that a few experiments were finding evidence for other absorption mechanisms. In 1968 Witten *et al.* [57] found indications of a small amount of single nucleon absorption of 68 MeV π^+ 's in C. They measured a singles spectra of proton energies and found a peak slightly under the total available energy in the system. Most of the experiments mentioned above that measured "protons" were actually only capable of determining the charge of the particle, and thus could not distinguish between protons, deuterons, and tritons. In 1964, Vaisenberg *et al.* [58] published an emulsion experiment in which they measured the multiplicities for charged particles having more than about 10 MeV. For absorption of stopped π^- on C, N, or O they found roughly equal numbers of deuterons and protons, and the number of tritons was about one-third the number of protons. This is an indication that possibly more nucleons are involved in the process, and some theorists of the time favored the possibility of absorption on an α -cluster [59, 60]. For 300 MeV π^- 's, the protons dominated the other two isotopes.

1.3 The Move to the Meson Factories

The 1970's were characterized by the three meson-physics facilities coming on line. The Los Alamos Meson Physics Facility (LAMPF) in Los Alamos is based on a 800 MeV linear proton accelerator. The Tri-University Meson Facility (TRIUMF) in Vancouver, Canada is based on a 520 MeV H^- cyclotron, and the Paul Scherrer Institute (PSI), known at the time as the Swiss Institute for Nuclear physics (SIN), is based on a 590 MeV H^+ cyclotron. All three pion factories were proposed in 1967, and came on-line in the mid 1970's. For the first time high intensity beams of mono-energetic pions were available to the experimental community. The results in pion absorption came slowly at first, but quickly accelerated into the 1980's. The first half of the decade was reviewed by Hüfner [28], but there are no good reviews of the second half available.

There were several experiments of importance in this period that came before the factories were fully operational. The first of these, performed by Favier *et al.* [6] and published in 1971, was designed as a more complete survey of two-nucleon absorption than had been previously attempted. The experiment consisted of two scintillator telescopes placed at $\pm 76^\circ$ which corresponded to 180° separation in the center of mass system. 76 MeV pions were used to measure the energy spectra for the reaction (π^+ ,2p) on fifteen targets ranging from 2H to Pb. The data were analyzed in terms of the missing mass, the magnitude and angle of the recoil momentum, and the Treiman-Yang angle. The missing mass is defined as the difference between the invariant mass of the residual A-2 system minus the minimum mass possible for such a system, *i.e.*:

$$[(E_\pi + M_A - E_{p_1} - E_{p_2})^2 - (\vec{p}_\pi - \vec{p}_{p_1} - \vec{p}_{p_2})^2]^{\frac{1}{2}} - M_{A-2}.$$

The Treiman-Yang angle [61] is defined in the system in which the incident pion is at rest. It is the angle between the plane defined by the momenta of the two outgoing nucleons and the plane defined by the momenta of the target and of the residual nucleus. If the absorbing pair has $S=0$ or if the pair is in an $L=0$ state with respect to the A-2 system then the differential cross section as a function of the Treiman-Yang angle should be constant, assuming that the two-nucleon absorption picture holds. The Treiman-Yang angle is thus a tool for checking the importance of the two-nucleon mechanism.

Figure 1-6 shows the Treiman-Yang distribution for absorption on 4He split into the cases in which the missing energy is ≤ 4 MeV, between 4 and 18 MeV, and ≥ 18 MeV. For the case

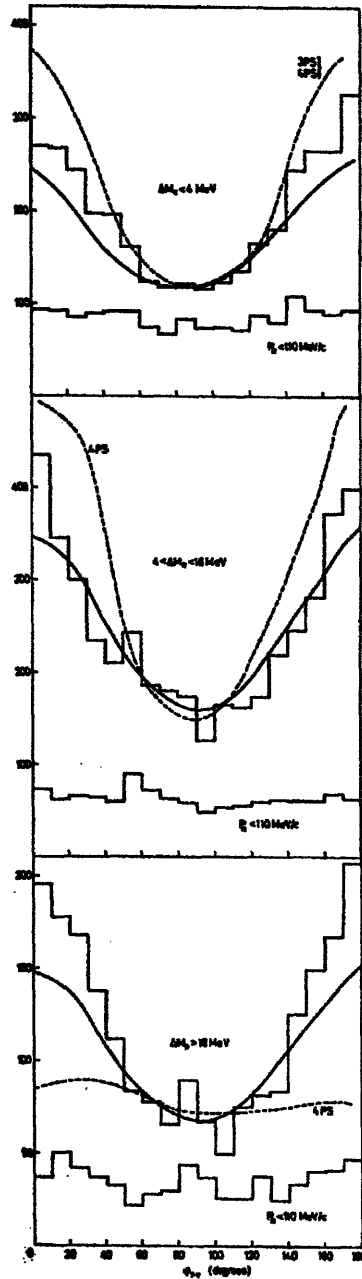


Figure 1-6: The Treiman-Yang angle for the absorption of 76 MeV π^+ on ${}^4\text{He}$ from reference [6]. The data were separated into three regions of the missing mass, as indicated in the figure. The distributions are also shown for the recoil momentum less than 110 MeV/c. The dashed lines result from phase space simulations.

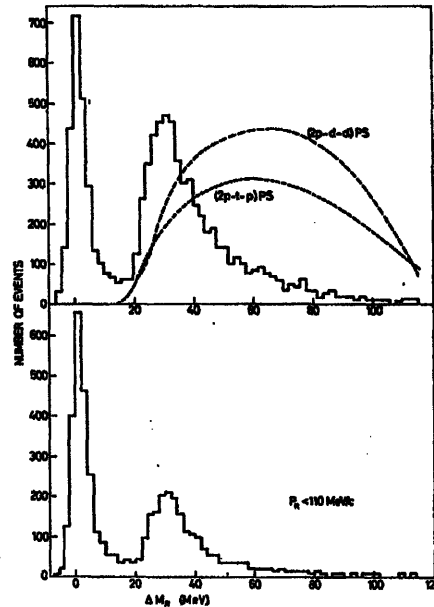


Figure 1-7: The missing mass distribution for the reaction ${}^6\text{Li}(\pi^+, pp)$ from reference [6]. The lower figure has the restriction that the recoil momentum is less than 110 MeV/c. The dashed curves are the result of phase space simulations.

where the recoil momentum is small (≤ 110 MeV) the geometry of the apparatus does not limit the acceptance, and the distribution does appear flat. When higher momenta are examined, the acceptance effects must be included. The authors compare the data to a phase space simulation (dashed line) and to a calculation by Lazard *et al.* [62] including the effects of rescattering on the residual system (solid line). The better agreement with the latter is taken as an indication that final state interactions play an important role, although the effects that initial state interactions would have were not mentioned when the authors were coming to this conclusion. The Treiman-Yang angle has an essentially flat distribution for the low recoil momentum region for all the nuclei measured between ${}^4\text{He}$ and ${}^{16}\text{O}$. The higher momenta are difficult to interpret because of the lack of calculations on these targets.

On more massive nuclei the interesting results from this paper involved the missing mass spectra. Figure 1-7 shows the distribution of missing mass after absorption on ${}^6\text{Li}$, and figure 1-8 shows the same distributions for ${}^9\text{Be}$ to ${}^{16}\text{O}$. In all cases specific peaks corresponding to the removal of nucleons from different shells are apparent. The distribution on ${}^6\text{Li}$ is especially

interesting since this nucleus is frequently modelled as a deuteron in orbit around a ${}^4\text{He}$ nucleus. In the figure the missing mass has two clear peaks corresponding to absorption on the ${}^4\text{He}$ and on the ${}^2\text{H}$ components of the nuclear wavefunction. The presence of large strength at higher missing energies is interpreted as a possible sign of more complex interactions. The difference between the outlooks in 1971 and in the present is made clear when the authors realize the difficulty of examining this region and classify it as “an annoying background, obscuring the interesting quasi-free events.”

In 1973 Bellotti *et al.* [7] used a propane bubble chamber to study the absorption of 130 MeV π^+ on C. They measured a total cross section of 189 ± 19 mb, which was the first precise measurement of a total absorption cross section on a nucleus heavier than ${}^2\text{H}$. The value obtained was about 50% of the total π^+ -C inelastic cross section, and was large compared to the estimated cross sections from two-nucleon correlation studies. Figure 1-9 shows the charged prong (>10 MeV) multiplicity distribution. The estimated single charge exchange contamination has been subtracted. The authors analyzed the different prong numbers separately, examining proton energies, missing energies, missing momenta, and opening angles. The conclusions they draw were rather surprising.

They estimate the cross section for quasi-free two-nucleon absorption to be about 10% of the total cross section. Another 15% they attribute to two-nucleon absorption with an undefined energy transfer to the residual nucleus. Less than 35% of the total number of events have two charged particles each above 50 MeV. They see a significant fraction of events with three energetic charged prongs which they attribute to absorption on an α -cluster (40%), although they apparently never consider the possibility of absorption on three nucleons. They also see four-plus prong events 15% of the time which they associate with absorption on either a ${}^2\text{H}$ or α cluster, followed by final state interactions.

Another technique to study pion absorption was pioneered during this period. The method is to examine γ -ray energies after stopped π^- are absorbed on heavy nuclei. In the cases that the residual nucleus is left in its final state, it will de-excite by particle emission until it has <10 MeV excitation energy, at which point it will de-excite by γ emission. By measuring the energy spectra, it is possible to identify the residual nuclei after any absorption and evaporation has occurred. This technique is more useful for stopped pions, as absorption and quasi-free knockout are not distinguishable if the pion was in-flight.

Figure 1-10 shows a γ energy spectrum after π^- absorption on ${}^{31}\text{P}$. The data are from an experiment by Ullrich *et al.* [8] in 1974. The upper curve is for stopped pions, and the lower for

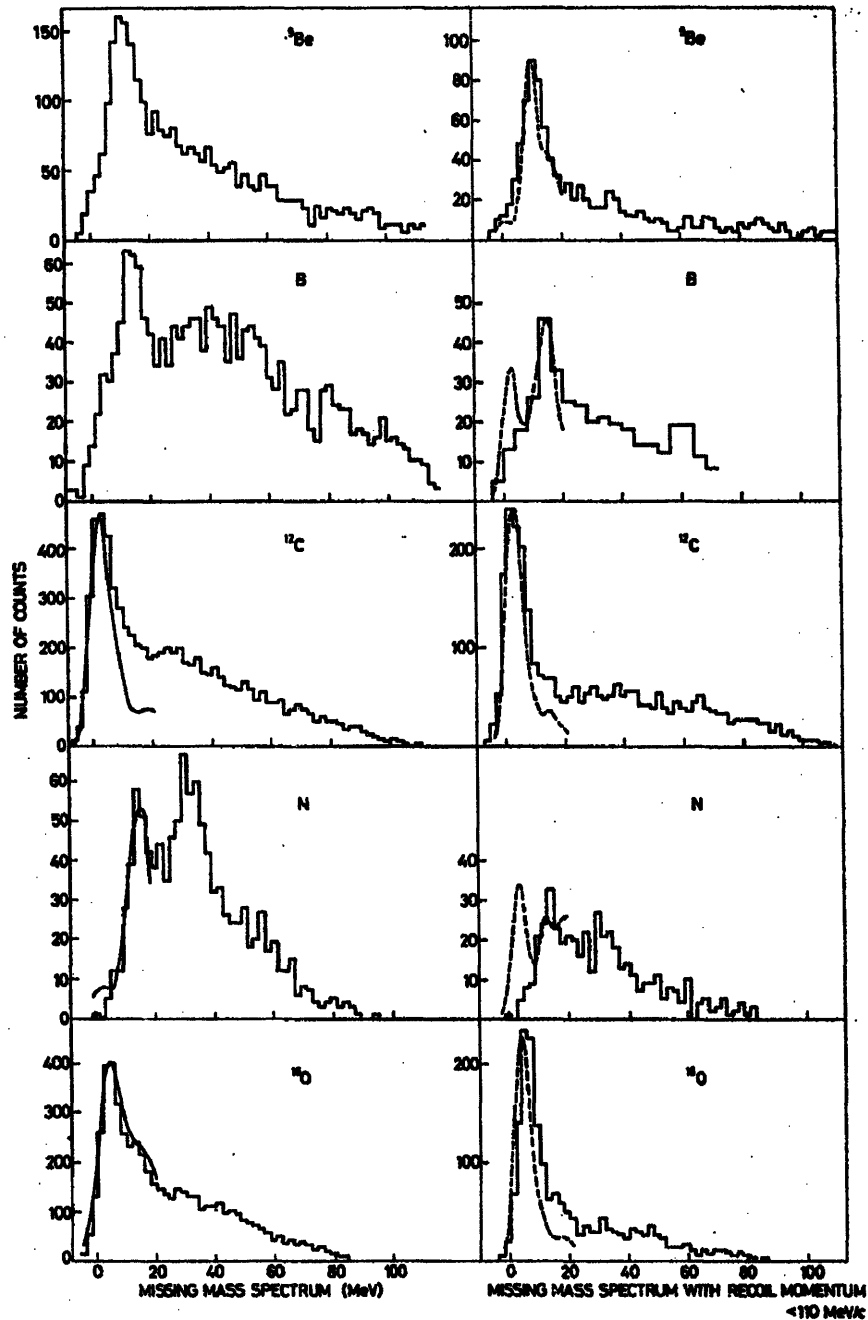


Figure 1-8: Missing mass distributions for the absorption of 76 MeV π^+ on five targets from reference [6]. The right side has the restriction that the recoil momentum is less than 110 MeV/c.

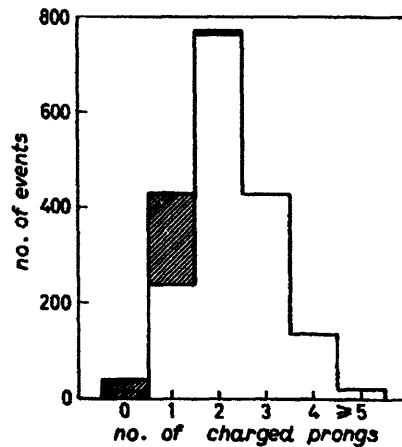


Figure 1-9: The charged prong multiplicity after the absorption of 130 MeV π^+ on ^{12}C from reference [7].

$T_{\pi^-} = 60$ MeV. This type of experiment gives a very limited view of the absorption process, since γ 's are only seen if the residual nucleus is excited. Only about 16% of the stopped π^- events led to γ emission. One expects that the cases in which evaporation occurred would be preferentially selected here, since nucleon emission is usually followed by γ emission, so the information available about the reaction dynamics is somewhat obscured.

In 1977, Jackson *et al.* [9] measured the energy spectra for high energy protons ($60 \text{ MeV} < T_p < 200 \text{ MeV}$) at 45° and 94° following the absorption of 100 and 220 MeV π^+ and π^- on Al, Ni, and Ta. The spectra for Ni are shown in figure 1-11. The distributions are relatively featureless, protons are about three times more likely from π^+ absorption than from π^- absorption, and the energy spectra from absorption of the two pion types are similar except for 100 MeV at 45° . Energetic deuterons ($\geq 80 \text{ MeV}$) were seen only 3% as often as energetic protons. The authors note that the three-to-one ratio for protons would be trivially explained if the absorption tended to occur on an α -cluster.

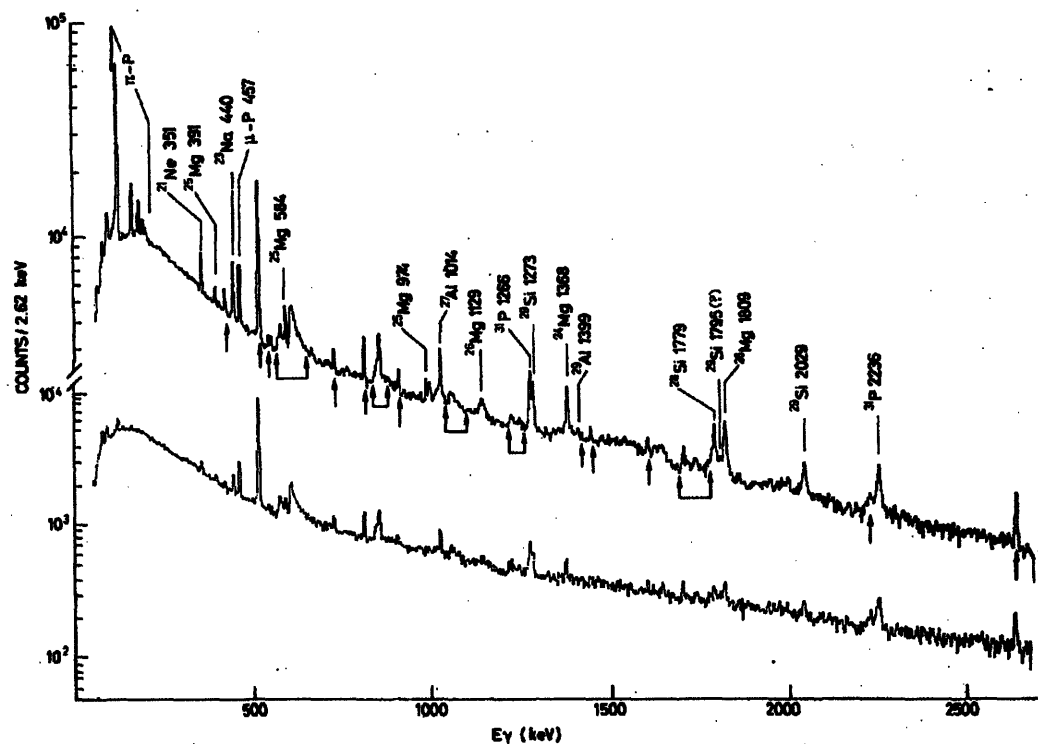


Figure 1-10: The spectra of detected γ -rays following the absorption of π^- on ^{31}P from reference [8]. The upper curve is for 0 MeV pions, and the lower is for 60 MeV pions. The nuclei corresponding to the individual peaks is identified.

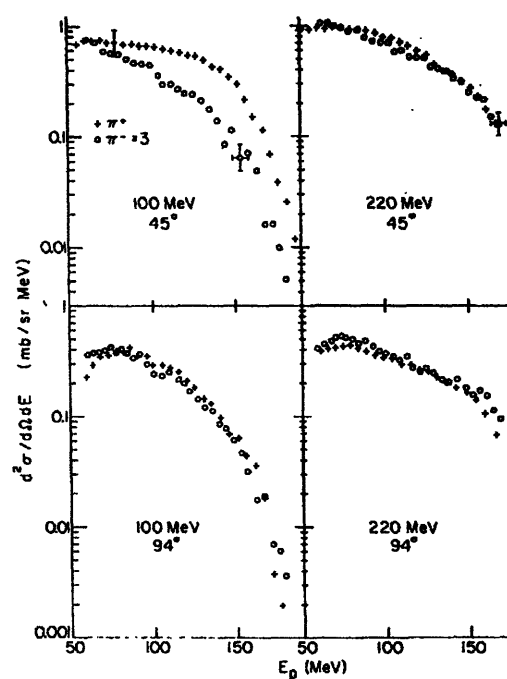


Figure 1-11: The energies of protons from the absorption of 100 and 220 MeV π^\pm on ^{62}Ni from reference [9]. The top spectra were measured at 45° and the bottom at 94° . The π^- results have been multiplied by a factor of three.

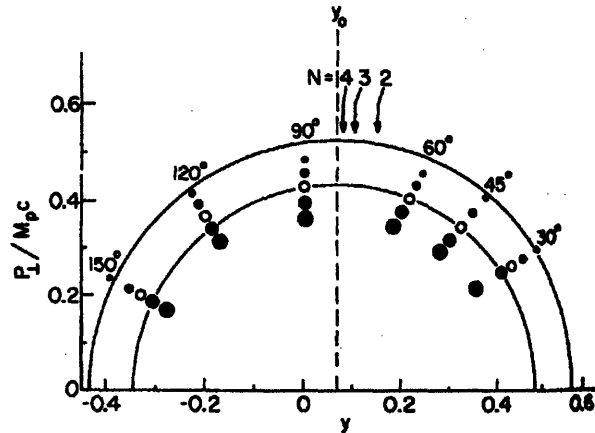


Figure 1-12: A rapidity plot for the absorption of 220 MeV π^- on ^{181}Ta from reference [10].

1.4 Recent Developments: The Eighties and Nineties

By 1980, the picture of absorption on nuclei that had emerged included a strong component of absorption on two-nucleon pairs in the nucleus with the rest of the nucleus acting as a spectator. Although there were still some indications of possible multi-nucleon absorption mechanisms, in general it appeared that this was mainly due to evaporation. It was becoming more believable that two nucleon absorption, with some initial state and final state interactions modifying the process, was the dominant effect. This picture would change in the eighties. There were several good reviews in this period including Ingram [63], Redwine [64], Ashery and Schiffer [65], and Weyer [66]. In addition, a book on pion-nucleus interactions was written in 1988 by Ericson and Weise [67].

In 1980, McKeown *et al.* [10] published the results of their experiment studying the absorption of pions on a variety of nuclei ranging from carbon to tantalum. They examined singles spectra for final state protons with high enough energies that it was likely that the protons came from absorption. In the analysis they borrowed a technique from high energy and heavy ion physics to determine the total mass of the absorbing system, and thus the number of nucleons involved. This technique makes use of a quantity known as the rapidity.

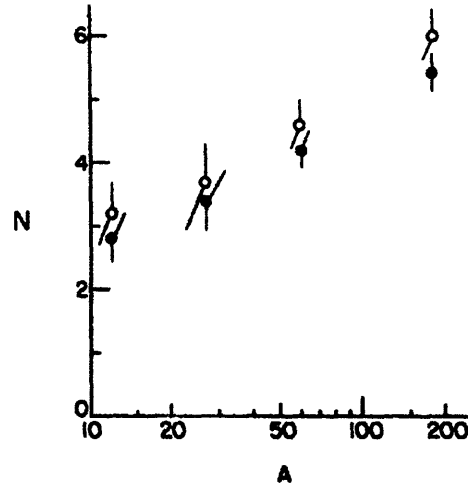


Figure 1-13: The A-dependence of the average number of nucleons participating in the absorption of π^+ (solid circles) and for π^- (open circles) from reference [10]. The results are averaged over the incident pion energies of 100, 160, and 220 MeV.

Rapidity is defined as the inverse hyperbolic tangent of the component of the proton's velocity parallel to that of the incident pion (in units where $c = 1$), or:

$$y = \tanh^{-1}\left(\frac{p_{\parallel}c}{E}\right)$$

When the rapidity is plotted versus the perpendicular component of the proton's momentum, one expects that the contours of constant cross section will be symmetrical around a value corresponding to the number of nucleons in the absorbing system. For an example of a rapidity plot see figure 1-12 where McKeown's results are shown for absorption of 220 MeV π^- on ^{181}Ta . Circles are fit to different constant values of the differential cross section. The value of y_0 that these circles are symmetric around is shown, as well as the values that would correspond to 2, 3, or 4 nucleons in the absorbing system.

The conclusion drawn from this analysis is that an average of almost 6 nucleons participate in this absorption process. Figure 1-13 shows the average number of nucleons involved, averaged over the results with 100, 160, and 220 MeV incident pions, as a function of A. A mechanism based on two-nucleon absorption with small modifications would have difficulty explaining the large number of nucleons involved on average as determined by this experiment. The question of the underlying mechanism was thus reinfused with vigor.

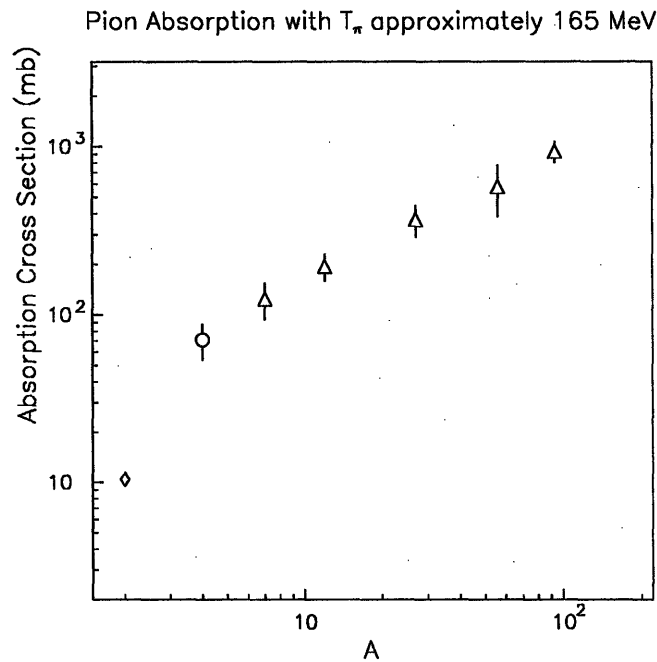


Figure 1-14: The A -dependence of the absorption cross section for π^+ around 165 MeV. The diamond is from Neganov and Parfenov [11], the circle is from Baumgartner *et al.* [12], and the triangles are from Ashery *et al.* [1].

In 1981 Ashery *et al.* [1] published the results from an experiment measuring the total cross sections for π^+ absorption on a variety of nuclei from ${}^7\text{Li}$ to ${}^{209}\text{Bi}$ at six energies in the region of the Δ -resonance. This experiment used a transmission/subtraction technique. Essentially, two different experiments were performed. In the first, a pion beam of known intensity was incident on the target and the intensity of the pion beam after the target was measured, determining a total reaction cross section. In the second experiment, the differential cross section was measured for the detection of a charged pion in the final state. This differential cross section was then integrated to obtain a total scattering cross section. The difference between these two values gives the sum of the absorption cross section and the single charge exchange cross section. The authors then subtracted an estimate of the SCX cross section to obtain a total absorption cross section.

The results at 165 MeV appear in figure 1-14. The absorption cross section appears to increase as $A^{0.7}$ for $A > 6$. This agrees with simple intuition: The pion interacts with nuclei via the strong interaction, and thus the interaction tends to occur on the surface. Thus, one

would expect the total absorption cross section to increase with the nucleus's cross sectional area which is proportional to $A^{2/3}$. In the absence of a different A-dependence in the competing channels, this should give the A-dependence for absorption.

The agreement with the power law in A is strong. However, when one includes the total cross section as measured on deuterium [11], it is clear that between deuterium and ${}^7\text{Li}$ this power law is not followed. This fact is an indication that the absorption process is changing in this region—a possible indication that new reaction mechanisms are becoming available as more nucleons are added to the system. The obvious place to study these reactions is in the lightest nuclei where one can isolate the effects of adding one or more nucleons to the system. Much of the following work has thus concentrated on studying absorption in ${}^3\text{He}$ and ${}^4\text{He}$.

Also in 1981 a different collaboration with Ashery as first author [68] published the results of a comparison between π^+ and π^- absorption on ${}^3\text{He}$ and ${}^4\text{He}$ with 165 MeV pions. The authors found that the ratio:

$$R = \frac{d\sigma(\pi^+, pp)}{d\sigma(\pi^-, pn)}$$

varied with angle between 100 and 200 on ${}^3\text{He}$ and was about 200 on ${}^4\text{He}$. The results were interpreted in terms of the ratio of absorption cross sections on T=1 and T=0 nucleon pairs. The authors found that the latter reaction is favored over the former by a factor of about 40. This result was later found to be incorrect by Backenstoss *et al.* [15, 69] as will be described below.

The only stopped pion experiment which we will mention in this section is that performed by Gotta *et al.* [13] published in 1982. This experiment was a kinematically complete measurement of the final state after π^- absorption on ${}^3\text{He}$. The results were presented in the form of a Dalitz plot, as shown in figure 1-15. In a Dalitz plot the energy of one nucleon is plotted against the energy of the other. The kinematically allowed region forms an ellipse on the plane. Events in which the three nucleons share the energy equally, perhaps corresponding to a three-nucleon absorption mechanism, would lie near the center of the ellipse. Events in which the particles are essentially back-to-back (although two can travel in the opposite direction to the third with equal energies) would lie near the edge. The authors found that the events populated the edge of the ellipse. They also found that soft-FSI, in which two nucleons have almost the same momenta, was a significant process.

In 1983, Baumgartner *et al.* [12] measured the total cross section on ${}^4\text{He}$ in the region of the Δ -resonance. The result at 170 MeV was 70.9 ± 17 mb. This value lies on the $A^{0.7}$

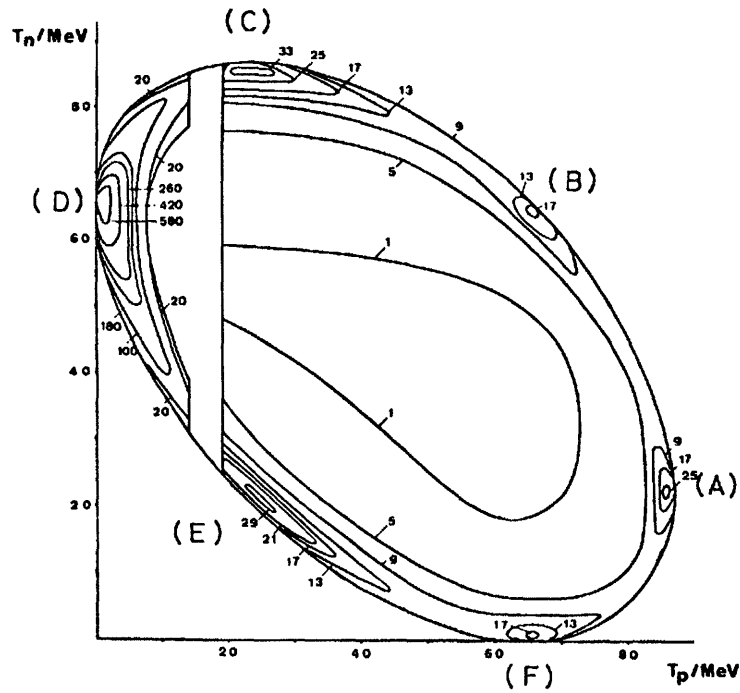


Figure 1-15: A Dalitz plot for the absorption of stopped π^- on ${}^3\text{He}$ from reference [13]. Region (A) corresponds to nn -FSI, (B) and (F) to $\pi^-pp \Rightarrow pn$ QFA, (C) and (E) to pn -FSI, and (D) to $\pi^-pn \Rightarrow nn$ QFA.

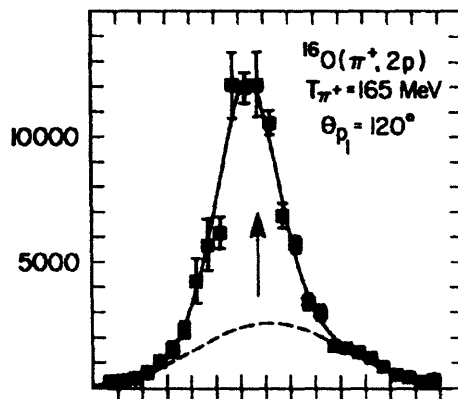


Figure 1-16: The angular distribution of an outgoing proton from the reaction $^{16}\text{O}(\pi^+, pp)$ at 165 MeV with the other proton detected at 120° [14]. The differential cross section is fit by the sum of two gaussians.

curve determined by experiments on heavier targets, as seen in figure 1-14. Thus, something interesting appears to happen between deuterium and ^4He . In the same year Navon *et al.* published the results of an experiment in which they compared the total absorption cross section measured on ^{16}O to that on ^{18}O . Their results showed that absorption on ^{18}O was 20% stronger than that on ^{16}O . This increase was interpreted as being associated with a large additional cross section for absorption on the additional nucleon pair. Since this pair has an isospin of one, this might be an indication that absorption on $T=1$ pairs is favored over absorption on $T=0$ pairs—a different situation than found previously for stopped pions [51].

However, during the next few years a group consisting of mainly the same members published more results in two papers by Altman *et al.* [14, 70]. In these papers the authors introduced a new analysis technique that has proven somewhat controversial. A coincidence experiment was performed where two protons from an absorption reaction were detected with the angle of one of them held fixed. The angular differential cross section for the other was then determined. This cross section was fit to the sum of two gaussians, one narrow and the other wide (see figure 1-16). The narrow gaussian was associated with two nucleon absorption and the wide gaussian with a multi-nucleon absorption process. By making this identification, the authors were able to measure the amount of the total cross section that was attributable to absorption on two nucleons.

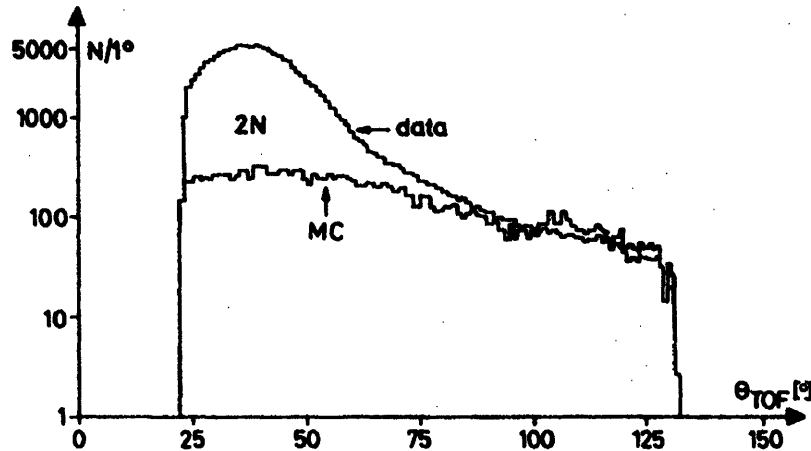


Figure 1-17: The angular distribution of a proton when another was detected at 117° after the absorption of $120 \text{ MeV } \pi^+$ on ^3He [15]. The distribution labeled MC is the results of a three-body phase space simulation.

Using this method, the authors measured an undisturbed two-nucleon cross section of roughly 10% of the total absorption cross section on $^{16,18}\text{O}$. Their estimates of the correction factor required to account for the effects of FSI increased this fraction to 20%. The remaining 80% of the cross section would need another explanation. In addition, Altman *et al.* found only small changes in the absorption cross section between ^{16}O and ^{18}O . Since ^{18}O consists essentially of two neutrons outside of a ^{16}O core, the obvious interpretation was that cross shell absorption is suppressed.

Backenstoss *et al.* [15, 69] published papers in 1984 and 1985 showing the results of a Δ -resonance region absorption experiment on ^3He . Their more precise measurements of the ratio:

$$R = \frac{d\sigma(\pi^+, pp)}{d\sigma(\pi^-, pn)}$$

obtained a value of $25. \pm 7.0$ at their angular setting at 165 MeV and values varying between 17.0 ± 5.0 and 22.2 ± 7.5 at 120 MeV. These results give a factor of about seven enhancement for the absorption on $T=0$ pairs over absorption on $T=1$ pairs. This result is significantly smaller than the ratio of 40 found by Ashery *et al.* [68]. The newer result is generally accepted.

The Backenstoss experiment also identified a component of the absorption cross section in which the final state protons have momenta distributed similarly to three-body phase space.

Figure 1-17 shows the in-plane angular distribution of one detected proton when another was detected at 117° after the absorption of 120 MeV π^+ on ^3He . A clear peak is seen at the quasi-free absorption angle, as well as a more uniform distribution that is well described by a three-proton phase space simulation. This result implies that all three absorbing nucleons can play an equal role in the process. It was the strongest evidence to date of the existence of a coherent three-body process, and it clearly demonstrated a difference between resonant and stopped pion absorption.

Tacik *et al.* performed an experiment where they detected three protons in coincidence after the absorption of 130, 180, and 228 MeV π^+ 's on ^{12}C . They published a paper on the 228 MeV data [71] in 1985, and a further paper [72] in 1989 with the other two energies and an updated analysis at 228 MeV. In their analysis they fit the individual proton energies, summed energies, and angular distributions to Monte Carlo simulations of several possible final states. In their initial paper they found that $pppn\alpha\alpha$ phase space fit their results the best, and concluded that this was evidence for an absorption process in which the pion scatters several times before being absorbed. The re-analysis in their second paper found that three body phase space is the best fit (with the momentum of the residual spectator nucleus consistent with a Fermi-distribution). The authors looked specifically for signs of initial state interactions by looking for the backward going proton from the two-body absorption when two forward-going protons were detected. Although their data were somewhat unclear, the author's interpretation was that ISI is not a significant contributor to three-body absorption.

Aniol *et al.* [73] reported the results of their measurement of two-nucleon absorption at two energies below the Δ -resonance in 1986. The energies used were 63 and 90 MeV. The authors measured a component due to two-nucleon absorption that had a similar differential distribution to absorption on deuterium and had a magnitude equal to 1.5 times the deuterium absorption cross section. This result is interesting because there are 1.5 $T=0$ nucleon pairs in ^3He . If correct, the implication is that the difference in environments does not affect the cross section, or that the various effects tend to cancel each other. Since there are several factors that are different, including the relative momenta and inter-nucleon spacing, it seems unlikely that the only characteristic of importance is the total isospin.

Burger *et al.* performed an experiment for which they published the first results in 1986 [74] and the complete analysis in 1990 [75]. The authors measured absorption on ^{58}Ni at 160 MeV. They used a similar two-gaussian analysis to that of Altman *et al.* [14] to separate the two from the multi-nucleon absorption processes. After correcting for the contribution of FSI by using a DWIA calculation, the authors found that 2NA accounts for about 30% of the total

cross section. These authors also looked for signs of ISI by looking for expected asymmetries in the angular distributions, and concluded that if ISI were present, it would account for less than 10% of the total cross section.

It was at this time that the proposal for the LADS detector was submitted [76]. It is thus a good point to summarize the state of the knowledge before continuing with further descriptions of experiments. Pion absorption had been established as an important nuclear process accounting for roughly one-third of the total pion-nucleus cross section in the region of the Δ -resonance. The Δ -resonance clearly plays an important role in the process, as shown by the strong peaking of the absorption cross section in this energy region. The simplest absorption process—absorption on a deuteron—had been extensively studied. Both its energy dependence and angular distributions had been precisely measured and parameterized.

In other nuclei, a two-nucleon absorption process in which the pion is absorbed on a two-nucleon pair with the rest of the nucleus acting as a spectator had been clearly identified. Experiments had indicated that absorption on a $T=0$ pair dominated absorption on a $T=1$ pair by a large factor. Thus, the two-nucleon component was referred to as deuteron-like or quasi-deuteron absorption. The measured magnitude of the 2NA in which the rest of the nucleus acts as a spectator is significantly smaller than 100%. One expects, however, that sometimes the absorption would be preceded by a pion-nucleon scattering (ISI), and sometimes it would be followed by a nucleon-nucleon scattering (FSI). Attempts were made to measure the importance of these processes. Although the data were not precise enough to determine the magnitude of these two processes directly, some experiments had seen signs of each, but limited their magnitudes. In the heavier nuclei like ^{12}C and ^{58}Ni , it appears that less than 50% of the cross section can be accounted for by a combination of 2NA, 2NA+ISI and 2NA+FSI. Thus the question remains of what accounts for the other 50%.

Indications had been found from several experiments that a significant fraction of this remaining multi-nucleon absorption had final states well described by three body-phase space. If so, this could indicate either a new nuclear absorption process in which three nucleons play an equal role, or a mixture of several different processes such that the individual features of each are no longer distinct. The story does not end with three-body absorption, however, as the initial experiment which reopened this question indicated that processes in which more than three nucleons are involved are also significant.

The major open questions at this point included: Is there a multi-nucleon absorption process? If so, what are its characteristics, and how important is it? What are the magnitudes

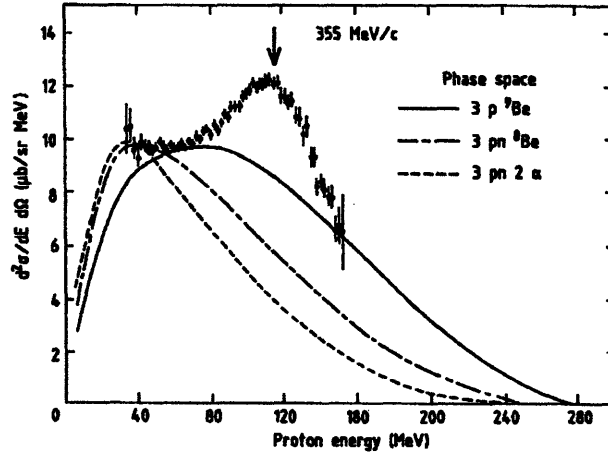


Figure 1-18: The energies of protons at 8° after the absorption of 242 MeV π^+ on ^{12}C from reference [16]. The arrow shows the energy that a proton would have after a free scattering process.

and features of 2NA, 2NA+ISI, and 2NA+FSI in nuclei? Does 2NA have a magnitude simply equal to the number of $T=0$ pairs times the deuterium absorption cross section? LADS was designed to address these questions as described in the next chapter. Now we will continue with the development of results from other experimental groups which have published while LADS was underway.

In 1987 Brückner *et al.* [16] published their results from a triple coincidence reaction measuring $^{12}\text{C}(\pi^+, 3p)$ with 240, 260, and 290 MeV pions. The authors were looking for signs of a ΔN bound state which would suppress the decay of the Δ thus leading to longer lifetimes. They found no signs of such a state, but they did see a broad peak at small forward angles (see figure 1-18) where the protons had energies consistent with quasi-free knockout reactions. This is a clear indication of the existence of ISI. However, the integrated size of the peak was small and would account for only a small fraction of the total cross section.

The technique pioneered by Altman *et al.* [14] of using a two gaussian decomposition of angular spectra to quantify 2NA was quite controversial. Many physicists believed that there might be another explanation for the narrow gaussian. In 1988 Schumacher *et al.* [17] published an experiment on $^{16,18}\text{O}$ that attempted to address this question by using a much better energy resolution than previous experiments had. This improved resolution allowed the identification

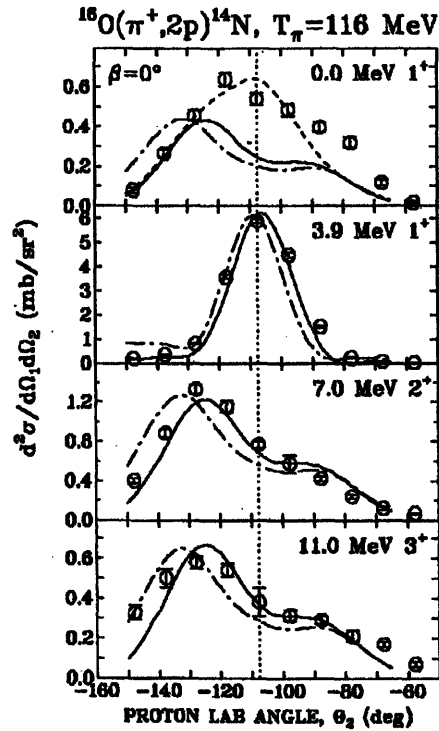


Figure 1-19: In plane angular distributions for a proton with the other detected at $+50^\circ$ after the reaction $^{16}\text{O}(\pi^+, 2p)^{14}\text{N}$ with 116 MeV pions from reference [17]. The various measurements are to specific nuclear final states with the specified excitation energies and angular momenta. The dotted line at -108° shows the quasi-free angle.

of individual final states of the residual nucleus, and thus the angular momenta of the absorbing pairs could be determined. The authors found that $L=0$ absorption leads to a narrow gaussian distribution and $L=2$ absorption leads to a wider gaussian distribution of the variables measured by Altman *et al.* [14] and by Burger *et al.* [74]. The data were also interpreted as showing that cross shell absorption was not suppressed, and that 2NA could explain less than about 50% of the cross section.

The results from this experiment seemed to justify the theoretical prediction of Ritchie [77] who had claimed that these two possible angular momenta would lead to narrow and wide gaussians. However, further comparison of the Schumacher data with those of Altman and Burger showed that the narrow gaussian in the latter two cases included both the narrow and wide gaussian found by Schumacher. The other two experiments did not resolve effects of the

size Schumacher was measuring. Thus, the extent to which the two gaussian technique can be used to quantify two and multi-nucleon absorption is still somewhat open to question.

Now a series of experiments on helium in the Δ -resonance region began to be published. The first of these was Steinacher *et al.* [78], who measured absorption on ^4He at 120 MeV. The authors identified separate three and four body phase-space-like components following absorption. They found a total cross section of 52.7 ± 9.0 mb which suggests that the earlier results of Baumgartner may have been too high. Undisturbed 2NA accounted for 70% of the total. A surprising result was that absorption on a ppn triplet was apparently twice as likely as absorption on a ppn triplet. This was unexpected because the cross section for π^+ -p to form a Δ is three times as large as the cross section for π^+ -n to form a Δ . Assuming that the reaction commences with a Δ being formed, one would have expected ppn absorption to be more likely than ppn absorption. In addition, the experiment found that about 10% of the time a deuteron is involved in the absorption reaction in some capacity other than as a spectator.

In 1991 Weber *et al.* [79] published an experiment measuring the absorption of 165 MeV pions on ^4He . They detected triple coincidences in the reaction plane and measured the cross section for absorption on a ppn triplet to be 4.5 ± 1.0 mb, almost twice the value Steinacher measured at 120 MeV. Weber *et al.* also put an upper limit of 2 mb on 4NA and saw no significant deviations from three-body phase space in the three nucleon absorption spectra.

Also in 1991, Mukhopadhyay *et al.* [80] published the results of an experiment on ^3He at 165 MeV. They measured a 2NA cross section of about 17 mb, and a 3NA cross section of about 10 mb. Interestingly, this is the first experiment to see significant signs of deviations from three body phase space in their 3NA results. As their experiment also only measured protons in the reaction plane, and all previous experiments had extrapolated out of plane by using three body phase space, these in-plane deviations cast doubt on previous multi-nucleon absorption total cross sections.

An experiment measuring pion absorption on ^{16}O at 115 and 165 MeV was also published in 1991 in two separate papers, one by Hyman *et al.* [81] and the other by Mack *et al.* [82]. The authors used energy excitation cuts to select 2NA, subtracted off an estimated phase space background, and corrected by a DWIA calculation for the effects of FSI. They found that 70% of the total cross section is attributable to 2NA at 115 MeV, and 50% at 165 MeV. This is a much larger fraction for 2NA than had been previously measured, and leaves open the possibility that the remaining cross section has an underlying mechanism that is based on two nucleons. An interesting facet of this paper was that the authors attempted to test the DWIA calculation

by comparing singles and coincident spectra at 2NA kinematics. They did find agreement with their model, but it bordered between quantitative and only qualitative.

Now we begin to see results from large solid angle detectors. The first of these was a plastic array covering roughly 50% of 4π steradians. The experiment, published in 1992 by Adimi *et al.* [83], measured pion absorption on ^4He at 114 MeV. This experiment measured a 2NA cross section of 50% of the total cross section. Absorption on a *pnn* triplet was found to be equally likely as absorption on a *ppn* triplet. The authors also found that soft-FSI was significant, affecting about 20% of the cross section, and that ISI+2NA was insignificant. These results are different enough from the Steinacher experiment at approximately the same energy to leave significant doubt in our quantitative knowledge.

Finally we must report the prolific results of the BGO ball collaboration. The BGO ball is the detector most similar to LADS in that it covers almost 4π solid angle with a low energy threshold and the capability of detecting neutrons. It does not have the angular precision or the granularity of the LADS detector. The recent results have been published in 1992 and 1993 by Ransome *et al.* [84, 85] and Jones *et al.* [86]. The energies range from 50 to 500 MeV and the targets from ^6Li to ^{238}U . The results are published as missing energy spectra and as separations into cross sections for experimentally detected final states with no corrections for geometry or energy thresholds. In addition, they do not make any serious comparisons with simulations, making their results difficult to interpret.

Chapter 2

The LADS Detector

2.1 Design Motivation and Goals

In the last chapter some of the experimental questions that LADS was designed to address were raised. As a reminder: Is there a multi-nucleon absorption process? If so, what are its characteristics, and how important is it? What are the magnitudes and features of 2NA, 2NA+ISI, and 2NA+FSI in nuclei? Does 2NA have a magnitude simply equal to the number of T=0 pairs times the deuterium absorption cross section? In order to address these questions, a detector needs several characteristics.

The most important requirement is that the detector cover a large fraction of phase space; *i.e.*, a close to 4π solid angle geometrical coverage with a low energy threshold. As the mechanism behind a possible multi-nucleon absorption mechanism is not understood, it is not possible to make large extrapolations over unmeasured regions of phase space accurately. This was the most important lack of prior experiments. There were several with sufficiently low thresholds, but with the exception of some early, low statistics bubble chamber experiments, all of the prior experiments had only small geometrical acceptances. Typically, extrapolation factors used to obtain multi-nucleon absorption cross sections were on the order of ≥ 1000 . The most glaring aspect of this was that there were no recent measurements out of the reaction plane.

As absorption reactions frequently lead to multi-particle final states, the detector components must be segmented enough to detect and classify several particles simultaneously. Many possible particle types arise from absorption reactions, or from other contaminating reactions,

necessitating clean particle identification (PID) techniques. For charged particles this means the separation of pions, protons, deuterons, and possibly tritons, ^3He 's and α 's. For neutral particles the detection and separation of photons and neutrons is required. Although the energy resolution available for the charged particles would be difficult and expensive to obtain for the neutral particles, some is required. For example, it is necessary to identify whether neutrons arise from evaporation or directly from the absorption reaction. For neutrons, energy resolution is determined by the resolution with which the time-of-flight is measured.

As improved energy resolution is always desirable, the question of how much is necessary is difficult to address satisfactorily. The required angular resolution is easier to obtain than the required energy resolution, so the energy resolution was the limiting factor. Some possible levels, from worst to best, would be:

- 1) The identification of an absorption reaction by the total kinetic energy of the resulting charged particles.
- 2) The separation of absorption on deuterium from that on other nuclei present in the detector (useful for detector studies) or the general separation of S from P shell absorbing nucleons from the binding energy differences.
- 3) The determination of whether all the nucleons involved in the absorption process were detected by measurements of the missing momenta spectra and comparisons with Fermi momenta spectra.
- 4) The identification of individual final states of the residual nuclei.

The last of the above possibilities would require a magnetic field based detector, which would be too expensive with 4π coverage, so it had to be discarded. The second to last would require resolution on the order of 10% of typical Fermi momenta, or roughly 20 MeV/c. With perfect angular resolution, the energy resolution required to obtain 20 MeV/c momentum resolution (two 150 MeV protons detected after absorption of a 165 MeV pion on ^3He) is 5% (per proton, 3.5% summed energy). This is obtainable by scintillation detectors, and as the separation of different absorption mechanisms was one of the primary motivations for LADS, it was chosen as the design goal.

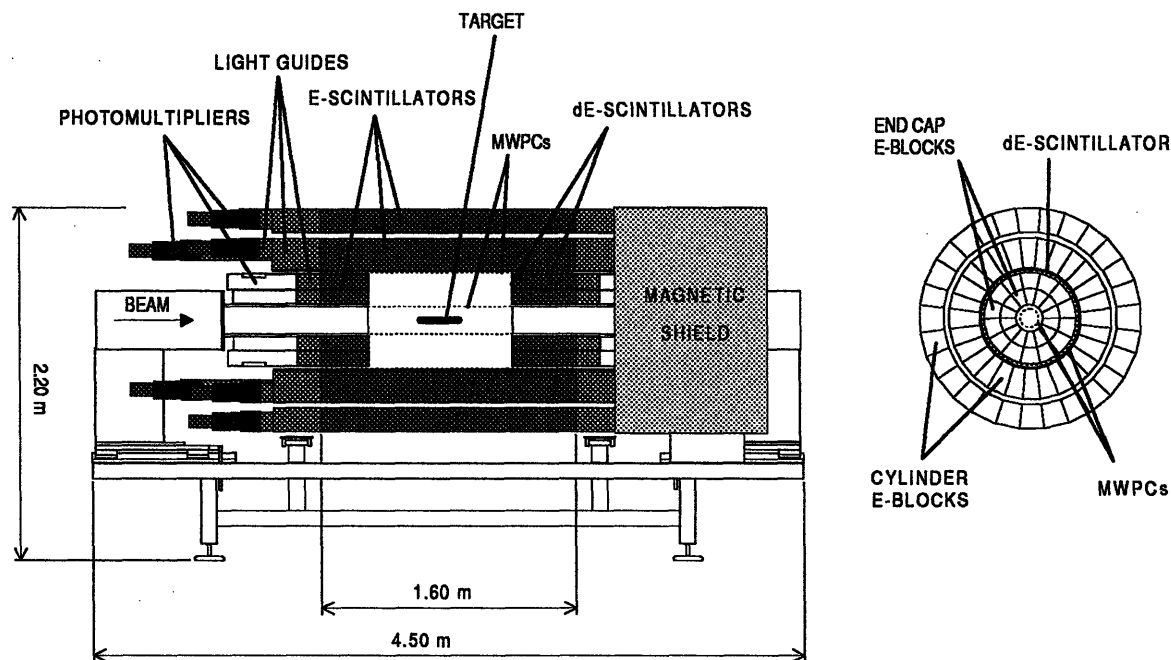


Figure 2-1: The LADS detector, adapted from reference [18].

2.2 Overview

LADS was constructed at the Paul Scherrer Institute in Villigen, Switzerland by a collaboration of forty-three physicists from twelve institutions in six countries. The detector (see figure 2-1 and table 2.1) consists of a combination of plastic scintillators and multi-wire proportional chambers. The scintillator is distributed through three concentric cylindrical barrels (dE-E-E), each 1.6 m long and divided into 28 sectors. The scintillators are read out by phototubes on both ends which match the area of the scintillators as closely as possible. This achieved the desired energy resolution for charged particles of under 5%. In addition, the ends of the cylinder are plugged with scintillating “endcaps”, also with dE and E-block components. Only 8 cm diameter entrance and exit windows remain uncovered in order to allow the beam to pass through the detector, and a geometrical acceptance of over 98% of 4π steradians is obtained.

The inner radius of the scintillating cylinder is 30 cm. The interior space contains the target mechanism and two cylindrical multi-wire proportional chambers (MWPC's). LADS uses a high pressure gas target capable of containing pressures of up to 100 bar. It is 25.7 cm

LADS's Performance	
Geometrical acceptance	98.5% of 4π sr
Energy threshold for protons	≈ 20 MeV
Maximum measurable proton energy	> 200 MeV
Energy resolution for charged particles	3-5% (FWHM)
Vertex resolution from two tracks	1 mm (FWHM)
Angular resolution	$< 1^\circ$
Detection efficiency for neutrons	$\approx 35\%$
Angular resolution for neutrons	$\approx 10^\circ$

Table 2.1: LADS's characteristics.

long, has a 2 cm radius, and is constructed of carbon fiber. This design maximizes the ratio of absorption in the target gas to absorption in the target container, giving a high ratio of signal to noise. The MWPC's provide trajectory information for charged particles to a resolution of better than 1° . For those events which have two charged particles each passing through both chambers, the resolution in the reconstructed event vertex is on the order of 1 mm. This accuracy is used to separate events occurring in the target gas from those originating elsewhere.

LADS was used to take data in the $\pi M1$ area at PSI. Individually tagged π^+ 's were incident on the detector at a rate of about 3×10^6 /s. A combination of scintillators defined a clean beam with a rate on the order of 1×10^5 /s. The numbers of charged and neutral particles detected were counted in hardware, and a fraction of each possible combination was written to tape. In this manner events which were more potentially interesting could be emphasized. The final rate at which events were written to tape varied between 150 and 500/s.

The overview of the LADS detector is now complete. Following will be a more complete description of the major detector components.

2.3 Scintillators and PMT's

The choice of scintillating material for LADS was made from various plastics, NaI, BGO, and glass. The final choice of plastic has a number of advantages: It can handle the rates necessary for tagged pion absorption studies; it has both a high light output per MeV deposited energy and

a long radiation length, enhancing the resolution of the detector; it has a reasonable neutron detection efficiency; and finally, it is stable, easy to work with, and not overly expensive. There are some associated disadvantages as well: Plastic scintillator is relatively light, which means more material is required to stop highly energetic protons; also, it has a relatively low γ detection efficiency which makes π^0 detection more difficult. Bicron-408 [87] was chosen for the scintillating material.

When an energetic charged particle passes through plastic scintillator it ionizes the organic components. The resulting electron "holes" are filled from the electron sea in the material. When these sea electrons de-excite they emit photons, or scintillation light. This light could be directly detected by the phototubes, but it is at a characteristic wavelength of the bulk of the scintillator, which means it is being constantly reabsorbed and re-emitted. This hampers its travel through the scintillator to the phototube. For this reason the scintillator is doped with a wavelength shifter. These complex molecules absorb light emitted by the scintillator and then re-emit it at another frequency which passes directly through the scintillator. Generally, the wavelength shifters are chosen so that the re-emitted light is at a frequency which maximizes the response of the phototubes.

A photo-multiplier tube, also referred to as a phototube or a PMT, has several major components enclosed in a vacuum tube. Photons from the scintillator encounter the front face of the vacuum tube which has been coated with a photosensitive cathode held at a highly negative potential. Some of these photons knock loose an electron which is accelerated in an electric field towards the first of a series of dynodes held at progressively higher voltages. Typically the potential difference between successive dynodes is around 150 V and there are about ten stages altogether. When the first electron strikes the first dynode it knocks loose several more electrons which are then accelerated towards the next dynode where the process repeats, amplifying the signal. After the last dynode, the resulting electron shower is collected by an anode at ground potential. A signal can be taken from one of the late stage dynodes or off of the anode. In the former case it will be a positive signal since there is a net flow of electrons outwards from a dynode, in the latter case it is negative since the anode collects the electron shower. In either case, it will be directly proportional to the number of photons which originally impinged on the photocathode.

2.3.1 Cylinder

The bulk of the scintillator is incorporated into the cylinder. The scintillator's thickness of roughly 45 cm was determined by the desire to stop 200 MeV normally incident protons, which is approximately the maximum energy a proton can have following three-nucleon absorption of a 165 MeV pion. The cylinder has an active length of 160 cm and an inner radius of 30 cm.

The cylinder is divided into 28 independent trapezoidal sectors, each of which has its sides 6.4° off of normal from its face to ensure a tight fit. This granularity is required to minimize the probability of two particles entering the same sector in multi-particle absorption events. Having 28 sectors reduces the probability of this occurrence to under 6.6% for a four nucleon phase space distributed final state. The scintillator in each sector was further sub-divided into three pieces. The innermost 0.5 cm acted as a dE detector (labelled CD for cylinder-delta) and was used primarily for trigger information and particle identification. The remainder was sub-divided into two E-blocks to improve the cross sectional match to the face of a phototube, and thus to improve light collection. The inner (CI) was 25 cm thick, and the outer (CO) was 20 cm thick. The inner and outer E-blocks were separated by 3 cm of empty space to allow for the possible future insertion of γ -converters.

Each scintillator bar was attached to two photo-multiplier tubes. The use of two tubes on each bar was necessary for several reasons. First, the resolution of the readout is determined by the number of photons which impinge on the PMT's photo-cathode. By reading out both ends of the block, approximately twice the number of photons will be collected (for a track passing through the center of the block) giving a factor of $\sqrt{2}$ improvement in resolution. Second, although the chosen scintillator has a relatively long attenuation length (λ), attenuation of the light is still an important effect. The number of photons a distance x from the interaction point follows the following formula:

$$N = N_0 \times e^{-\frac{x}{\lambda}}$$

where N_0 is the original number of photons emitted. If we form the geometric mean of the number detected at each end of the scintillator material, we obtain:

$$\sqrt{N_0 e^{-\frac{x}{\lambda}} \times N_0 e^{-\frac{L-x}{\lambda}}} = N_0 \times e^{-\frac{L}{2\lambda}}$$

where L is the total length of the scintillator. This is proportional to the initial number of photons, and thus the energy deposited, while being independent of position. Finally, having measurements of the time the light reaches each end of the scintillator allows the calculation of

the time at which the light was deposited in the scintillator (independently of position) as well as the position along the block at which the light was deposited.

The light guides connecting the E-block scintillators to the PMT's were constructed from UVT. They were designed to optimize the light collection. It was especially important that the characteristics of the light collection be independent of the position along the scintillator bar. Extensive use of Monte Carlo simulations and testing of prototypes resulted in a design incorporating a 20 cm extension to the scintillator with the same cross sectional shape. A 5 cm long cylindrical piece of UVT was used to attach the 5" Hamamatsu PMT to the light guide so that a μ -metal magnetic shield could extend past the face of the tube. This design had to be modified for the inner cylinder E-blocks where the lack of space required adjacent PMT's to be different distances from the scintillator. Thus, light guides of varying length were used, allowing the PMT's to be staggered.

The light guides for the dE's were also made of UVT but they had to have a significantly different design from those of the E-blocks since the phototubes had to be at a larger radius than the scintillators, allowing room for the insertion of the endcaps and the outer MWPC. Several designs were tested including adiabatic twisted strips, fish-tails, and optical fiber. The adiabatic twisted strips were chosen because they transmitted the most light.

Several PMT's were tested to determine which had the most suitable characteristics. The determining factors for the E-blocks were the available sizes and the timing resolution of the tubes. The size was important as a relatively large tube was required to cover as much of the cross sectional area of the scintillator as possible. The timing resolution limits the calculation of TOF's for the particles as well as the calculation of the axial position at which the track passed through the E-block. The time at which the light is detected by the up and downstream phototubes can be related to the particle's TOF, the position at which it hits the scintillator (x = the distance from the upstream phototube), and the speed that light travels up the scintillator by the following formulae:

$$t_u = \text{TOF} + x \cdot c_{\text{scint}}$$

$$t_d = \text{TOF} + (L - x) \cdot c_{\text{scint}}$$

These equations can be solved for the TOF and the position:

$$\text{TOF} = \frac{1}{2}(t_u + t_d - L \cdot c_{\text{scint}})$$

$$x = \frac{1}{2c_{\text{scint}}} (t_u - t_d - L \cdot c_{\text{scint}})$$

Thus the timing resolution determines the resolution of these measurements. The 5" tube from Hamamatsu (R1250) was found to be the most suitable for LADS.

For the dE's there were several available PMT's with suitable radii, and the timing characteristics of the tubes were the deciding factor. The 1" Hamamatsu R1355 was selected. A timing resolution of 0.7 ns (FWHM) was obtained from these tubes when coupled with the light guides and scintillators.

The trapezoidal shape of the scintillators and light guides was designed so that they fit closely together in a barrel shape. Each sector was wrapped with one layer of aluminum foil to keep out exterior light and to improve the light transmission characteristics. The blocks were also separated by one layer of aluminized mylar to protect the relatively fragile aluminum foil. The blocks were then organized into cylinders and held together by metal bands wrapped tightly around the light guides. The inner cylinder was supported by several metal spacers between the light guides of the inner and outer cylinders. The outer cylinder rests on a chassis with semi-circular supporting arms, which holds all of the LADS components together in a mechanically solid design.

The dE's were supported by attaching the light guides to metal rings positioned at the entrance and exit from the cylinder. In addition, 2" wide flaps from the aluminized mylar separating the E-blocks were wrapped at intervals around the dE's to prevent them from bowing in the center.

2.3.2 Endcaps

The active region of the cylinder covers approximately 93% of 4π solid angle. Of course, close to the edges the thickness of the scintillator is small, so the effective covered region is closer to about 88%. To bring this percentage close to 100%, scintillating endcaps were designed to plug the openings of the cylinder (see figure 2-2).

The constraints on the endcaps due to the available space were quite severe. It was necessary to provide entrance and exit ports for the beam, and for the scintillators to fit inside the openings at the end of the cylinder. For these reasons, the natural design was like that of a cannon-barrel.

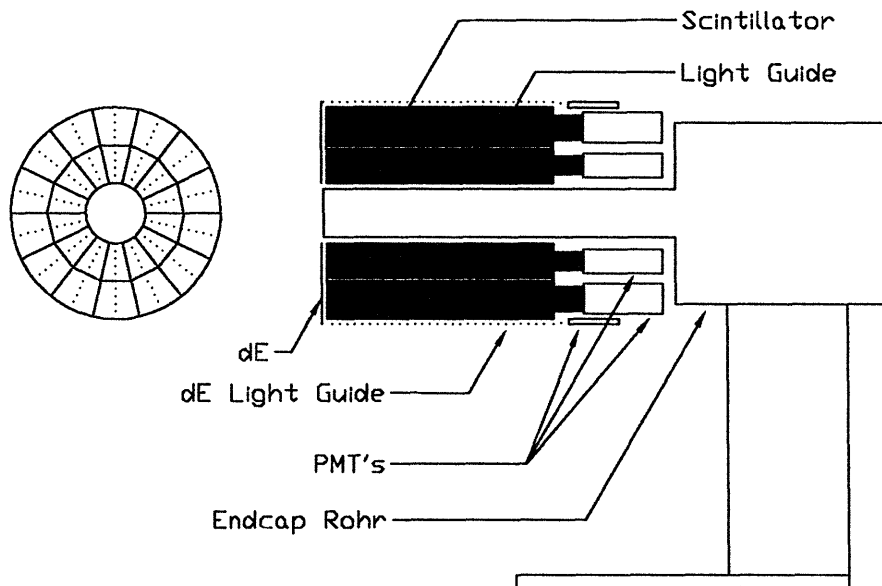


Figure 2-2: The downstream endcap.

The endcaps were divided azimuthally into 14 sectors, each with four separate scintillating components. The bulk of the scintillator in the endcaps was incorporated into the E-blocks. As for the cylinder, the E-blocks were divided into two pieces in order to provide better light collection. The inner E-blocks (EI) consisted of trapezoidal blocks of scintillator 8.0 cm thick, with a curved inner edge of 3.9 cm, and a straight outer edge of 7.5 cm. The outer E blocks (EO) had dimensions of 9.0 cm thick, with a straight inner edge of 7.5 cm and a curved outer edge of 11.5 cm edges. The downstream endcap's E-blocks were 40 cm long, while the upstream endcap's E-blocks were 30 cm long. This difference in length is explained by the fact that particles moving along the direction of the incident pion's momentum tend to have higher energies than those moving against its direction.

The E-blocks were wrapped in aluminum foil with one layer of aluminized mylar separating adjacent blocks. Simulations resulted in the choice of a 20 cm length of UVT with the same cross sectional shape as the scintillator for the optimal light guides. A 7 cm cylinder of UVT attached these extensions to the PMT's. Similar criteria were used to choose these PMT's as were used for the cylinder tubes. Philips XP2312B 3" tubes were used for the outer E-blocks, and Philips XP2262B 2" tubes were used for the inner E-blocks.

The front face of each endcap was covered by 0.5 cm thick scintillators which acted as dE counters (ED). These were also divided into 14 sectors and were trapezoidally shaped with

curved inner and outer edges. They had an inner edge of 3.9 cm, an outer edge of 11.5 cm, and were 17.0 cm in length (measured radially). Each sector covered 25.7° in azimuthal angle, like the E-blocks. They were, however, offset by 12.85° with respect to the E-blocks. This allowed the scintillators to determine the phi angle of a charged particle with a higher precision than if they had not been offset. The dE's were attached to light guides via sharp 90° bends (with mirrored beveled edges). The light guides were 0.5 cm thick and extended the entire length of the endcaps. They were then fish-tailed and attached to $1\frac{1}{8}$ " Hamamatsu R1355 PMT's.

Positioned between the inner E-blocks and the mounting tube were curved 0.5 cm thick scintillators used as veto counters, intended to determine if a charged particle entered the endcap E-blocks without passing through the dE's. They were attached by light guides to $\frac{3}{4}$ " Hamamatsu R1450 PMT's. The tubes proved difficult to obtain clear signals from, partially due to their complete inaccessibility during the run. They were not incorporated into the data analysis except for periodic use as diagnostic tools.

The support structure consisted of a steel mounting tube 7.9 cm in inner radius, tapering from 0.3 to 1.0 cm thick. This is attached concentrically and end-to-end to another steel cylinder 17.4 cm in inner radius and 1.0 cm thick. This unit was attached to a platform that moved smoothly on rails, allowing the endcap to be inserted and removed from the cylinder with ease. The scintillators, light guides, and PMT's were packed tightly around the mounting tube and secured with bands of strapping tape.

2.3.3 Readout

The dynamic range that the E-blocks and their readout electronics needed to handle was determined from the relevant physics. The low energy threshold was determined from the need to detect the light emitted by charged particles which had been scattered by neutrons. The neutron detection efficiency is a strong function of the threshold. It was determined from Monte Carlo simulations that 2.5 MeV electron equivalent light was a reasonable minimum. Of course, this amount of light must be detectable anywhere along the block, and attenuation from one end of the scintillator to the other is about a factor of two, so 1 MeV equivalent light is the actual minimum. The maximum is determined by the most light that can be deposited near a scintillator. The somewhat unrealistically high value of 400 MeV electron equivalent light was used for safety by the collaboration in its estimates. Thus, a dynamic range of 400 needed to be covered.

The PMT's used in the LADS detector have custom designed passive bases and were run at high voltages varying from 1300 to 1800 V. The 5" tubes used for the cylinder E-blocks were read out from a dynode and emitted a positive pulse. The other tubes were read out at the anode. All signals were transported to the electronics shack via 100 ns coaxial cables. The positive signals were passed through inverting transformers, and then all signals were amplified by PSI designed $\times 10$ Fast Amplifiers.

After being amplified, the signals were fed into PSI designed fastbus modules called FDMT 100's (Fast Discriminator and Mean Timer). Unfortunately, problems with the module's voltage supply prevented the mean timers from being implemented. Each 32 channel module was double width and had two separate sub-boards. The analog board contained adjustable amplifiers which were set to provide $\times 0.3$ and $\times 0.4$ outputs. The digital board had constant fraction discriminators with three separately driven NIM logic outputs. Two of these outputs were delayed by 300 ns to allow time for the data acquisition (DAQ) system to be activated. The FDMT's also incorporated high-pass filters which removed noise with frequency < 1 kHz. The careful attention paid to noise in the system allowed the discriminators to be set at the low value of 15 mV. Combined with the various amplifiers in use, this value corresponded roughly to the required threshold of 2.5 MeV electron equivalent light. The saturation level of the PSI Fast Amplifiers at 6 V then fixed the dynamic range at 400.

The analog signals ($\times 0.3$ or $\times 0.4$ depending on the class of counter) were sent via 300 ns cables (for delay purposes) to LeCroy Fera ADC's. The ADC's reported only those channels which were above a preset pedestal level to the DAQ system (see section 2.8). The non-delayed logical outputs were sent to the trigger electronics (see section 2.7). One set of delayed logical outputs was connected to Phillips Scientific Fastbus ADC's model 10C6 and daisy chained to Phillips Scientific Fastbus Latches model 10C8. Some of the remaining logic signals were sent to scalers for monitoring the detector operation.

2.4 Multi-Wire Proportional Chambers (MWPC's)

Trajectory information for charged particles in LADS was provided by two concentric cylindrical multi-wire proportional chambers. A proportional chamber consists of an anode wire held at a highly positive potential between two cathode planes. The planes are separated by about 1 cm, and the interior space is filled with a gas. When an energetic charged particle passes through the chamber it ionizes some of the molecules in the gas, producing electrons which drift towards

the anode and anions which drift more slowly towards the cathodes. In the immediate vicinity of the anode wires the field intensity increases sharply, accelerating the electrons to the point where they also ionize gas molecules, creating an avalanche of electrons and a large number of anions slowly drifting towards the cathodes. The actual charge collection occurs too quickly to be measured, but the motion of the anions induces a change in the potential difference between the anode and the cathode resulting in a detectable signal.

In a multi-wire proportional chamber, many anode wires are strung about 2 mm apart between the cathode planes forming an anode plane. The cathode planes can also be constructed of segmented pieces providing position information. This segmentation is usually achieved by constructing them from strips. These strips are orientated at a non-zero angle with respect to the anode wires, so that positions on the chamber plane can be calculated from the crossings. The induced signal tends to be over one or two anode wires, providing localized position information. However the signal can be spread out over 2-3 cm of cathode strips (typically five strips for LADS). It will have different strengths on each, however, and the weighted mean of the strength on each strip can be calculated, determining the hit position accurately.

The LADS chambers are shown in figure 2-3. The outer chamber had a 28 cm anode radius and a 160 cm active length. It rested inside the cylinder and covered the entire active region of the cylinder scintillators. The two endcaps were inserted inside the outer chamber. They were positioned so that the back ends of the endcap E-blocks were aligned with the edges of the cylinder's active region. This left a 90 cm distance between the endcaps. The inner chamber had a 6.4 cm anode radius, and a 90 cm active length. It was inserted into LADS through the endcap mounting tubes and rested between them. Its active length covered the entire region between the endcaps. All particles originating at the target and passing through a dE had to pass through the inner MWPC. Those particles entering the cylinder passed through both MWPC's.

A chamber consisted of several layers. Listing them from the smallest radius to the largest, they were:

- 1) A grounding foil of aluminium coated Kapton
- 2) A layer of epoxy
- 3) A rohacell cylinder
- 4) A layer of epoxy

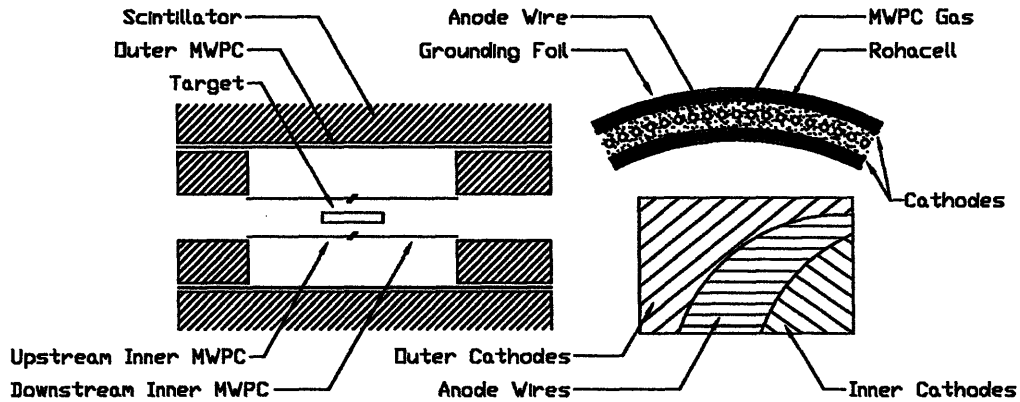


Figure 2-3: Three views of the MWPC's are shown. The left-most shows the position of the chambers in the detector. The top-right shows an end-on view of a slice through a chamber, and the bottom-right shows the orientations of the cathode strips and anode wires.

- 5) A cathode plane
- 6) Free space
- 7) The anode wires
- 8) Free space
- 9) A cathode plane
- 10) A layer of epoxy
- 11) A rohacell cylinder
- 12) A layer of epoxy
- 13) A grounding foil

Table 2.2 gives relevant technical values for the important layers.

The anodes consisted of 10 micron radius gold-plated tungsten-rhenium wires stretched between two stesolite support rings. The anode wires were spaced 0.21 cm apart. There were 832 in the outer chamber and 128 in the inner chamber. In addition, the outer chamber's anodes were attached to a rohacell ring at the center to provide additional mechanical support. The cathode foils were constructed from 50 micron thick Kapton foil with a 0.2 micron layer

MWPC Specifications	Inner MWPC	Outer MWPC
Radius	6.4 cm	28.0 cm
Number of wires	192	832
Wire spacing	2.094 mm	2.114 mm
Number of cathode strips	384	560
Cathode strip width	2.7 mm	3.8 mm
Cathode spacing	0.6 mm	0.6 mm
Strip angles (inner, outer plane)	34.25°, 41.19°	45.86°, 44.21°
Anode-cathode gap	3 mm	4 mm
Anode HV	≈ +2350	≈ +2800

Table 2.2: Relevant MWPC parameters, from reference [20].

of aluminum sputtered on one side. The strips were made by scratching the surface with a dentist's drill held by a large Hewlett-Packard computer plotter.

The outer chamber had 560 cathode strips divided between the inner and outer cathode layers. These strips spiraled around the z-axis of the detector at an angle of roughly 45°, with those on the inner plane spiraling in the opposite direction from those on the outer plane. This geometry meant that no two strips crossed more than twice over the active region of the chamber, helping to minimize the ambiguity in the determination of the hit location. The pitches of the cathode strips were not exactly equal for those on the inner and outer plane, so that the two crossings were not exactly 180° apart. This was necessary since several of the reactions occurring in the target have the characteristic that the outgoing particles are back-to-back in phi. Both the anodes and cathodes were read out, with the cathode strips used to calculate the hit position and the anodes used to resolve any ambiguities from multiple crossings.

If the inner chamber were designed in the same manner, a problem would arise. The small radius would cause some pairs of strips to cross four times over the active length. This ambiguity would complicate track reconstruction. It was solved by a combination of two modifications. First, the cathode strips spiraled at a pitch less than 45° (see table 2.2). Second, the cathode planes were split in the center by etching a ring in the foil. The cathode strips then had to be read out at both ends, essentially resulting in two separate MWPC's that shared anode wires. Incorporating these changes resulted in no pair of strips crossing more than twice.

Choice of gas used in a wire chamber has a large effect on the amplification achieved in the vicinity of the anode wires. The gas used for LADS was a mixture of 49.8% C₂H₆, 0.2% freon,

and 50% argon which was continuously circulated. The argon is the component that ionizes creating the avalanche. The ionization energy of argon is high enough, however, that photons from the anions capturing electrons are energetic enough to ionize other atoms, leading to a continuous discharge. The C_2H_6 acts as a quencher, absorbing these photons and preventing a continuous discharge from occurring. The small amount of freon also acts as a quencher, but it also captures electrons emitted from the cathodes before they can start additional avalanches themselves.

The high voltages were supplied by negatively-grounded, highly stabilized Heinzinger HV power supplies. The cathode strips were held at ground potential, while the anodes were at HV. Built into the MWPC's themselves are capacitors to isolate the high voltage of the anode wires from the readout system, and resistors between the anode wires and ground to drain off any accumulating charge.

The anode wires were read out by the LeCroy PCOS III system which reported the centers and widths of clusters of adjacent wires. The signals from the cathode strips were amplified by LeCroy TRA1000 current sensitive preamplifiers in the area, and then again by PSI designed post-amplifiers in the electronics shack. The signals were read out by LeCroy 2282B CAMAC ADC's. The LeCroy 2280 module was used to subtract pedestals and to select only channels above an adjustable threshold to present to the DAQ system (see section 2.8).

2.5 Target

The choice of targets for LADS was made between high-pressure gas, cryostatic liquid, and room temperature solid materials. Because a substantial motivation for LADS was the study of absorption on the helium isotopes, one of the first two types had to be developed. Space considerations precluded the installation of refrigerator machinery, so a high-pressure gas target was selected. Once such a target had been constructed, it was simpler to restrict all the targets to gasses instead of separately developing solid targets for heavier nuclei.

Several factors were of importance in the design of the target. The overriding goal was to have the largest possible target thickness while minimizing background reactions and the energy losses of particles following absorptions. The target wall material had to be strong enough to contain the pressures involved, while being light enough to limit the number of background reactions. Carbon fiber provided these qualities with the additional benefit that a rupture

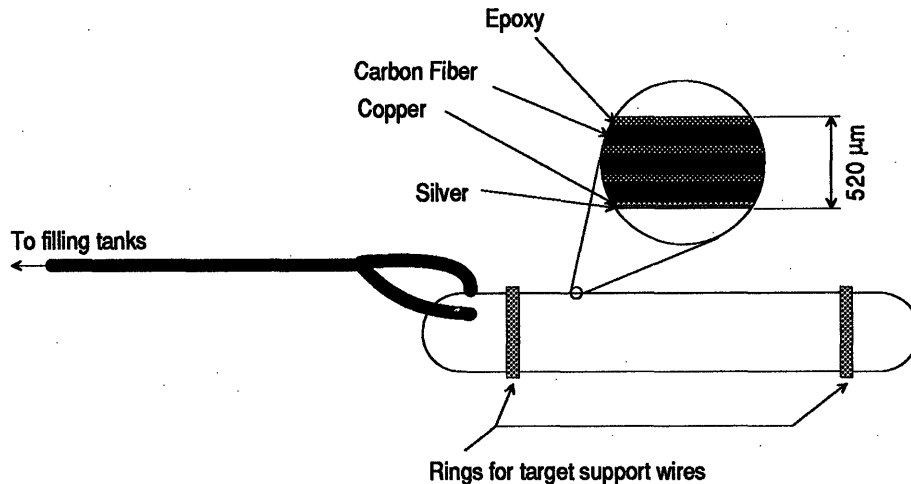


Figure 2-4: The high pressure gas target [19].

would result in a slowly increasing loss of pressure rather than an explosive decompression. The length and radius of the target were determined by balancing the desire to have as much target gas thickness as possible while limiting the effects of multiple scattering. Multiple scattering in both the target endcaps and target gas disperses the beam. A longer target would have resulted in more beam pions impinging on the walls, and thus a greater background-to-signal ratio. Monte Carlo simulations of this effect led to the choice of the dimensions used.

The gas target used was designed by the LADS collaboration and constructed by Dornier Ltd. [88]. The target (see figure 2-4) has a length of 25.7 cm, and an inner radius of 2 cm. The walls are constructed of three layers of carbon fiber each 120 microns thick, alternating with three layers of epoxy each approximately 45 microns thick. The ends of the cylinder are closed off by endcaps which are segments of a sphere of 3 cm radius. The regions where the endcaps attach to the cylinder are reinforced by an additional 0.1 cm of carbon fiber-epoxy sandwich.

The interior surface of the target was made gas-tight by galvanically coating it with 10 microns of silver and 20 microns of copper. The existence of this lining affected the choice of target gasses as some possibilities might have reacted with it. With the exception of ^2H , only noble gasses were used. Two stainless steel 0.3 cm pipes were mounted at the downstream end of the target for filling purposes. The pipes were attached in the reinforced region, which was further reinforced in the immediate vicinity to a thickness of 0.3 cm. As built, the target could safely contain pressures of 100 bar. The actual pressures used during 1991 were approximately

75 bar for ^2H , 95 bar for He, 40 bar for N, and 30 bar for Ar. The heavier materials had to be filled at a lower pressure both because their weights would cause the target support system to sag and to limit the energy loss of the outgoing particles. The target was suspended in the middle of the detector on three thin steel wires.

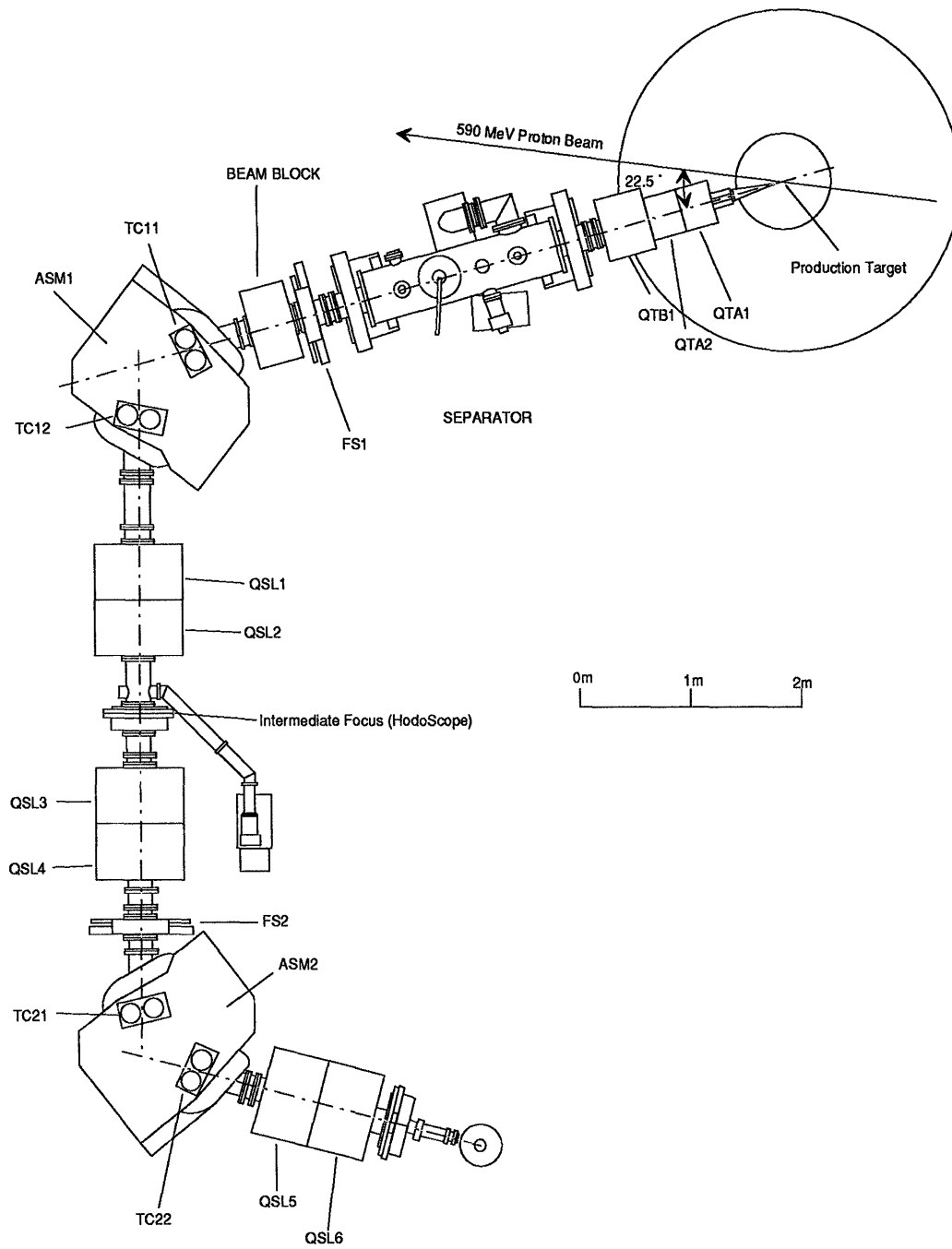
The feature that the carbon fiber has of not rupturing explosively was tested near the end of the 1991 run when a leak developed. For the last few days of the 1991 run and the entire 1993 run the backup target was used. This was constructed in a similar manner, but with slightly thicker walls.

2.6 The Pion Beam: Creation and Definition

The definition of the pion beam was accomplished by a combination of scintillation counters and the cyclotron's RF signal. The experiment was conducted in the πM1 area at PSI. Figure 2-5 shows a picture of the beamline. The cyclotron produced 590 MeV protons in a 50 MHz microstructure. The protons from the cyclotron are directed at a beryllium production target. Outgoing particles at 22.5° are selected and initially pass through a series of three focussing quadrupoles. The particles next pass through a 2 m long electrostatic separator which selects charged particles according to their velocities by balancing static E and B-fields. Compensating magnets incorporated into the electrostatic separator refocus the particles.

The particles then encounter a series of two bending dipoles and six focussing quadrupoles which select charged particles according to their charge and momentum, and focus them on the experimenter's target. The combination of selecting particles based on their velocities and on their momenta allows for the selection of particular particle types. Finally, the selected pions pass through the beamline vacuum system's exit window.

The beamline is capable of delivering pions from 110-560 MeV/c with a momentum resolution of 5×10^{-4} and a momentum acceptance of $\pm 1.4\%$. The pion momentum can be measured within the acceptance by using a hodoscope consisting of 64 scintillating strips located at the intermediate focus. In the range of momenta used in this experiment, the maximum attainable pion flux is approximately $2 \times 10^7/\text{s}$. This rate was limited in this experiment to approximately 3×10^6 by adjustable slits in the beamline. The pions can only appear at 20 ns intervals due to the cyclotron's RF. The shape of the beam was monitored during the run using a pair

Figure 2-5: The π M1 channel at PSI.

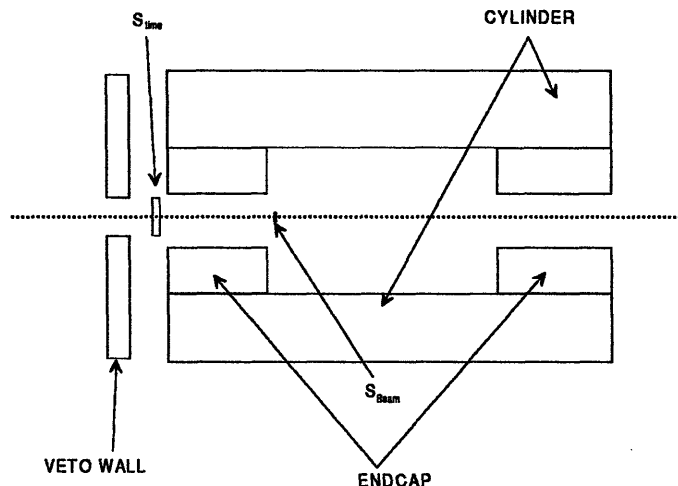


Figure 2-6: A diagram of the beam defining scintillators.

of integrating multi-wire proportional chambers located at the exit window from the vacuum system.

The scintillators involved in defining the beam are shown in figure 2-6. The first in line is the veto wall, designed to minimize the effects of the beam's halo. The veto wall consists of a 20 cm thick wall constructed of lead blocks. It covered the entire cross sectional area of LADS, with the exception of a 10 cm diameter hole in the center for the actual beam. Both the front and the back of the wall are covered with scintillator paddles which were used as a veto in the beam logic.

Next in line is the timing counter, S_{time} , mounted just behind the veto wall at the upstream end of LADS. This is a 12 cm diameter 0.3 cm thick piece of scintillator read out with two Philips XP2020 PMTs. It covers the hole in the veto wall completely, and is used for three main purposes. First, it identifies possible beam particles. Second, it rejects most of the protons, muons, and electrons contaminating the beam through a combination of timing and energy loss characteristics. Third, it was used in the analysis as the basis for calculating TOF's.

The final beam defining counter was S_{beam} . It was a 2 cm diameter, 0.1 cm thick counter mounted at the end of a long cylindrical light guide inserted into the upstream end of LADS. It was read out by a Philips 1/2" XP1911 PMT. Its position was approximately 35 cm upstream of the target entrance window. As it was the smallest counter in radial dimension, and was smaller

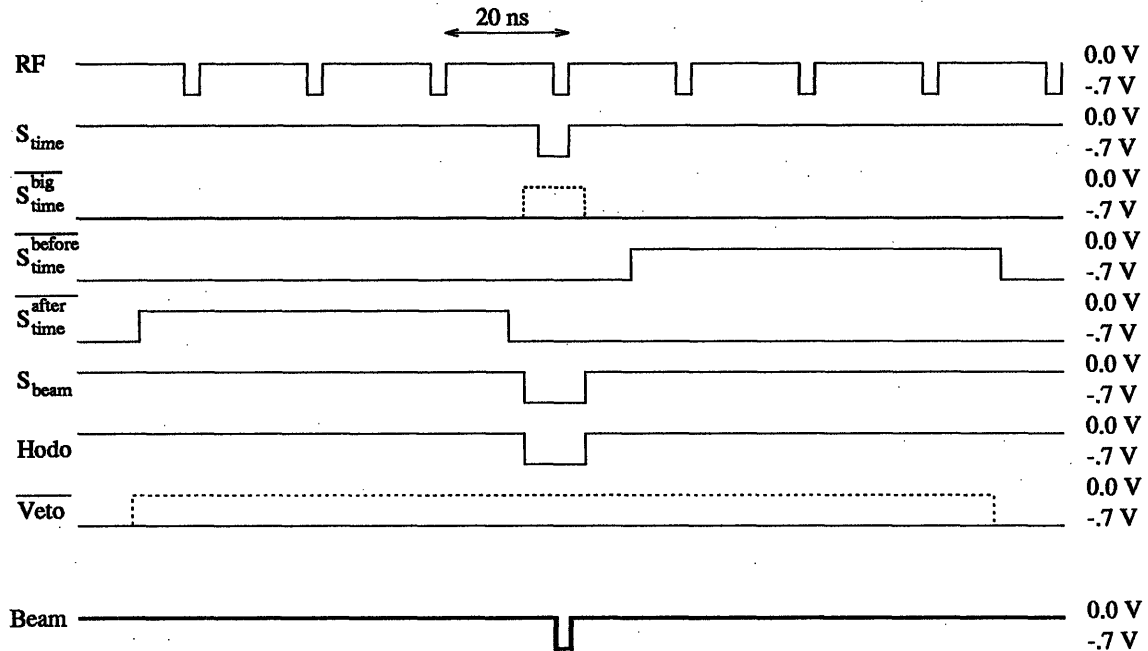


Figure 2-7: A timing diagram for the beam defining electronics [20].

than the beam, it determined the shape of the beam's profile. Since the target's diameter was 4 cm, most of the beam passed within the target's walls.

Signals from the beam defining counters were conveyed to the electronics shack by shorter cables than the other LADS scintillators in order to give a lead time for constructing the beam strobe. In addition, the cables for S_{time} were thicker than normal in order to minimize the dispersion and thus provide better timing resolution. The logic describing the definition of the beam is:

$$\text{Beam} = S_{\text{beam}} \cdot S_{\text{time}} \cdot \text{RF} \cdot \overline{S_{\text{time}}^{\text{big}}} \cdot \text{HODO} \cdot \overline{\text{VETO}} \cdot \overline{S_{\text{time}}^{\text{before}}} \cdot \overline{S_{\text{time}}^{\text{after}}}$$

Since the electronics layout is relatively simple and based mainly on timing, a timing diagram appears in figure 2-7. For NIM electronics, a signal at 0 V is false while a signal at -0.7 V is true.

The "logical beam" was defined when there was a coincidence between S_{beam} and S_{time} with the following constraints. First, in addition to pions in the beam there is contamination from electrons, muons, and protons. These will in general have different flight times from the

pions and can be separated by time-of-flight. This was done by requiring a coincidence with the cyclotron RF, delayed by the right amount to select the pions and exclude the others. Second, there were events in which multiple pions came in the same beam burst. Since LADS was counting individual pions for its normalization, these events needed to be vetoed. This was done by checking the amount of energy deposited in S_{time} . A discriminator was set to fire if more energy was deposited than usual for a beam pion. The inverse of this signal was put in coincidence with the others ($S_{\text{time}}^{\text{big}}$). In addition to vetoing events which had multiple particles, this also vetoed any protons which may have passed the previous tests.

Third and fourth, the signals from the hodoscope (HODO) and veto wall (VETO) were added. The veto wall pulse was set to a large width so that no halo particles passed into the detector for the prior three beam bursts or the following three, in addition to the current beam burst. Finally, in addition to vetoing on halo particles from nearby beam bursts in the detector during legitimate events, it was necessary to veto events where another pion entered the detector within 70 ns of the current particle. This was because events would not be separable if they occurred so closely spaced. Such events were vetoed by adding in coincidence an inverted, 70 ns wide pulse from S_{time} with extra delay ($S_{\text{time}}^{\text{after}}$; to veto the event if there was an earlier pion) or less delay ($S_{\text{time}}^{\text{before}}$; for a later pion).

This coincidence, labeled “beam” in the figure, was called the “beam strobe” or the “logical beam”. It strobed the trigger electronics, and was used to set the timing for the electronics (with the start determined by the RF). The defined beam rate varied as a function of several factors including the pion energy and the cyclotron’s output. A typical rate was $1 \times 10^5/\text{s}$.

2.7 Trigger

The events of interest in this experiment are those which originated in the target region and have multi-particle final states with no pions. These events are a small fraction of the events detected by LADS which are dominated by pion scattering. In order to obtain enough events on tape for analysis, it was necessary to select a subset of detected events to be written. For this reason a trigger was designed for LADS. The trigger had to be fast, since only about 300 ns were available to make the decision as to whether to activate the data acquisition system. It also had to be “clean”; *i.e.*, it had to select events in an unbiased and known manner from all possibilities.

It would be ideal to be able to select events coming only from the target region, since over half of the reactions in LADS are from S_{beam} , the target windows, and the air. Unfortunately, the vertex reconstruction was performed using MWPC information which needed to pass through amplifiers, ADC's and the PCOS system. These components are relatively slow and the MWPC's did not provide information quickly enough to be used in a trigger. For this reason, the data written to tape had to have a sizable background from events which occurred outside of the target region.

Unlike vertex reconstruction, it would be conceivable to perform some basic particle identification tests on the outgoing particles to reject events which definitely have a pion in them. Examples of such a test would be a very low level cut on the amount of energy deposited in the dE's or a timing cut to reject very fast particles. In both cases, the goal would be to reduce the number of events with pions in the final state while leaving the events with no pions either unaffected or affected in a known and correctible way. Unfortunately, due to effects in the detector like the resolution of the dE's and noise, it would be difficult to be completely certain of the effects such cuts would have. For this reason, this technique was deemed too risky for the gains.

A remaining possibility is to work with the number of particles detected in LADS. It is possible to separate and count the numbers of charged and neutral particles very quickly in the hardware. Then the numbers for an event can be compared to a predetermined matrix of relative importances, and a desired fraction of each possible type written to tape. It is important that the selection of each possible type written not be influenced by any other factors, so that the data on tape are an accurate representation of the events in question. Then the data can be corrected during analysis by simply weighting each event by the requisite factor.

A charged particle was identified for purposes of the trigger when a dE fired. A cylinder neutral particle was identified when an E-block fired and the dE in front of it did not. An endcap neutral particle was identified when either the inner or outer E-block in a sector fired, and neither of the dE's partially covering it fired. Clearly this scheme is not perfect. For example, it miscounts single charged particles which pass through the endcap and enter the cylinder as two particles. A more complex scheme was used in the analysis to identify particles more accurately, but this quick method was suitable for the necessarily fast trigger electronics. Its imperfections are not important since the number of charged and neutral particles counted by the trigger were recorded by latches, and the events were corrected according to the trigger types by which they had been prescaled, not the actual number of particles.

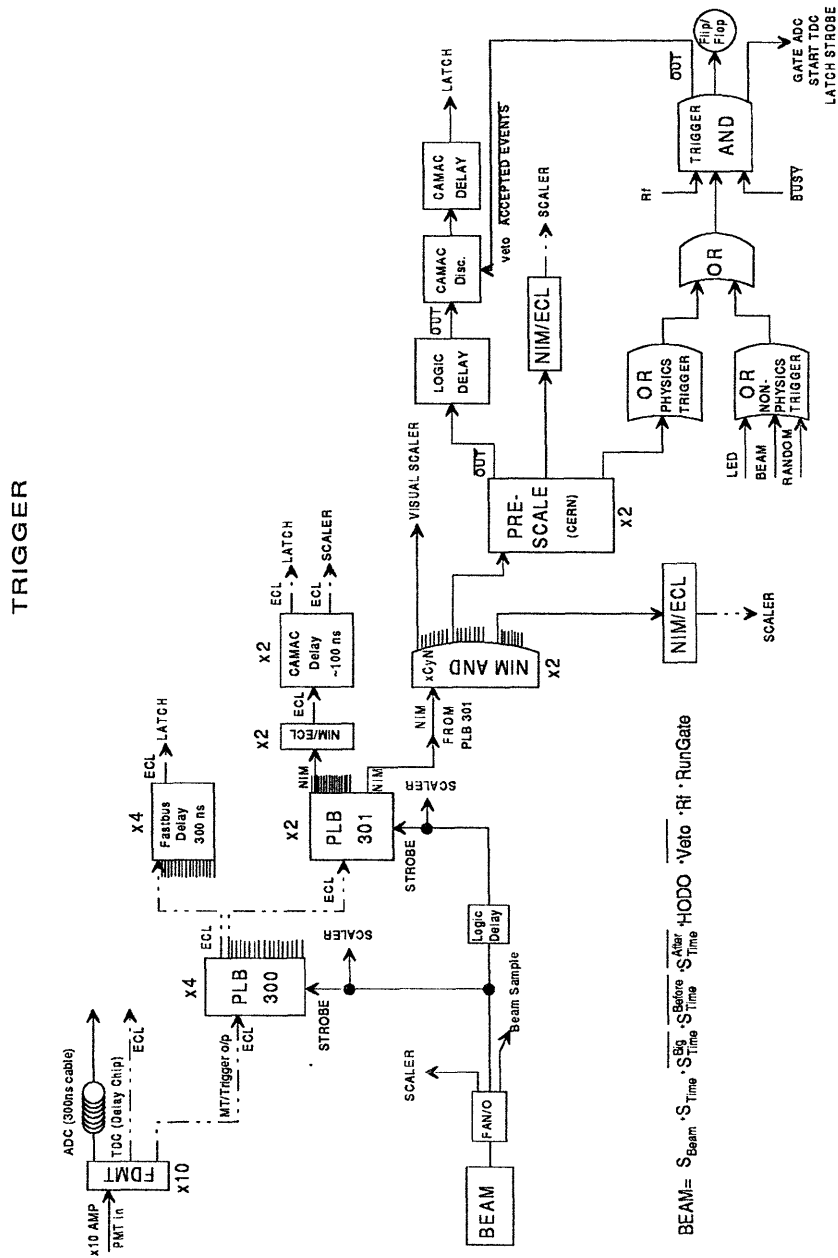


Figure 2-8: A diagram of the trigger electronics, from reference [19].

A diagram of the trigger electronics appears in figure 2-8. The non-delayed discriminator outputs of the FDMT's (see section 2.3.3) were sent to PSI-built Fastbus PLB 300's (Programmable Logic Boxes) which identified whether there was a charged or a neutral particle in the sector. The outputs of these went to PLB 301's which counted the number of charged and neutral particles present in the detector. All the PLB's were strobed by the logical beam and thus were only activated when a single pion entered the detector. The entire trigger, including the definition of the beam, was formed in about 200 ns.

The multiplicities determined above were used to form eight different triggers using PSI NIM coincidence units. They were $0C1N$, $1C0N$, $1C1N$, $0C\geq 2N$, $1C\geq 2N$, $2C0N$, $2C\geq 1N$, and $3C$. Each of these signals went to CERN prescaling units, daisy chained where necessary to provide an adjustable range from 1 to 2^{16} . The prescaled signals were then OR'ed to construct one overall physics trigger. Typically the interesting and relatively uncommon events like $3C$ were not prescaled at all, while events like $1C0N$ were prescaled by a factor of 512. The others were in between these extremes.

There were three other trigger types used in the experiment. The beam trigger periodically wrote an event in which there was a logical beam signal whether or not anything else was recorded in the detector. The random trigger was a periodic signal from a clock which was uncoordinated with anything in the experiment. The LED trigger wrote LED events to tape. Each scintillator had LED's attached to it which were used to monitor and maintain the stability of the PMT's. The LED's were fired at 1000 Hz to ensure constant signals were measured by the scintillators, reducing effects due to rate variations. A fraction of these events was written to tape.

After these three non-physics triggers were included, the signal was put in coincidence with the inverted computer busy and the cyclotron RF (to restabilize the timing). The main LADS trigger was the result.

The process of determining the trigger was monitored and recorded over its whole path by a combination of latches (which only recorded events written to tape) and scalers (which recorded all events with a logical beam signal). Such care was taken since small errors in the formation of the trigger could be catastrophic for normalization purposes. Especially important were the scalers after the physics triggers had been formed and before they were prescaled because they determined the normalization for the experiment.

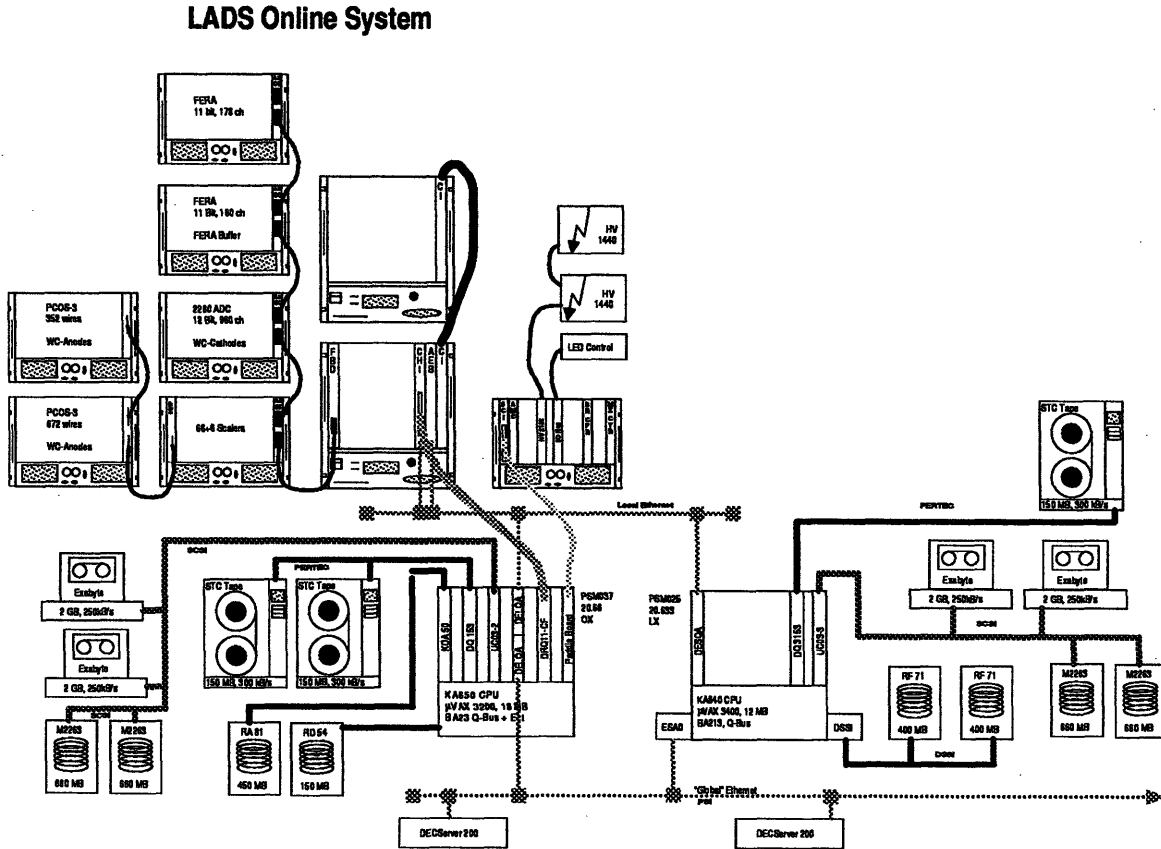


Figure 2-9: A diagram of the data acquisition system.

2.8 Data Acquisition and Storage

The data readout is shown in figure 2-9. The components requiring readout varied between the CAMAC and Fastbus standards. Those in the CAMAC standard were converted to Fastbus via the Struck FBD 320. All Fastbus signals were then read out by a Struck Aleph Event Builder (AEB). The AEB is a programmable processor which gathers and organizes the data into a multiple event buffer for shipment. It is also capable of testing the characteristics of the event. The possibility of using it for filtering events based on a preliminary particle identification was considered and eventually discarded (see section 2.7).

Data transfer from the AEB's buffer to a μ VAX 3600 was handled by a Struck CHI processor and a DRQ-11 DMA interface. The data was stored on 2.5 gigabyte 8 mm Exabyte tapes. The

event rate to tape depended on the average size of the events which in turn depended on the target, energy, and prescale factors. It averaged about 200/s. Later improvements in the DAQ system boosted this to as high as 500/s.

The μ VAX 3600 performed a variety of other tasks such as controlling the PMT's high voltage and the LED monitoring system. A second μ VAX also sampled the data stream which allowed for the online analysis and monitoring of the incoming data. As the analysis software was in the process of development over the course of the run, the amount of available useful information varied with time; however, quantities like multiplicities and event vertices were usually available. An automatic diagnostic system was also installed which filled histograms and periodically compared them to reference histograms, warning the shift crew of any major discrepancies.

Chapter 3

Analysis Software and Performance

The amount of effort required to program the analysis system is often significantly underestimated during the planning stages of an experiment. LADS has upheld this tradition. Thousands of man-hours have gone into developing the main analysis package Ladybird, not including the various simulations developed and modifications to histogramming packages.

Ladybird consists of about 500 subroutines which can be divided into several major elements, diagramed in figure 3-1. The data collection package samples the data from the stream between the hardware and tape during online analysis and reads the data directly from tape for offline analysis. Run control monitors the status of the run and allows for the use of different parameters for different conditions. The "physics" package handles such tasks as calibration, track reconstruction, particle identification, *etc.*. Finally there is the testing and histogramming package which handles the output of the system.

Data in Ladybird are manipulated in a series of common blocks which define areas of storage that can be accessed by many different subroutines. The main common block is called the "xl_d" which contains over 26,000 variables used by Ladybird. The data collection package accesses the raw data from the latches, TDC's, and ADC's which is then copied into the xl_d. Other packages access the data, make calculations, and then insert the results in new locations in the xl_d. For example, the calibration package forms energy information from the light information stored in the xl_d and then stores energy information.

The testing and histogramming package works with information contained in the xl_d. It is possible to test of the values of different variables and to make geometrical cuts, including linear,

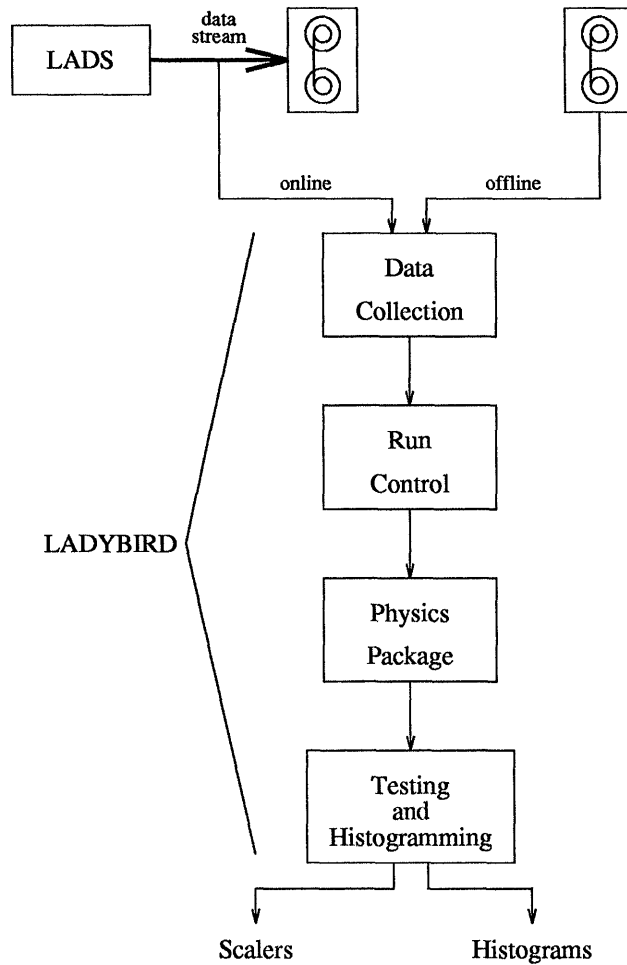


Figure 3-1: A flow of the major components of the LADYBIRD data analysis package.

elliptical, and hyperbolic, on pairs of the variables. One can also form logical combinations of previous tests, including NOT, AND, OR, and XOR. In addition, some xLd variables carry information based on individual bits, so the test package is capable of testing the status of single or multiple bits. Tests are evaluated on an event by event basis. They are used in two different ways: On an event by event basis, histograms are filled with the values of variables if any test is true. In addition, the number of times each test is true is counted during the course of a run and read out as soft scalers (distinct from hard scalers which refer to the contents of electronic scalers in the data acquisition system).

The guts of Ladybird are found in the “physics” package, which is the part the author spent most of his time working on (credit for the development of the other packages goes to collaborators at the University of Basel and PSI). Detailed descriptions appear below for the five major subsections: particle reconstruction, track reconstruction, calibration, particle identification, and loss. The descriptions are of the basic packages, used in all of the LADS analyses. In certain cases these methods have been modified for the specific analysis described in this thesis, but these modifications will be described in later chapters. Not all parts of the physics package are included under the above headings. Some examples of sections which are not described are:

- 1) Latch reconstruction – unsorts the latch information from the convoluted manner in which they are read by the data acquisition system.
- 2) Fixit – corrects the data for known mistakes such as miscablings.
- 3) Monte Carlo input – reads in simulated data for comparison.
- 4) Hardware scaler analysis – monitors the values of the electronic scalers.
- 5) Trigger testing routines – monitors the consistency of the trigger.
- 6) Derval – Calculates derived quantities directly from the plastic information.
- 7) Kinematics – Calculates some standard kinematic quantities used by many collaborators.
- 8) Data filtering – simplifies the analysis by writing out subsets of the data consisting of selected events.

The complexity of Ladybird is shown by the fact that the above list is not exhaustive.

3.1 Particle Reconstruction

The experimenter works with outgoing particles: their numbers, types, energies, and trajectories. A detector supplies information by counters. Particle reconstruction refers to the process in which information from the different detector components is grouped together into “particles”. The first step of particle reconstruction is the determination of which scintillators had light deposited in them. Noise is separated from true information by requiring that all of the electronics associated with a scintillator sector report a particle in that sector. So for a particle passing through a cylinder E-block to be recognized, the latches, TDC’s, and ADC’s for the PMT’s on each end of the scintillator must record its presence. Although it might be possible to reduce thresholds near the ends of the blocks by relaxing these requirements, that would necessitate a much more complicated and frequently inaccurate treatment of these additional particles which would outweigh any gains.

After it is known which scintillators contain information, it is necessary to group that information together into individual particles. This aspect of the code is called “Cylinder-To-Particle” (CTP) for historical reasons. The code has several distinct steps. For the cylinder, the CD, CI, and CO in the same sector are initially combined together. The particle is identified as charged or neutral depending on whether the CD fired. Now either multiple scattering or nuclear reactions can cause a particle to scatter from one sector into another. The likelihood of this occurring is rather high, about 30% for an energetic charged proton. This is much more likely than the possibility that a neutral particle is in a sector adjacent to a charged particle. For this reason, sectors which recorded a neutral particle that are adjacent to charged particles are reconstructed into a single charged particle. The cases in which neutral particles are adjacent are also reconstructed.

The endcaps are slightly different because of the angular offset between the ED’s and the EI’s and EO’s. First a charged particle is identified for each ED hit. Then the light in any of the four E-blocks behind that ED is associated with that charged particle. Finally, any remaining E-blocks are identified as neutral particles, with adjacent blocks grouped together.

The difficult cases involve reconstructing particles that intersect both the endcap and the cylinder, called “punchthroughs” (not to be confused with “punchouts”, which pass completely through the scintillator). First it was determined whether any charged particles entered the cylinder in any of the three sectors behind the endcap sector, thus performing a rough ϕ -cut. If so, a rough cut on the plastic calculated z-position was used to determine if a charged particle passed through the CD in the vicinity of the endcap (within 10 cm of its front face to allow for

the resolution of the method). If both these tests were satisfied the particles were reconstructed into a single particle. Finally, it is possible for a neutral particle to enter an endcap and react, resulting in an energetic charged particle which then entered the cylinder. These cases were reconstructed in a manner similar to that described above.

The above logic for reconstructing particles all follows clearly from the geometry of the detector. There were some cases, however, for which it was impossible to determine exactly what had occurred, and which particles should be grouped. Consider a case in which one CO fired, and the two adjacent CI's fired. It would be difficult, if not impossible, to determine which of the particles should be grouped together. Another example would be if the CD and CO fired for a sector, but not the CI. For events like these, either arbitrary assignments were made, or the event was aborted if this proved too complicated. This treatment was justified by the low frequency of occurrence, which was on the fractional percent level.

3.2 Trajectory Reconstruction

Trajectory information for charged particles was provided by the MWPC's. The output of the MWPC's is in the form of ADC signals for the cathode strips and hit patterns for the anode wires. This information is transformed by a subroutine called *L_Recon* into hit positions on each of the two chambers in terms of ϕ and z locations. This information is combined with the plastic information in a subroutine called *L_Tracks* into particle trajectories in terms of ϕ , θ , and event vertices.

L_Recon begins by identifying the locations of peaks on each of the six cathode planes (two each for the upstream inner, the downstream inner, and the outer MWPC's). First, the effects of noise are mitigated by using a standard noise reduction method of associating with each strip the median of the ADC values of that strip and its neighbors. Then all regions that have mean values above a certain threshold are identified in order to locate regions with possible peaks. Since a peak extends over several strips, typically four or five, it is possible for multiple peaks to be in the same region. The peaks usually approximate a gaussian distribution, possibly with a maximum value cutoff if the saturation level of the ADC's is approached. This allows peaks in the same region to be separated by looking for relative minima in the centers of the regions. If the median values dropped below 75% of the maximum of the values on either side, the region was separated into two regions at that point.

Examination has indicated that noise on the cathode planes usually falls into three broad categories. The most common is single strip variations, which are handled by the use of the medians. The other possibilities are long regions of approximately uniform value or many smaller regions with ADC signals. In these last two cases the maximum ADC values in the noise regions are lower than typical peak values, but can exceed some of the smaller ones. They are handled by restricting the number of peaks on any of the cathode planes to five, and the maximum width of any peak to eleven strips. If either of these limits is exceeded, the minimum ADC threshold used to identify regions is increased, and the procedure for that plane begins anew.

After the regions containing peaks have been identified, their centers are determined by calculating a weighted mean of the ADC values in the region. The actual values are used instead of the medians in order to maximize the precision of the calculation.

After the peak locations have been identified, hit locations are determined for each of the three chambers. All possible permutations of pairing off the peaks on one plane with those on the other are considered. The ϕ position of crossings are calculated for each permutation and compared to the positions of the anode wires which fired. If one possible permutation has the largest number of matchings within $\pm 1.5^\circ$, it is selected as the correct matching. If more than one permutation has the maximum number of matchings, the integrated ADC values on each plane are compared peak by peak to choose among the permutations. At the end of this procedure the hits on the two chambers have been paired up. Some of these pairs will have more than one crossing between the associated cathode strips. In the cases where an anode wire matched up with one of the crossings, only that crossing is considered. Otherwise, both crossings are sent to the LTracks routines.

LTracks is the package which takes the hit locations on each of the three chambers and constructs tracks and vertices from them. This is the first point where plastic information is considered in the chamber reconstruction. The first step is the association between particles detected in the cylinder and hits in the outer chamber. Since they are so close to each other, relatively tight tolerances can be used to determine matchings. Hits on the outer chamber which are within $\pm 11^\circ$ in ϕ and ± 30 cm in z with a hit in the CD's are considered. If there is only one possible match for a plastic hit and an MWPC hit, these are assigned and the process repeated until all clear matchings are assigned. In the cases where there are still multiple possibilities, preference is given to those MWPC hits that have an associated anode wire. Finally, in the very few remaining cases with multiple possibilities, assignments are made arbitrarily.

Next, outer MWPC hits are assigned to plastic hits that did not fire a CD. Not many assignments are made in this section. Those that are include "neutral" particles in the cylinder which may actually be charged particles slipping by the CD's, and charged particles (or neutral particles which knock out a charged particle) in the endcap which reach the outer chamber but do not have enough remaining energy to fire a CD. The process used to make the assignments is similar to that described above.

So far only hits in the outer chamber have been considered. The next step is the association of hits in the inner MWPC with hits in the outer MWPC which have been assigned to a plastic hit. This is done by considering those inner MWPC hits which are within $\pm 14^\circ$ of an outer hit. All cases in which there is only one possibility are assigned and an attempt is made to calculate a vertex. In the cases in which there are two tracks which pass within 1 cm of each other, the vertex taken is the midpoint of the shortest line segment connecting the tracks. In the cases that have only one clear track, the point of its closest approach to the beam is taken as the vertex. Once a vertex is found, it is used to sort out other possible matches as tighter ϕ -tolerances and a z-tolerance can be used in the sorting procedure.

Finally, unassigned inner chamber hits and unassigned plastic hits are matched up by similar methods to those described above. In all cases, if two possible crossings were passed to L_Tracks by L_Recon, as soon as one is assigned the other is discarded.

As described above, an event will have a calculated vertex if at least one charged particle has hits in both the inner and outer chambers. In those cases which have a calculated vertex, all charged particles will have calculated trajectory information whether they have two hits or only one. In the latter case the vertex is used as the second point necessary for calculating θ and ϕ .

Examples of the resolution with which the MWPC's measure the vertex position appear in figures 3-2 and 3-3. The first shows the z-position of a reaction, clearly identifying the objects in the beam. The second shows an x-y projection of a 20 cm slice from the target differentiating the beam spot and the target walls. It is clear that when MWPC information is available, there is no difficulty in selecting events from the target gas.

3.3 Calibration

The energy calibration of the detector was accomplished by using the reaction ${}^2\text{H}(\pi^+, pp)$. It was possible to select events arising from this reaction by the MWPC's (not using any energy

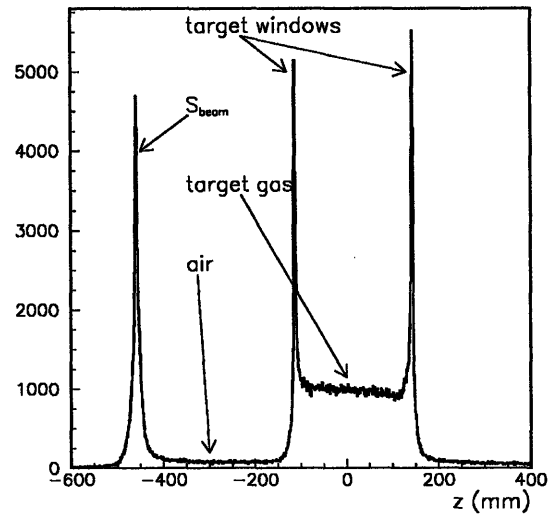


Figure 3-2: MWPC reconstruction of the position along the z-axis at which a reaction occurred.

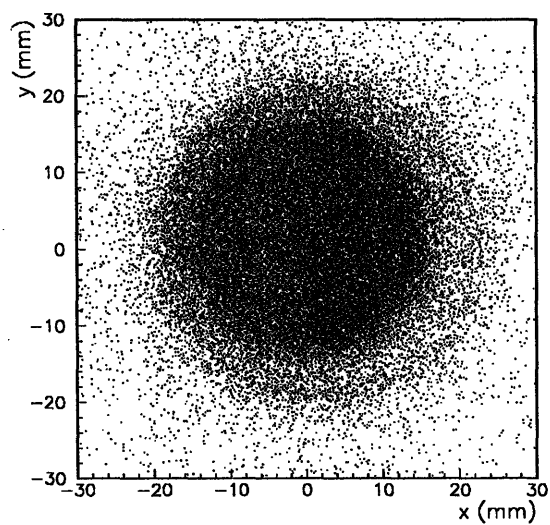


Figure 3-3: MWPC reconstruction of the position in the x-y plane at which a reaction occurred in a 20 cm slice in z around the center of the target.

information from the scintillators) by choosing events from the target region that were back-to-back in the CM system of the reaction. This cut is very clean with negligible backgrounds from π^+p scattering. The angular information alone is enough to calculate the energies of the protons. In order to calibrate the energies, a procedure similar to that used by the Eloss package described in section 3.5 was then used to track the outgoing protons through the various materials in the detector in order to determine the amount of light deposited in each scintillation counter.

The assumption was initially made that the ADC value measured from the PMT's was a linear function of the amount of energy a charged particle deposited in a counter, with the exception of known non-linearities arising from saturation effects in the scintillators (also described in section 3.5). Since a particle which deposits zero energy will not get a detector response, this assumption means that only a scale factor has to be determined for the i^{th} sector:

$$E_i = a_i L_i,$$

where L_i is the amount of light detected. In the case of the cylinder, attenuation was handled by using the geometric mean of the light detected by the PMT's on each end. However, it was desirable to calibrate each PMT separately, so the MWPC's were used to determine where each particle hit the cylinder sector. Comparisons of hits at many different z -positions allowed the calculation of the attenuation length for each sector, which was then used to calculate a scale factor for each phototube individually.

The above method was suitable for obtaining energy calibrations with a FWHM of about 6% for an absorption event. This is well above the 2.5% obtained when testing the cylinder E-block setup with beams of mono-energetic protons. Most of the difference is attributable to non-linearities in the system. Some examples from among a myriad of possibilities are a non-linear response of the $\times 10$ Fast Amplifiers or the ADC's, or a dependence of the energy calibration on the z -position at which the proton hits the E-block due to different paths the light takes to the PMT's. To account for some of these effects, a package called "Fine-Calibration" was developed. This package uses the fact that it is possible to identify protons from the reaction ${}^3\text{He}(\pi^+, \text{ppp})$ and determine their energies using only trajectory information from the MWPC's. This reaction provides a source of protons with widely varying known energies at all angles. Calibration correction curves were determined by fitting the resulting spectra in terms of both energy and angle independently. As it was determined that most of the non-linearities were due to energy variations, typically only that correction function was used. With it in place, calibrations with a FWHM of 4% were typical.

The timing calibration required several steps. First, the gain of the TDC's was determined by looking at LED pulses and inserting successively longer lengths of delay cable. The TDC's had a typical calibration factor of 0.099 ns/channel. After the gain was determined, high energy π^+ 's from scattering were used to determine the offsets. These particles were chosen because their fast flight-times were accurately calculable from their energies.

The above method was used to calibrate events for a particular run. To account for shifts in the position of the incident pions in the RF timing envelope, the TDC value for S_{time} was used to adjust the calibration on an event-by-event basis. Shifts in the timing calibration over time tended to affect all the counters simultaneously. One example of a possible effect would be variations in the length of the 100 ns cables which carry the signals to the electronics shack due to temperature changes. To account for such variations, the timing calibration was normalized to the position of the timing peak in the S_{beam} spectra for each run.

3.4 Particle Identification

A variety of particle identification (PID) techniques were used with LADS. Some of these have been previously mentioned, such as using MWPC information to identify specific final states of particular reactions. The main package, however, depended on two techniques: E-dE/dx and E-TOF.

E-dE/dx makes use of the fact that a charged particle traversing a thick piece of scintillator (defined as one in which it stops) will typically deposit all of its kinetic energy, while a particle traversing a thin piece of scintillator (defined as one in which it loses only a small fraction of its energy) will typically deposit an amount of energy approximately proportional to the square of the ratio of its charge and its velocity. Since the kinetic energy is a function of mass and velocity, it is possible to use the above two quantities to determine the particle's mass in terms of its charge, usually unambiguously identifying the particle.

An example of an E-dE/dx plot is shown in figure 3-4. The total detected kinetic energy of the particle is graphed on the x-axis, and the amount of energy deposited in the dE counter, divided by the length of the particle's track through the dE, is graphed on the y-axis. The particles fall in clearly differentiated bands corresponding to the particle type. Also shown in the figure are the cuts applied to the data to determine the particle type, indicated by hyperbolic lines. The background of events above the particle bands corresponds to particles

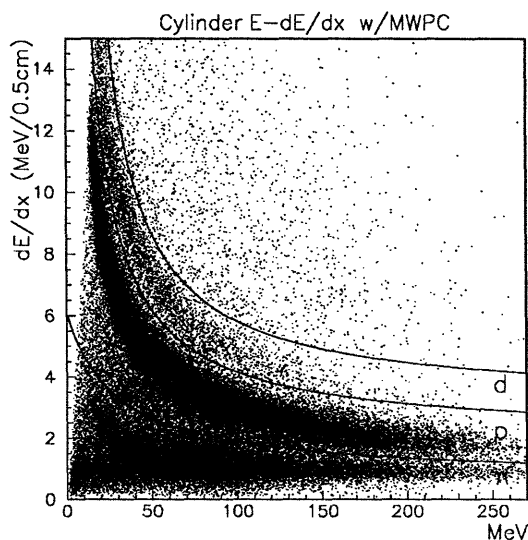


Figure 3-4: An E-dE/dx plot for cylinder particles with MWPC trajectory information. The data are from 239 MeV π^+ incident on N. The curves show the tests used for PID.

which deposited more than the normal amount of energy in the dE, possibly because they reacted in the dE or in the E-block (causing charged particles to recoil back through the dE counter). This method only works when the particle deposits a significant amount of energy in an E-block, so it is only applied to particles with >10 MeV deposited in the E-blocks.

The previous figure shows E-dE/dx as calculated by the cylinder for particles which have MWPC trajectory information. Other possibilities include cases which do not have MWPC information (the trajectory calculated from the plastic information, assuming that the vertex was at the center of the target) and cases in which the dE-dx is calculated from the endcap's dE's (ED's). These other possibilities are shown in figure 3-5. The resolution of the different particle types is worse without MWPC information than with such information, but the vast majority of the particles are still clearly identified. In the figures showing E-dE/dx in the endcaps, a tail moving off from the main proton band in the direction of lower energies is clearly visible. These tails, which also exist in the cylinder but are harder to see, correspond to relatively low energy protons whose kinetic energy is not all converted to light in the scintillator. Thus they are more energetic than the amount of light collected indicates, and have a correspondingly lower dE/dx than would be expected from the detected total light. One possible explanation for this effect is that the particle undergoes a nuclear interaction in the scintillator, and some of

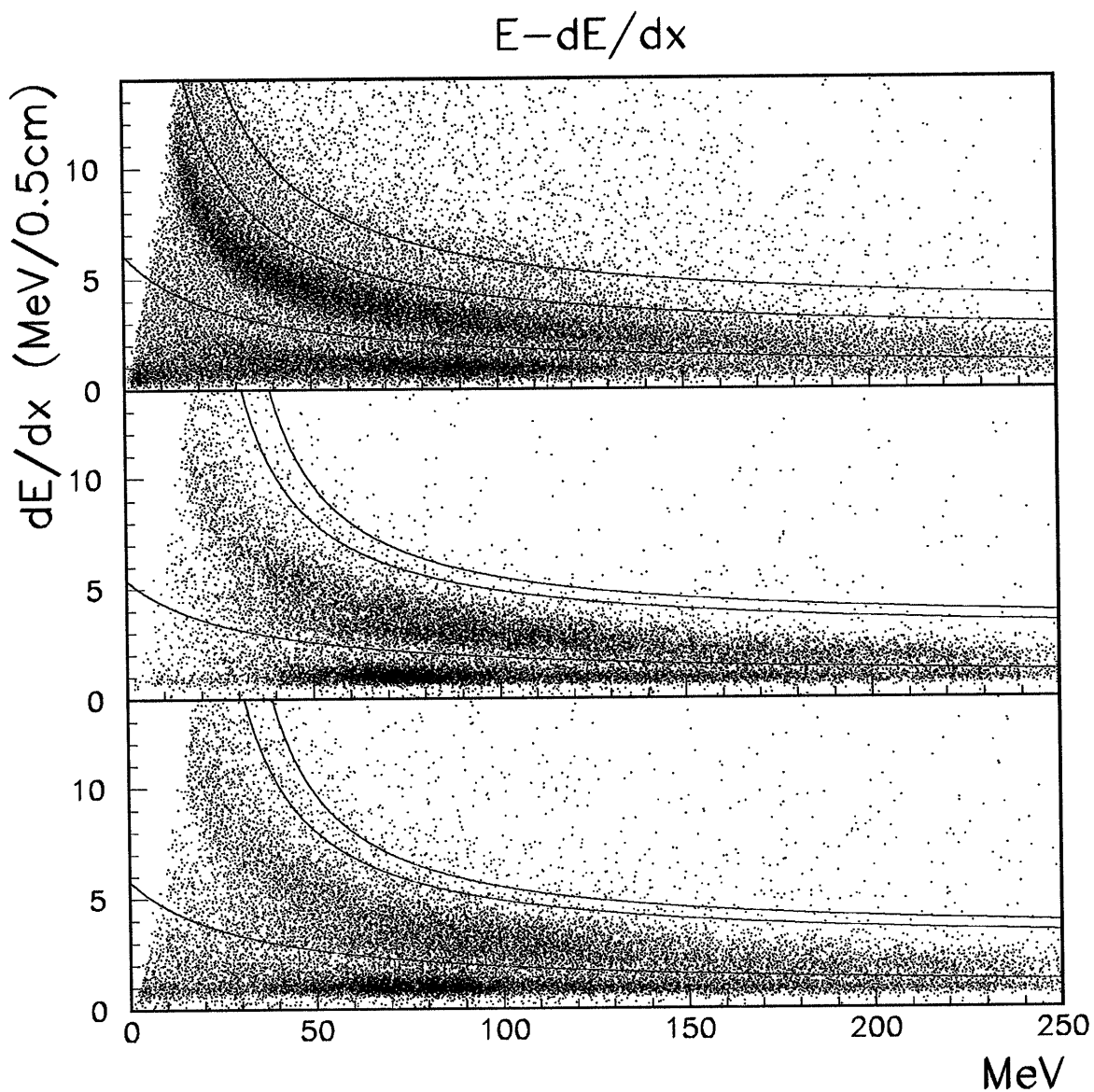


Figure 3-5: $E-dE/dx$ plots following the interaction of 239 MeV π^+ 's with N. The top figure shows the calculation for the cylinder without using MWPC data, the middle figure is for the endcaps with MWPC data, and the bottom figure is for the endcaps without MWPC information.

its kinetic energy is not converted into light, being carried off by neutral particles or being used to break up a nucleus. Another possibility, dominant in the endcaps, is that the proton has enough energy to punch through the endcap, but loses a lot of energy in the ED's light guide. The PID curves are very loose in this region, so the particles are usually correctly identified. Still, these two effects need to be corrected for in the analysis, as will be explained in following chapters.

The other main PID technique used is similar to $E-dE/dx$, but uses the reduced time-of-flight (TOF) instead of dE/dx . The reduced TOF is the amount of time it takes the particle to traverse 30 cm, and it corresponds to $1/\beta$. This is trivially a function of velocity and, when it is graphed versus the total energy, bands appear corresponding to different particle masses. Figure 3-6 shows the E-TOF graphs for four distinct cases. Clockwise from the upper left corner they are: cylinder w/MWPC; cylinder w/o MWPC; endcap w/o MWPC; and endcap w/MWPC info. The bands and features are similar to those seen in the $E-dE/dx$ figures.

The main LADS PID machinery works by a strict hierarchy. If a charged particle deposits more than 10 MeV in an E-block, $E-dE/dx$ is used. In these cases, the cylinder is used if it is available because the resolution of the CD's is better than of the ED's. If the particle deposits less than 10 MeV in an E-block, E-TOF is used. The ED's then have priority over the CD's since in the calculation of the reduced TOF it is important that the particle has not lost a significant amount of energy. As will be seen in Chapter 4, this PID machinery forms the basis of this analysis's PID, but it is modified to improve identification in possibly ambiguous cases.

3.5 Energy Loss

The final major section of the physics package consists of the energy loss routines, or *eloss* for short. The amount of light detected in the scintillator is related to the particle's kinetic energy at the event vertex, but it is not equal to it. There are two major effects which need to be accounted for. The first is saturation in the scintillator, and the second is energy loss in the intervening materials.

Saturation is a term referring to the fact that a scintillator's light output is not a linear function of the converted kinetic energy. As described in section 2.3, a charged particle passing through a scintillator ionizes the material, and the resulting electron-holes are then filled from the electron sea. It is the de-excitation of the sea electrons which determines the light output.

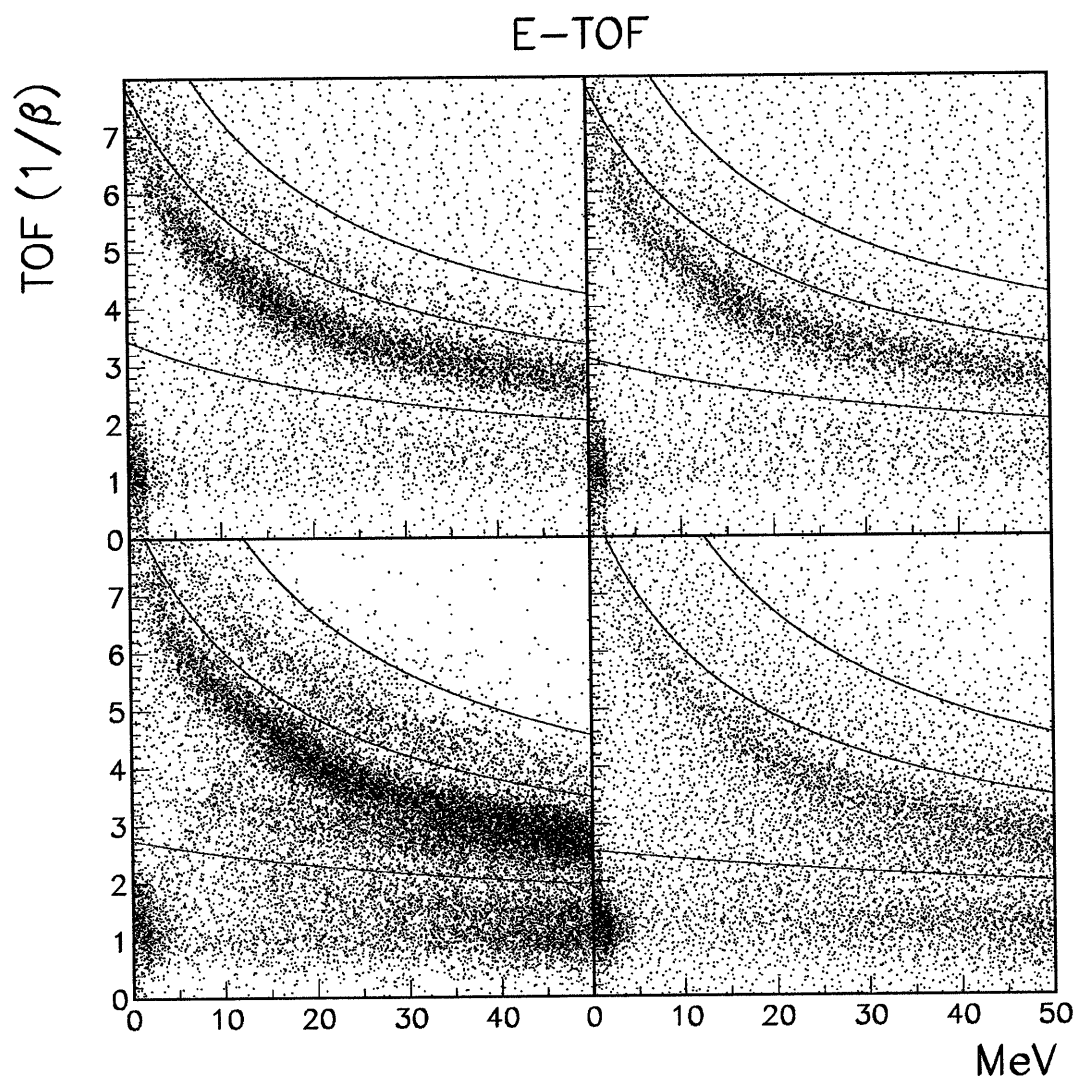


Figure 3-6: E-TOF plots following the interaction of 239 MeV π^+ 's with N. The top left figure shows the calculation for the cylinder using MWPC information, the top right is for the cylinder without using the MWPC's, the lower left figure is for the endcaps with MWPC data, and the lower right figure is for the endcaps without MWPC information. The hyperbolic lines show the cuts used to separate pions, protons, and deuterons.

Any additional energy carried off by the excited electron over the ionization potential will not affect the resulting signal. As the particle loses energy in the scintillator, it moves more slowly and spends more time in the immediate vicinity of each electron, and more energy is typically transferred. The light output is therefore less than would be expected for the amount of deposited energy, and the scintillator is said to be “saturated”. Saturation is only a small effect until the last ≈ 10 MeV of the particle’s energy. It is a well known effect, and formulae to adjust for it appear in the literature [89].

Energy loss refers to the fact that the particle ionizes all of the material it traverses, not just the scintillator. The energy deposited in the other materials is not detected, and needs to be corrected for. Many electrons are typically ionized by the particle, and the rate of energy loss can be described statistically by the Bethe-Block equation:

$$-\frac{dE}{dx} = 2\pi N_A r_e^2 m_e c^2 \rho \frac{Zz^2}{A\beta^2} \left[\ln\left(\frac{2m_e \gamma^2 v^2 W_{\max}}{I^2}\right) - 2\beta^2 \right]$$

For definitions of all the terms, see reference [90]. The distribution has the feature that above a certain energy, charged particles lose approximately $2 \text{ MeV}/(\text{g}/\text{cm}^2)$. This rate of energy loss is known as minimum ionizing, and occurs above about 30 MeV for pions and 300 MeV for protons. It has the additional feature that on a log-log plot the function for range in terms of initial energy is linear to a good approximation, allowing for simple parameterization. The particle’s energy can then be corrected for each material it passes through. Table 3.1 shows the thicknesses of the various materials encountered.

The method followed for correcting the energy for the effects of eloss and saturation includes these steps:

- 1) Sum all the light deposited in the cylinder, if any. Correct for saturation effects.
- 2) Correct for eloss in the outer MWPC and the ED light guide, if necessary.
- 3) Sum all the light deposited in the endcaps, if any. Correct for saturation. If there was light deposited in both the cylinder and endcaps (punchthrough) this is done by starting with the energy the particle has after leaving the endcap scintillator, using the inverse of the saturation formula to convert this into an equivalent amount of light, adding the actual endcap light, and finally using the saturation formula to convert this into an energy.
- 4) Correct for eloss in the air, inner MWPC, target walls, and target gas.

Material in LADS			
Description	Composition (Density g/cm ³)	Thickness mg/cm ²	Notes
Target Gas	³ He (example), 95.0 bar at 32.0° C (10.83)	21.65	Thickness varies with vertex
Target			
Lining	Ag 10 μm	10.5	
Lining	Cu 20 μm	17.9	
Walls	C fiber, 3 layers, (1.784)	64.2	Total, for all 3 layers
Walls	epoxy, 3 layers, (1.5)	19.4	Total, for all 3 layers
Reinforced Regions	C fiber ≈ 0.7 mm thick	125	Most particles
Reinforced Regions	Epoxy ≈ 0.3 mm thick	45	not affected
Air elevation 360 m	≈ 1017.5 hPa, 30.5° C (.00113)	28.4	Total air for cylinder particles
Inner MWPC			
Two grounding foils	Kapton, 25 μm (1.42)	7.1	
Two support cylinders	Rohacell C ₉ O ₂ NH ₁₃ (.050)	20	Each 2 mm thick
Two cathode foils	Kapton ≈ 45 μm (1.42)	12.8	50 μm before scratching
Al Coating on Kapton	8 layers Al, 700 Å each	1.5	
Epoxy	Araldit, 4 layers	5	
MWPC Gas	Ar and C ₂ H ₆	1	
Two epoxy beads	Araldit, ≈ 2 mm × 2 mm (1.5)		Most particles not affected
ED Wrapping			
Al foil	Al 12 μm thick (2.7)	3.24	
Al Mylar	Mylar 25 μm thick	3.5	Ignore Al coating
Outer MWPC			
Two grounding foils	Kapton, 50 μm (1.42)	14.2	
Two support cylinders	Rohacell C ₉ O ₂ NH ₁₃ (.050)	30	Each 3 mm thick
Two cathode foils	Kapton ≈ 45 μm (1.42)	12.8	50 μm before scratching
Al Coating on Kapton	8 layers Al, 700 Å each	1.5	
Epoxy	Araldit, 4 layers	5	
MWPC Gas	Ar and C ₂ H ₆	1.6	
Four epoxy beads	Araldit, ≈ 3 mm × 3 mm (1.5)		Most particles not affected
CD Wrapping			
Al foil	Al 12 μm thick (2.7)	3.24	
Mylar support	Al Mylar, 20μm	.9	Partial coverage

Table 3.1: All thicknesses are given for a trajectory normal to the beam line. Adapted from reference [20].

The loss corrections are significantly more accurate when MWPC information is available to allow accurate determination of the material traversed. For this reason, among others, results in this thesis which depend on accurate energy reconstruction are limited to those particles which have MWPC information.

Chapter 4

Particle Multiplicities

There are several possible reactions between a pion and a nucleus. In the energy region of the Δ -resonance the dominant possibilities are: elastic scattering, inelastic scattering, single charge exchange (SCX), double charge exchange, and absorption. It is also possible to have combinations of these interactions; *e.g.*, inelastic scattering followed by single charge exchange. As explained earlier, this experiment is studying π^+ absorption. The distinguishing factor of events including absorption is apparent from the above list. Absorption events have no pions in the final state; non-absorption events have pions in the final state. Thus, absorption events are identified by checking the identity of all final state particles and selecting the events which do not include pions. Unfortunately this process is complicated by the presence of SCX. The final state pion is a π^0 , which decays into two photons. Thus, it is also necessary to identify photons and determine their origin in order to isolate absorption.

The main goal of this analysis is the determination of multiplicities of energetic particles of various types resulting from an absorption reaction. The multiplicities will be presented in the form of cross sections, which are determined using the formula:

$$\sigma_i(\text{mb}) = \frac{N_i}{N_{\text{beam}} \times \rho_{\text{target}} \times L_{\text{target}}} \times 10^{-27}.$$

N_i = the number of detected events satisfying any particular conditions (denoted by i , such as 2CON).

N_{beam} = the number of beam particles incident on the target.

ρ_{target} = the density of the target in terms of nuclei per cubic centimeter.

L_{target} = the length of the target expressed in centimeters.

Determining the cross section thus involves several steps. The most complex of these is the identification of a set of absorption events which occurred in the target. This involves the separation of reactions in the target from those outside, the identification of all final state particles, and the imposition of the particular conditions being used. The determination of the denominator is relatively straightforward, although meticulous attention has to be paid to the magnitudes of occurrences such as pions missing the target.

In the following sections, the steps followed in the analysis will be described in detail.

4.1 Separation of Events Originating in the Target

The first step in this process is to separate those events which have a vertex position calculated by the MWPC's from those events which do not. The reconstruction of trajectories is described in detail in section 3.2. To recap briefly, an event will have a calculated vertex if at least one of the particles in the final state has hits in both the inner and the outer chambers. Each chamber has an efficiency of roughly 95% of correctly reconstructing a hit, so roughly 90% of the charged particles passing through both chambers will have two hits. If two particles each have two hits, the intersection of the tracks is used as the event vertex. If only one charged particle has two hits, the point of its track's closest approach to the beam is used as the vertex.

Consider first events which have an MWPC vertex. The z-position of this vertex is typically accurate to a couple of millimeters, which is small on the scale of the length of the target. It can therefore be accurately used to cut on the center 20 cm of the 25.7 cm target region. However, the beam has a spread in the x-y plane which is larger than the extent of the target, so some events originate in the carbon-fiber of the target walls or outside of the target. The MWPC's could be used to select the interior region, but the available precision is not adequate for this task. Instead, data were taken using an empty target, and a "cross section" was calculated using exactly the same methods as for the full target. The events comprising this cross section were attributed to events occurring outside of the target gas. To correct for this inclusion, this empty background was subtracted from the final measurement.

Unfortunately, the presence of the target gas changes the characteristics of the beam. As the beam passes through the full target, multiple scattering effects cause the profile to widen

more quickly than for the empty target. A greater fraction of the pions pass through the walls and the region outside for the full target, and the empty background subtraction has to be scaled correspondingly. This correction factor has been estimated by zeroing the cross section for three charged particle final states following the absorption of π^+ on ^2H . It is difficult to determine accurately, so a conservative uncertainty was chosen. The value used is $f_e = 1.2 \pm 0.1$.

Now consider the events which have no MWPC calculated vertex. In the regions of phase space where a charged particle passes through both chambers, the lack of a vertex is attributable to the efficiency of the chambers. It is possible to determine this efficiency accurately, and these events could be corrected for by weighting the number of detected events that did have a vertex by a compensating factor. However, this is not possible to do for the regions of phase space that do not have any charged particles passing through both chambers. To handle these events, one of two possible methods must be followed. The first is to attempt to extrapolate over the unmeasured regions. This could be done by constructing a model for the interactions involved and using simulations to determine what fraction of the events are undetected. This method is attractive because it allows for extrapolations over the energy regions below the detector threshold. However, it is unattractive because the various interactions involved are not well understood, especially in the heavier nuclei. Alternatively, some functional form could be chosen (for example, low order Legendre polynomials) and fit to the differential spectra. Then this function could be used to correct the detected cross sections. This method involves the assumption that the unobserved regions can be accurately extrapolated over by the chosen functions.

The second main possibility would be to use the data that do not have MWPC calculated vertices. A cross section is calculated for the data that do not have a vertices assuming that the interaction occurred in the target, using its entire 25.7 cm length. The same process is applied to the empty target, and the difference taken. The assumption made in this analysis method is that the MWPC efficiency is the same for the empty and full targets, which has been confirmed. The main benefit of this method is that it does not require any guesswork about the nature of the absorption reaction. A secondary benefit is that it is unnecessary to correct the results to account for any MWPC inefficiencies, since any events for which the MWPC fails to fire will be included in the no-MWPC subset of events. The main disadvantage of this method is that the signal-to-background ratio is high for the events without an MWPC vertex, since only one-half of the material in the beam is the target gas. This leads to large statistical errors for this component of the cross section. Fortunately, this part of the cross section is a small fraction of the total, and the errors introduced are acceptable.

The data without MWPC vertices was in fact used in the analysis because of the advantages mentioned above. Comparisons were made when reasonable to extrapolations from the MWPC data to ensure no major discrepancies arose. In summary, the reactions which occurred within the target region were isolated through a combination of using the vertex information provided by the MWPC and subtracting off background measurements obtained from empty target runs. For the events which had a calculated vertex, a 20 cm slice from the center of the target was used. For those events which did not have a vertex, the entire 25.7 cm length of the high pressure gas was used.

The empty multiplication factor applied to the background subtraction when a vertex was available was not used in the cases which had no vertex ($f_e = 1$). Although the same spreading effect is expected to occur, the amount of the background attributable to reactions in the cylindrical walls of the target is only a small fraction of the total background. A correction factor as a fraction of the final cross section could possibly be estimated from the MWPC data and applied to the after subtraction no-MWPC result. However, this factor would be very uncertain, and as its effect on the total cross section would be small, it was neglected.

Another problem with the no-MWPC data also involved the spreading of the beam due to multiple scattering. It was found in the analysis that many events consisted of only one detected charged particle which was in the inner E-block of the downstream endcap. Most of these particles were beam pions that had scattered, but had not undergone a nuclear interaction in the target. The rate was significantly higher for the full target runs than for the empty target runs, and the subtraction of the empty background was not sufficient to correct the problem. Although most of these pions were correctly identified, the rate was high enough for PID errors to cause a significant problem. For this reason the acceptance of the detector was limited by ignoring events which had no MWPC vertex and consisted only of charged particles with light in the downstream endcap's inner E-block.

4.2 Modifications to the Experimental Definition of a Particle

Now that events originating in the target have been isolated, the next step is to reject those that have charged pions in the final state. Before this is done, several changes were made to the routines which reconstruct particles, described in section 3.1. First, particles which had less than 2.5 MeV of associated light detected in the cylinder were interpreted as noise and were ignored in the analysis. PID was not performed on these particles, and they were not counted in

the multiplicities. For charged particles this restriction increased the effective detector threshold by 2.5 MeV. It was also applied to neutral particles. Second, any particle that had a reduced TOF ($1/\beta$, or the amount of time needed for the particle to traverse 30 cm) of greater than 7 ns was also ignored in the analysis. For a nucleon, this TOF corresponds to an energy of about 10 MeV; for a deuteron, about 20 MeV. This is significantly less than the actual detector threshold for the charged particles, so these are clearly noise. For neutrons, this restriction sets a lower limit on the detector threshold of roughly 10 MeV, above which the detection efficiency will vary with the neutron's energy as discussed in chapter 5.

The final modification is more complex. The CTP routines described in section 3.1 do not handle punchthrough neutrals well. These are neutral particles which react and impart energy to protons in the endcap E-blocks. The protons then enter the cylinder. When there is a charged particle detected in the cylinder region behind an endcap there is clearly a problem, as a particle cannot travel from the target to this region without being detected by the endcaps—either as a charged or neutral. These charged particles were therefore ignored in the analysis if no neutral was detected in the endcap, or combined into a single neutral if one was detected.

4.3 Charged Pion Identification

The main method used here is the standard Ladybird PID machinery described in the last chapter. This machinery, with the cuts shown in section 3.4, correctly identifies over 90% of the charged pions detected. However the resolution effects in the detectors involved allow some pions to slip through. Close examination of the remaining events shows that some simple additional cuts remove most of the remaining charged pions. These consist of an overall E-TOF cut applied to all particles (the PID machinery only uses E-TOF in those cases where E-dE/dx is impractical) and a dE/dx cut on the endcap dE for punchthrough particles. In addition, small gaps between the dE's allowed some charged particles to slip between them, which means that they appear to be neutral particles to the plastics. Many of these "neutral" particles could be correctly reclassified and identified. These additional PID methods are described in the following subsections.

4.3.1 Additional E-TOF Cut

For the majority of the particles detected, the PID method applied by the PID machinery is E-dE/dx. E-TOF is used only for the least energetic particles. It is also possible to use E-TOF for more energetic particles, but the relatively short flight path means the resolution will not be as accurate. However, the optimal method is to primarily use E-dE/dx, but also to use E-TOF to identify cases where the original identification was probably an error. This is done by first applying E-dE/dx to make as clean a separation of π 's and p's as possible, as described in section 3.4. After eliminating those events for which E-dE/dx finds a pion, a much less restrictive cut is applied using E-TOF. This additional cut is called the "too-fast" cut, and it is illustrated in figure 4-1.

In each of the four cases, the tight cut on the proton band is the normal PID curve from figure 3-6. The looser cut is the too-fast cut. It is clear from the figure that there is some pion contamination in the events after the initial PID methods have been applied, which this additional cut helps to minimize. The too-fast cut is looser than the normal PID cut to minimize errors where a proton is identified as a pion, especially at the higher kinetic energies where the timing differences are small.

4.3.2 dE/dx for Punchthrough Particles

Because the resolution for calculating dE/dx is better for the cylinder than for the endcaps, cylinder information was used in the standard PID machinery for punchthrough particles. This generally works very well, but it is possible for a pion to enter an endcap and react in the scintillator, transferring energy to a proton which subsequently enters the cylinder. In this case, the main PID machinery misidentifies a pion as a proton. In a similar manner to the too-fast cut, it is possible to use both methods simultaneously by applying an additional E-dE/dx cut using the endcap dE's to punchthrough particles. This additional cut is shown in figure 4-2. The figure clearly demonstrates that a significant number of punchthrough pions are misidentified as protons by the normal PID machinery in the punchthrough region.

4.3.3 PID for "Neutral" Charged Particles

The majority of the remaining charged pions which have not been correctly identified have slipped through the cracks between the dE's, and thus appear to be neutral particles to the

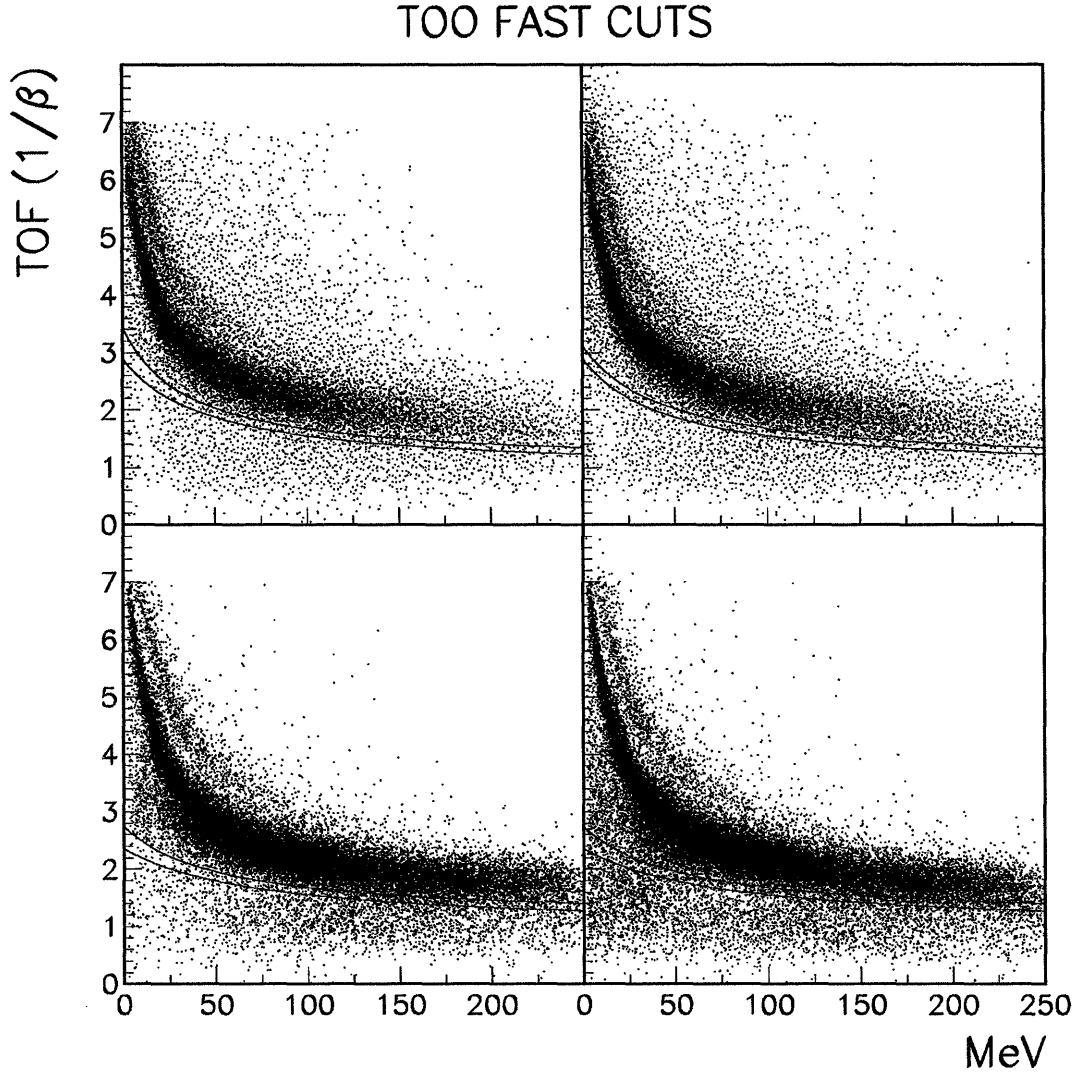


Figure 4-1: The too-fast cut is shown as the lower curve on each figure; the upper is the normal PID cut. The data are from the interaction of 239 MeV π^+ 's with N, with pions identified by the basic PID machinery already removed. The top left figure shows the calculation for the cylinder using MWPC information, the top right is for the cylinder without using the MWPC's, the lower left figure is for the endcaps with MWPC data, and the lower right figure is for the endcaps without MWPC information.

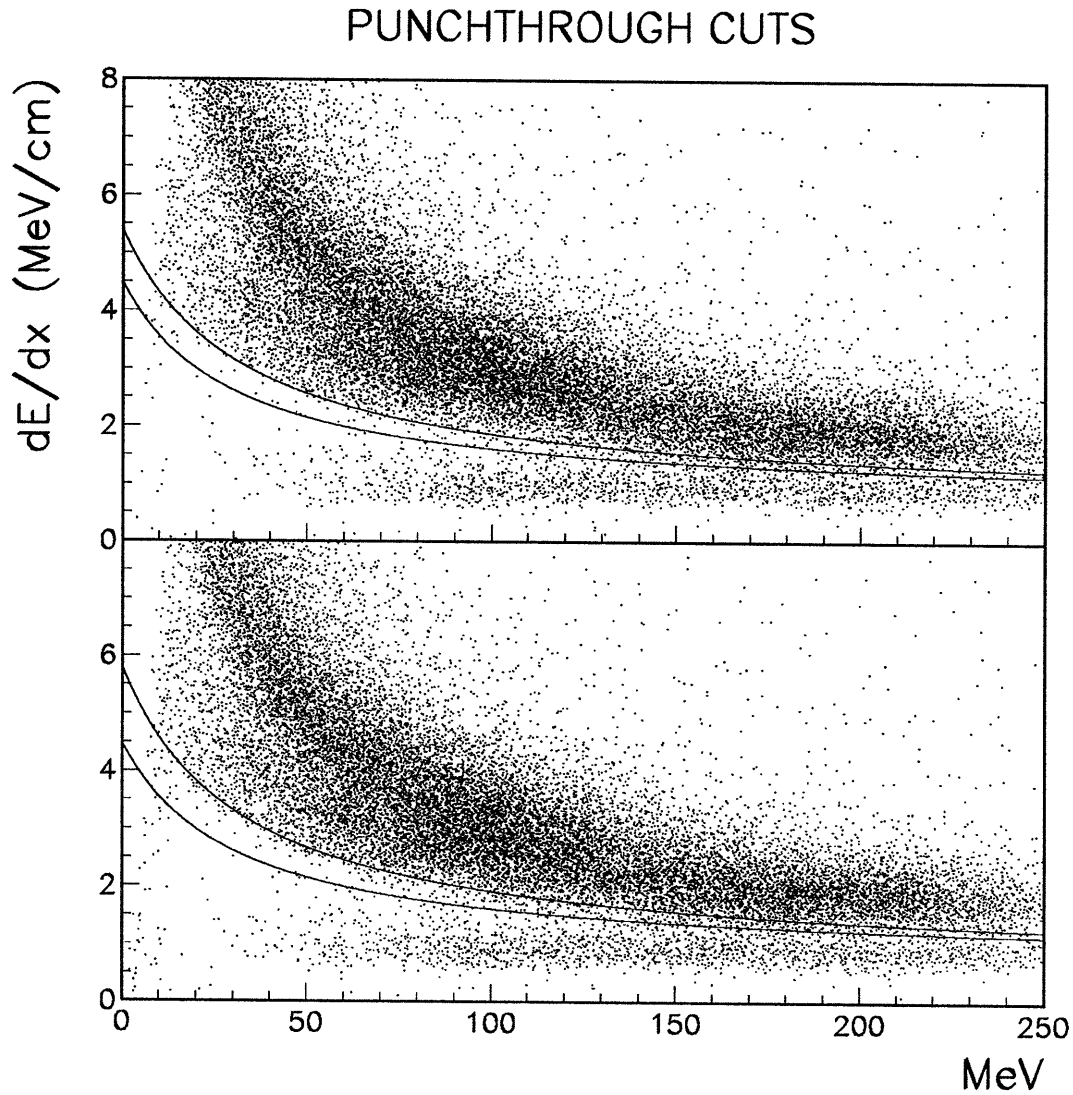


Figure 4-2: The punchthrough cut is shown on each figure as the lower curve; also shown is the normal E-dE/dx cut as the upper curve. The data are from the interaction of 239 MeV π^+ 's with N, with pions identified by the basic PID machinery already removed. The top figure shows E-dE/dx for the endcaps using MWPC information, and the lower is for the endcaps without using the MWPC's.

detector. These particles were identified by determining whether there was MWPC information for the particle. If a neutral particle in the cylinder had an outer MWPC hit, or an endcap neutral had an inner MWPC hit, then that particle was reclassified as a charged particle. It is of course impossible to use $E-dE/dx$ for these particles; however, E-TOF is still available. Thus, the standard PID machinery's E-TOF PID (see figure 4-1) was applied to these particles in order to veto events including charged pions, and to correctly count the number of protons.

Unfortunately, this additional fix did not prove sufficient to solve the problem, especially for the case of ${}^3\text{He}$ where the absorption cross section is a small fraction of the scattering cross section. The selected no-pion events were found to have contamination from charged pions slipping through the cracks. This contamination appeared as either one charged particle and one neutron, or one charged particle and one gamma. The charged particle was the scattered proton, and it typically had under 50 MeV of energy, or 35 MeV of light. It proved impossible to identify these events cleanly, which had a serious effect on the 1C cross sections. This problem was solved by making a small restriction to the acceptance of the detector. For the case that only one charged particle was detected (along with any number of neutrals), that particle was required to have over 35 MeV of light. Light was used instead of energy in order to ensure that particles with MWPC information and without MWPC information were handled the same. For a proton, 35 MeV of light corresponds to 50 MeV of energy. This restriction has greatly reduced the problems arising from contamination.

This restriction should not significantly affect the absorption cross section, since there are usually two charged particles in the final state. When there is only one, it will usually have over 50 MeV kinetic energy. For example, following the absorption of a 118 MeV π^+ by an nn pair at rest, the smallest amount of energy the resulting proton can have is over 75 MeV. This value will actually be lower since the nn pair is inside a nucleus where both binding energy and Fermi momentum play a role. Thus the cut might have some effects, but they should be small.

4.4 SCX Subtraction

At this point almost all the events with charged pions in the final state have been identified and vetoed. Still contaminating the remaining events are those in which a single charge exchange reaction occurred, leading to a π^0 in the final state. These events need to be identified and their contribution to the cross section subtracted. There are two major methods that can be used. The first is to use the results of other measurements of SCX and various theoretical models

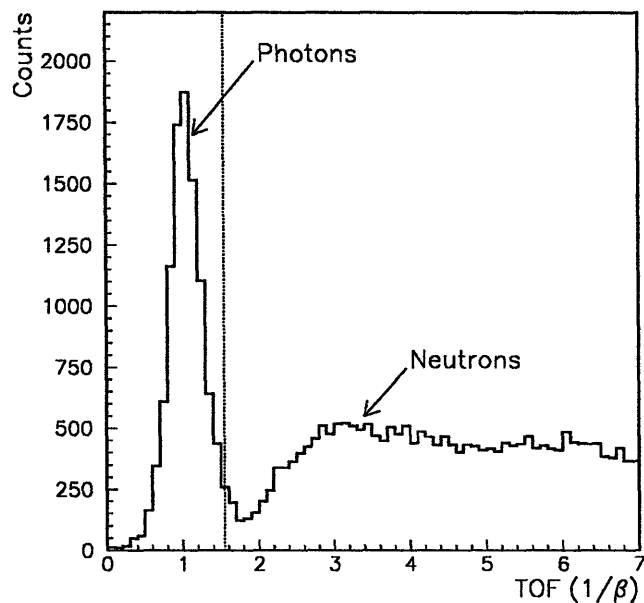


Figure 4-3: The reduced TOF spectrum for neutrals detected after the interaction of 162 MeV π^+ 's with Ar. The cut used to separate γ 's from neutrons is shown as a dotted line.

and extrapolations. However, the accuracy of measurements of SCX on the light nuclei is poor, particularly regarding the fraction of SCX with a certain number of particles above an arbitrary threshold. For this reason, this analysis will use another method: taking results directly from the data to perform the SCX subtraction.

This is possible because the detector has a substantial photon detection efficiency, and because the π^0 's essentially always decay into two energetic photons. The procedure followed involves breaking the data up into those events which have a detected photon arising from SCX, and those that do not. Some fraction of the latter events will still be due to single charge exchange, but they should have differential distributions similar to those with a detected photon, since to first order the detection of a photon is uncorrelated with the kinematic properties of the massive particles. The cross section arising from events with a detected photon can thus be multiplied by an appropriate scale factor, and the result subtracted from the cross sections arising from events with no detected photons. More details follow.

Photons were identified by examining the reduced TOF of the neutral particles detected in LADS. The cylinder inner and outer E-blocks and the endcap outer E-blocks were used for this purpose. The endcap inner E-blocks were neglected because of the difficulties in accurately calibrating them. Figure 4-3 shows a typical spectrum for neutrals detected in the cylinder inner E-blocks. The γ peak is seen to be clearly separated from the neutrons, with the indicated cut leading to an almost clean separation. Now that the photons have been identified, the question of whether they originated from SCX is still open. The other prolific source of γ 's following a reaction in the target region is evaporation. The residual nucleus can be left in an excited state, which typically decays to about 10 MeV by particle emission, and then to its ground state by γ emission. The photons resulting from evaporation are thus generally less than 10 MeV. In contrast, the two γ 's resulting from SCX need to carry the total energy of the π^0 , and are thus usually over 70 MeV. When a photon is detected in scintillator, it has typically produced an electron-positron pair, leading to an electron shower. It depends on the location in the scintillator that the photon converts, but generally a fair fraction of the photon's energy will be detected as light in the scintillator. This allows the separation of γ 's resulting from SCX from γ 's resulting from evaporation by imposing a cut on the detected light. Figure 4-4 shows the energy spectrum of photons detected in the cylinder inner E-block, along with the 14 MeV cut used. From this point on, references to γ 's or photons in this thesis will refer to those which have greater than 14 MeV detected light, and thus are attributed to SCX.

The first step is to determine the γ detection efficiency for the LADS detector. It is in this calculation that the most crucial assumption of this method of subtracting SCX is made: that the probability of detecting each of the two photons is independent. This assumption is not strictly correct, since the directions and energies of the photons are kinematically linked. For example, if one of the two photons is not detected because it goes down the beam pipe, the chances that the other one also goes down the beam pipe is significantly smaller than it would be if the probabilities were independent. However, since LADS covers such a large fraction of 4π steradians, the method is sufficiently accurate.

Having made the above assumption, it becomes possible to determine the γ detection efficiency. Cross sections are separately calculated for the cases in which one photon is detected and the cases in which two photons are detected. In both cases the empty target backgrounds have been subtracted, and the reaction corrections described in section 4.5 have been applied. The cross sections should be related to the total SCX cross section (actually the fraction of the total SCX cross section satisfying the constraint that at least one charged particle be detected) by the formulae:

$$\sigma_{1\gamma} = 2\epsilon_{\gamma}(1 - \epsilon_{\gamma}) \times \sigma_{\text{SCX}},$$

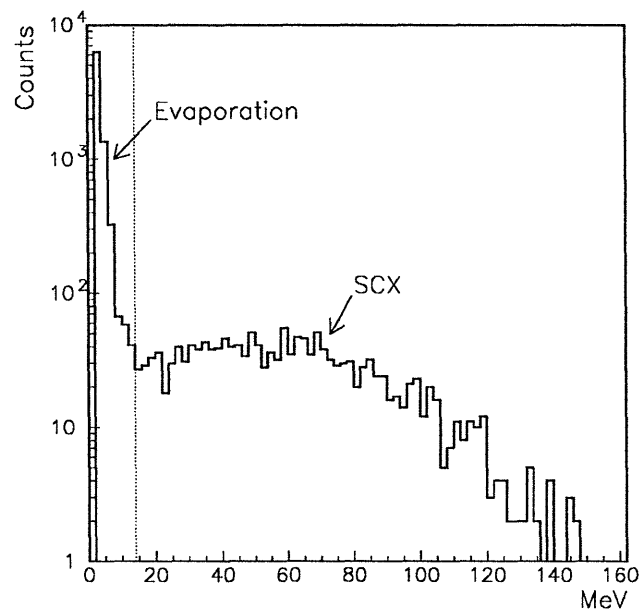


Figure 4-4: The spectrum of detected light for photons after the interaction of 162 MeV π^+ 's with Ar. The cut used to separate evaporation γ 's from SCX γ 's is shown as a dotted line.

$$\sigma_{2\gamma} = \epsilon_{\gamma}^2 \times \sigma_{\text{SCX}},$$

in which ϵ_{γ} is the detection efficiency. Combining these gives:

$$\epsilon_{\gamma} = \frac{2}{2 + \frac{\sigma_{1\gamma}}{\sigma_{2\gamma}}}.$$

The detection efficiency was measured using the above method in two ways. First, it was measured separately for each combination of target and energy from the data itself. The cross sections for detecting one photon and for detecting two photons were measured, and then the above formulae were applied. The detection efficiency depends on the incident pion energy, since the cross section for conversion is a function of the photon's energy. However, the efficiency does not have a clear dependence on A. This is expected, since the π^0 's energy should only have second order dependencies on A. Thus the results were averaged over the four target types. The obtained values were 27%, 27% and 29% at 118, 162, and 239 MeV, respectively.

Second, it is possible to select sets of events in which SCX occurred on ^2H (or ^3He) and two (or three) protons were detected. These events were isolated by cutting on the reconstructed π^0 mass. The γ detection efficiency was then calculated by comparing the number of times photons are detected to the number of selected events. Unfortunately, the cross section for this process is small. At 162 and 239 MeV, it was possible to determine ϵ_{γ} , and the results agreed with those given above. At 118 MeV, this method proved unproductive.

Once the detection efficiency has been obtained, it is used by measuring separately the cross sections with no detected γ 's and with at least one detected γ for a quantity of interest (an example would be the absorption cross section leading to one detected proton and one detected neutron, σ_{1p1n}). Then the final cross section is determined from:

$$\sigma_{1p1n} = \sigma_{1p1n}^{0\gamma} - f_{\text{SCX}} \times \sigma_{1p1n}^{\geq 1\gamma}.$$

Where,

$$f_{\text{SCX}} = \frac{(1 - \epsilon_{\gamma})^2}{2\epsilon_{\gamma}(1 - \epsilon_{\gamma}) + \epsilon_{\gamma}^2}.$$

The detection efficiencies given above correspond to f_{SCX} 's of 1.14, 1.14, and 1.02.

The magnitudes of the SCX corrections are given in table 4.1. The reported cross sections are $(1 + f_{\text{SCX}}) \times \sigma^{\geq 1\gamma}$, and thus include the events with no detected photons. Comparisons

with previously published data are essentially impossible because of the restrictions placed on LADS's acceptance. The requirement that if only one charged particle is detected it must have over 35 MeV of associated light significantly reduces the size of these corrections.

The uncertainties associated with this correction required careful handling because of the correlations between $\sigma^{\geq 1\gamma}$ and f_{SCX} . The importance of this effect is diminished by the fact that an average over the four targets was used to determine ϵ_γ , but it still needs to be considered. The variations of the calculated efficiencies with the target type were consistent with an uncertainty in the measured ϵ_γ of 2%. This value was doubled to account for the effects of correlations, and 4% was used. This value corresponds to an uncertainty in f_{SCX} of ± 0.25 .

This error analysis has proven insufficient. The correction for SCX contamination was the most difficult part of this analysis. During the early stages, negative cross sections for the 1C channel were consistently obtained, with magnitudes that were larger than the expected uncertainties in the calculations. Errors in the SCX correction were the only reasonable source of these problems, and thus the correction was closely examined.

Figure 4-5 is instructive. It shows the energy of a charged particle for the cases in which only one charged particle is detected. This figure will be revisited and more fully explained in section 6.3. SCX corrections have been made using the f_{SCX} calculated above, and result in problems. The negative cross sections at low energies for the ^3He 239 MeV data and the peak in the Ar 162 MeV data are the clearest examples. f_{SCX} was also calculated by adjusting its value until "reasonable" behavior was obtained in these figures. That means that the spectra were consistent with zero (taking the expected pion contamination into account) for ^3He , and dropped smoothly to zero from its value at about 100 MeV for the heavier nuclei. The values for f_{SCX} obtained by this method varied from 0.5 to 2.0. The median value was consistent with that obtained above, but the variation was inconsistent with the uncertainty obtained above.

"Reasonable" behavior is not well defined, however, so these calculated correction factors were not used. The restriction that if only one charged particle is detected, it has more than 35 MeV of light was applied, which greatly reduced the magnitude of the problem. In addition, the uncertainty associated with f_{SCX} was increased from 25% to 50% to obtain better agreement with the variation in measured values. This corresponds to an uncertainty in the gamma detection efficiency of 8%.

SCX			
	118 MeV	162 MeV	239 MeV
^3He			
1C	1.7	6.1	5.4
2C	1.1	3.0	3.6
3C	0.1	0.2	0.5
Total	2.8	9.2	9.4
^4He			
1C	2.6	7.3	10.7
2C	0.6	2.2	4.3
3C	0.0	0.1	0.5
Total	3.2	9.6	15.5
N			
1C	5.4	15.0	20.2
2C	1.4	4.0	9.7
3C	0.1	0.2	0.9
4C	0.0	0.0	0.0
Total	6.8	19.1	30.7
Ar			
1C	11.8	30.3	39.8
2C	2.1	6.7	15.4
3C	0.1	0.3	1.2
4C	0.0	0.0	0.1
Total	14.0	37.3	56.5

Table 4.1: The magnitudes of the total detected SCX cross sections (mb) are given, broken up by the number of charged particles detected. The requirement exists that at least one charged particle be detected in LADS, with the restrictions on the acceptance described in the text.

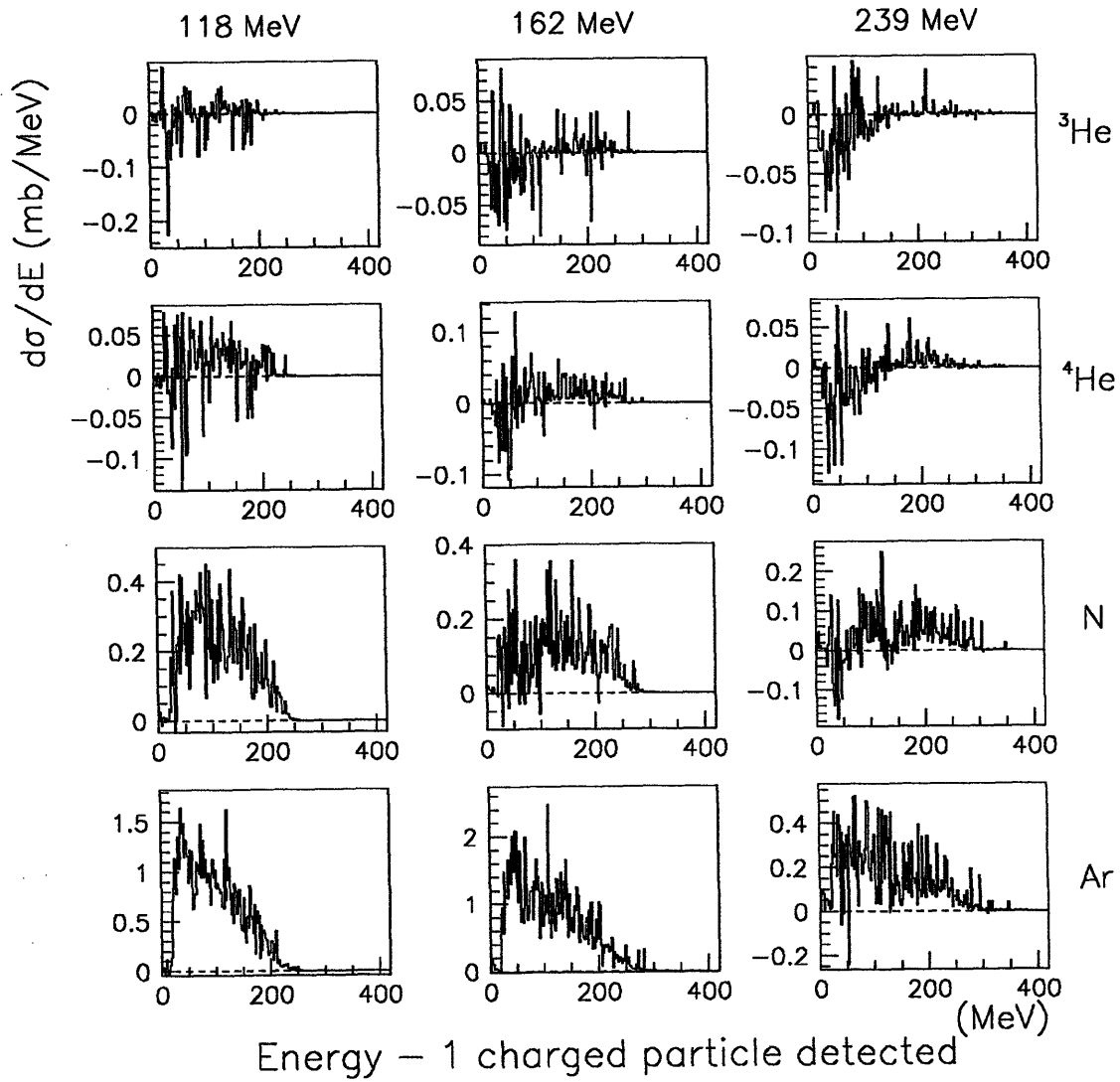


Figure 4-5: The kinetic energy of a charged particle when only one charged particle was detected.

4.5 Reaction Corrections

The majority of charged particles resulting from absorption are protons, and the two errors which affect whether an event is seen as arising from absorption are mistakenly labelling a proton as a pion or mistakenly labelling a pion as a proton. This section will investigate the magnitude of the probability of mistakenly identifying a proton as a pion, and the next section will examine the magnitude of the probability of mistakenly identifying a pion as a proton.

The situation in which a proton is mistakenly identified as a pion is frequently due to reactions. The term “reaction” used in this context usually refers to a charged particle undergoing a nuclear interaction with a component of the scintillator such that not all of the kinetic energy of the particle is seen as light. The definition of a “reaction” used in this thesis is somewhat different. A “reaction” is deemed to have occurred any time a charged particle is labelled by PID as something which it is not. Various resolution effects are thus included with the nuclear processes which determine the nomenclature.

The procedure followed is to first measure the probability of mistakenly identifying a proton as a pion as a function of the proton’s kinetic energy. Then each and every event is weighted by a factor:

$$f_{\text{event}} = \prod_{i=\text{proton}} \epsilon_{\text{react}}(E_i),$$

$$\epsilon_{\text{react}}(E_i) = \frac{1}{1 - p_{\text{react}}(E_i)},$$

where, p_{react} is the probability of mistakenly identifying a proton as a pion, and ϵ_{react} is the resulting correction factor. Two major assumptions are made in the calculation of this correction. The first is that charged particle PID is uncorrelated; that is, the probability of misidentifying one charged particle is independent of whether another charged particle is misidentified. Making this assumption allows reaction corrections to be done on a particle by particle basis. The second assumption made is that the only variable that p_{react} depends on is the proton’s kinetic energy. Clearly, this function should also depend on angle since the geometry of the scintillator varies with θ . In the manner in which the function is calculated, an average is taken over angles which should be similar to the distribution of angles in the data. It is not exactly the same, however, and this is a source of error.

In order to calculate the function $p_{\text{react}}(E_i)$, data are used from the interaction of 239 MeV π^+ ’s with ^3He . A data sample is filtered out in which each event has exactly three charged

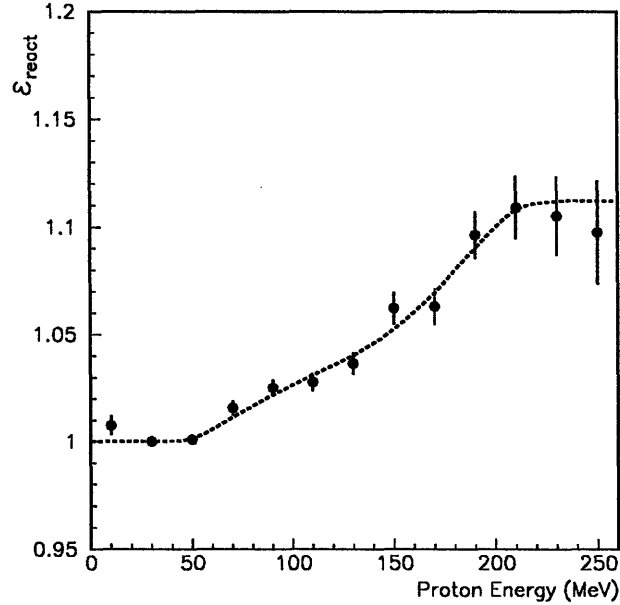


Figure 4-6: The proton reaction correction factor as a function of proton energy for events with MWPC information. The dotted line is the fit used to correct the data.

particles detected by LADS. The three particles are numbered randomly, and the first two are each required to be a proton in the cylinder with two MWPC hits. These two tracks are used to make a clean cut on the target region in both r and z . A missing mass is calculated from these two protons, and cut applied at the proton mass, ensuring that PID is correct for these two particles, an absorption reaction occurred, and that their energy information is correct.

Now the energy of the third proton is calculated from the initial state and the energies of the first two protons. The third proton is subjected to all of the PID tests discussed previously. The function $p_{\text{react}}(E_i)$ is then calculated for 20 MeV bins, and the result fit to a polynomial. The results of the calculations and the fit are shown in figure 4-6. The specifics of the PID methods are slightly different for the cases which do not have MWPC information. In order to obtain the function p_{react} for such events, the same filtered file of events described above is used (selected with the MWPC's). In this case the MWPC's are turned off in the code so that they will not be available for the calculation of the PID of the third proton. The resulting calculations and fit are shown in figure 4-7.

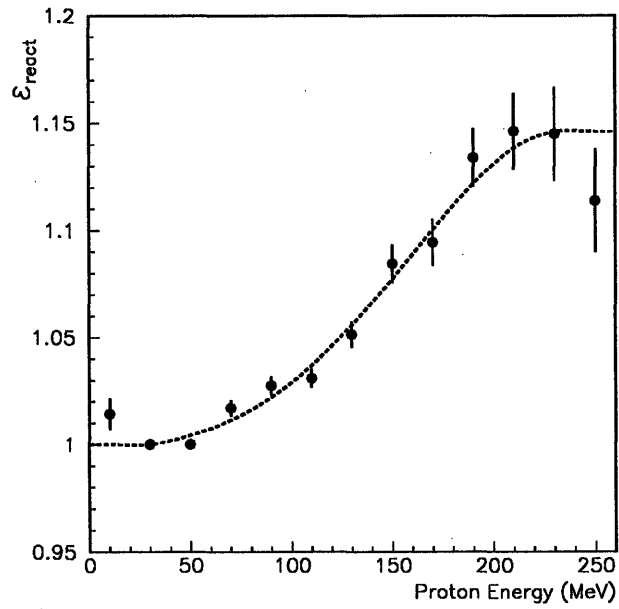


Figure 4-7: The proton reaction correction factor as a function of proton energy for events without MWPC information. The dotted line is the fit used to correct the data.

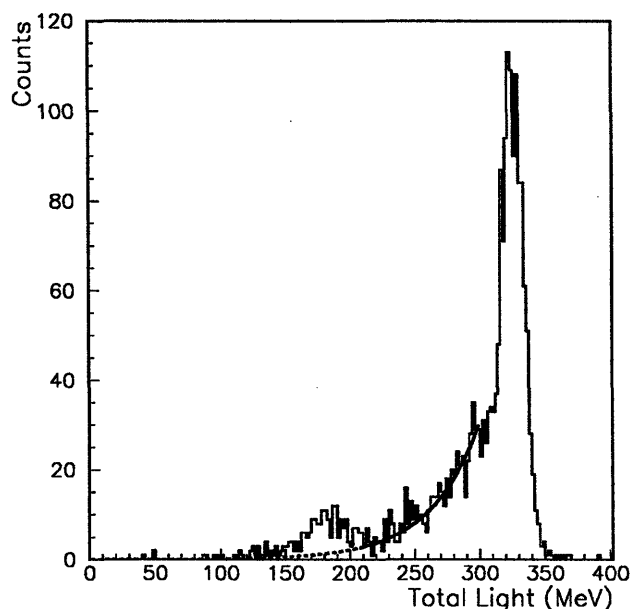


Figure 4-8: The total detected light of absorption events selected by the MWPC's following the interaction of 239 MeV π^+ 's with ^3He . The line is an exponential fit to the reaction tail, used to determine the pion contamination.

In order to obtain an estimate of the uncertainty in this technique, the absorption of 239 MeV π^+ 's on ^3He was used. There are three protons in the final state, each of which has three momentum components, so nine variables are needed to determine the system. Energy and momentum conservation fix four, leaving five undetermined. The MWPC's can provide two angles for each proton, over-determining the system. Thus, it is possible to use the MWPC's to select a set of absorption events independently of the plastics, and thus essentially independently of the reaction correction. There is a small πpp contamination remaining in the selected events. The magnitude of this contamination can be determined by examining the total energy spectrum of the events and fitting the tail to an exponential as illustrated in figure 4-8. After this correction has been done, the number of absorption events in the file has been determined.

Once a set of events has been obtained, it is run through the usual analysis chain. Some of the events are vetoed by the various PID cuts described above, but those remaining are corrected by the weighting factor described in this section to compensate. The analysis calculates the number of absorption events in the file, which is then compared to the number determined above.

It was found to be off by 3%, which was taken as an estimate of the error associated with the technique. Since the reaction correction is applied to each charged particle individually, this would be 1% per particle. However, there is some correlation between this method of estimating the error and the method use to calculate the correction. Therefore, 2% per charged particle was used in order to be conservative.

4.6 Pion Contamination

Although the various PID methods used correctly identify most of the final state charged pions, there still remain some which have slipped through the cuts. The magnitude of this effect must be determined so that the final result can be corrected. The method is similar to that used for calculating reaction corrections. A sample of events is selected which include a charged pion in the final state. These events are then passed through the analysis chain to determine their effect on the cross section. The small resulting contamination is attributed fully to mistaken identification of the pion, ignoring any second order effects such as two particles in the event being misidentified.

As there is only one charged pion in each event, the fractional contamination is the chance that a single pion is misidentified. To use this result, a second cross section is calculated in a similar manner to the absorption cross section, but measuring the probability of finding a charged pion in the final state. For this cross section, only standard PID is used, and second order effects due to the other methods are ignored. In addition, the restriction to the LADS acceptance requiring that a charged particle deposit over 35 MeV of light, if it was the only charged particle detected, has not been applied here. This treatment explains the large uncertainty applied to the pion contamination fraction calculated below. Table 4.2 gives these experimental pion scattering cross sections. Care has to be taken if any attempt is made to compare these numbers with other results. The restrictions made to LADS's acceptance, while of minor importance for the absorption cross section, are significant here since the scattering cross section peaks at zero degrees. The cross section for finding a pion in the final state is broken up according to the charged particle multiplicity, multiplied by the pion contamination fraction, and subtracted from the absorption cross section.

To isolate events with a pion in the final state, interactions of π^+ 's with ^2H are used. The analysis is performed separately for all three energies, so the pions have similar energy distributions in the sample set as in the data being corrected. Events are selected which have

Pions			
	118 MeV	162 MeV	239 MeV
^3He			
1C	100.7	123.7	67.8
2C	60.0	123.7	84.3
3C	2.9	11.4	15.7
Total	163.9	260.0	169.8
^4He			
1C	111.8	123.5	83.6
2C	28.2	68.4	67.6
3C	1.5	4.8	10.3
Total	141.7	197.3	162.8
N			
1C	279.5	240.5	172.1
2C	64.9	122.9	130.0
3C	3.9	9.4	22.9
4C	0.5	1.2	3.4
Total	348.7	373.9	328.3
Ar			
1C	499.8	399.6	319.0
2C	97.4	176.5	203.9
3C	8.0	16.1	35.8
4C	0.9	2.1	5.4
Total	606.0	594.2	564.0

Table 4.2: The cross sections for detecting a charged pion with the acceptance limitations described in the text are given in millibarns.

two charged particles in the final state, each of which has two MWPC hits with a vertex in the interior of the target. Then the MWPC information is used to separate out π -p scattering events. The assumption is made that the final state neutron is at rest. The energy of the two particle system is calculated first taking particle one as the pion and particle two as the proton, and then recalculated the other way. If either calculated energy matches the initial energy of the system, the event is tentatively identified as π -p scattering.

Now the possible sources of contamination in these events are absorption and SCX (where the two protons are the detected particles). To remove any remaining contamination from these events, cuts are made around 180° in ϕ -difference, and between 130° and 170° in CM θ -difference. SCX typically does not lead to events which are back-to-back in ϕ , and absorption leads to events which are 180° apart in both. Finally, both particles are assumed to be protons and their energy information is used to calculate a missing mass. If this results in the π^0 mass, the event is vetoed. The combination of these cuts leads to a very clean selection of data.

There is one more complication which needs to be considered. One reason a pion might be misidentified is because it underwent a reaction in the scintillator. This reaction can lead to a number of energetic particles in the detector, some of which might be mistakenly identified as photons. The magnitude of this effect is not large, but it needs to be handled carefully. The problem is that such events are corrected for in the SCX correction discussed above. Thus, for determining the pion contamination fraction, we do not include events where no pion was detected, but a γ was. Unfortunately, in the SCX correction, events with detected photons are not only vetoed, but an additional fraction of the magnitude is subtracted off (typically about 80%). Thus, the same procedure must be followed here to ensure that these events are not being doubly counted. Coincidentally, this procedure also accounts for any remaining SCX contamination in our selected events.

As an illustration of the above concepts with equations, consider the correction to the two charged particle absorption cross section:

$$\sigma_{2C} = \sigma_{2C}^{0\pi} - f_\pi \times \sigma_{2C}^{1\pi};$$

where,

$$f_\pi = \frac{N_{0\pi}^{0\gamma} - f_{SCX} \times N_{0\pi}^{>1\gamma}}{N_\pi}.$$

N_π is the number of events in the sample set of pions. $N_{0\pi}^{0\gamma}$ and $N_{0\pi}^{>1\gamma}$ are the number of events from this sample set for which the analysis chain reports zero charged pions. And finally, f_{SCX} is the pion contamination factor.

The calculated values of f_π were 0.7%, 0.9%, and 1.4% at 118, 162, and 239 MeV, respectively. These values were also calculated for the no-MWPC data by using the same set of selected events and turning off the chamber reconstruction code. The values in this case were 0.7%, 0.8%, and 1.5%. Estimating the uncertainty in this result is difficult. For the heavier nuclei, the error in this fraction is insignificant because the absorption cross section is a significant fraction of the total cross section. On ^3He , however, the total scattering cross section is almost an order of magnitude larger than the absorption cross section, and the error in f_π is significant. One-half of the size of the measured correction was conservatively taken as the uncertainty on this value.

4.7 Beam Normalization

A “logical beam pion” is defined in section 2.6. The number of logical beam pions which occurred during each run is counted by a hardware scaler. This number is used to calculate the number of pions on target during the course of the run. Several corrections to this number have to be made and will be described below. They cover beam events which have unusual timing, the possibility of reactions in S_{beam} , the effects of pion decay, and the loss of beam flux due to reactions.

A beam pion is defined by a coincidence between several counters, the important one for this discussion being S_{beam} . Figure 4-9 shows a timing spectrum from the S_{beam} TDC for beam events. Beam events consist of a random sampling of the cases in which there was a logical beam pion, irrespective of whether any particles were detected in LADS. The spectrum shows a clean peak for good beam pions, and another significantly smaller peak about 6 ns earlier (its magnitude varies with pion energy between 1% and 7% of the total). These events probably arise from pions hitting S_{beam} 's PMT, which would explain the timing. They are not good beam particles. These events are isolated by making a cut on the S_{beam} TDC spectrum. For the figure shown, an event is not considered unless the S_{beam} TDC is between 240 and 280. The number of pions on target also must be modified to account for this cut. The hardware scaler's value for logical beam is multiplied by the fraction of the total beam events that are in the “good beam” peak.

The S_{beam} counter is also attached to an ADC. This allows for the beam to be corrected for those cases in which the pion reacts inside the S_{beam} scintillator. If the pion reacts in the counter, it usually deposits more energy than a pion which did not react. This energy typically

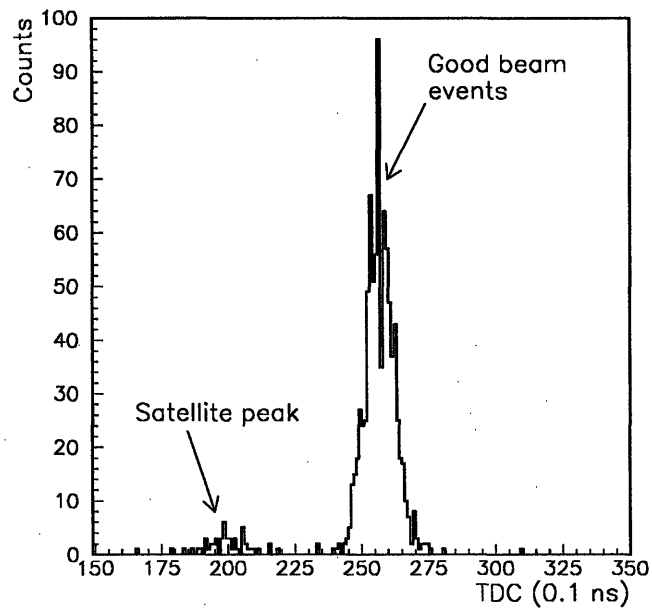


Figure 4-9: S_{beam} 's TDC spectrum for beam events at 118 MeV incident pion energy.

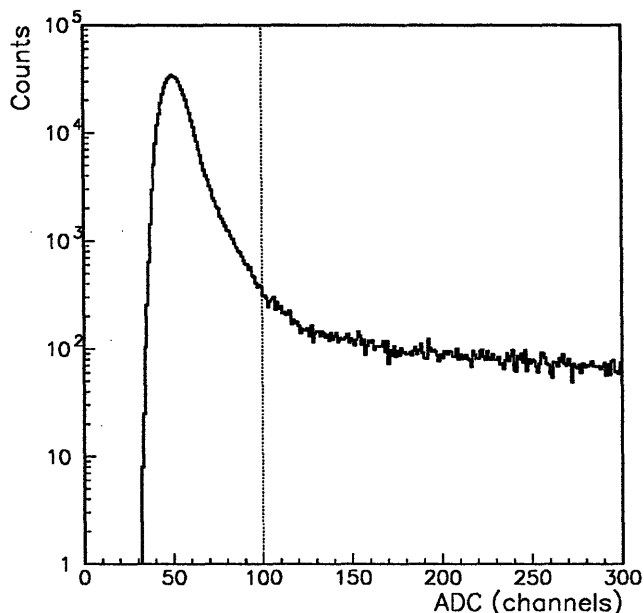


Figure 4-10: S_{beam} 's ADC spectrum for events with an incident pion energy of 118 MeV. The dotted line shows the cut separating "good" beam pions from "bad" beam pions.

appears as light resulting in a larger ADC value. Figure 4-10 shows an ADC spectrum from the S_{beam} counter. A rather arbitrary cut at 100 channels was made, and the event rejected if the ADC value was above this. This cut affected only about 1% of the events. In order to correct the number of pions on target, the beam events were used again, and the hardware scaler's value for logical beam was multiplied by the fraction of the total beam events that have ADC values less than 100. Actually, the ADC and TDC cuts were applied simultaneously to account for any correlations. The uncertainty associated with these two cuts is simply the statistical error in the measurement of the fraction of the beam that fails to satisfy them. In all cases this was less than 1%.

The next two corrections made to the beam flux dealt with π^+ decay. The pion's path was divided into two segments: the route through the beamline to S_{beam} , and the distance between S_{beam} and the center of the target. To determine muon contamination in the beam before S_{beam} , the program TURTLE was run for the $\pi M1$ beamline with the addition of S_{time} and S_{beam} . The fraction of the simulated beam which consisted of muons was 2.0% at 119 MeV and 1.8% at 162 and 239 MeV. Reasonable variations of the beamline geometry supplied to TURTLE resulted

in variations in these numbers of less than $\pm 1.0\%$, so this was taken as the uncertainty. For the path between the beam counter and the target center, a simple decay formula was used:

$$N(\text{center}) = N(S_{\text{beam}}) \times e^{(-\frac{L}{\beta\gamma\tau})}$$

Where,

$N(x)$ = the number of pions at position x ;

L = the pathlength = 47.5 cm;

β = the velocity of the particle;

$\gamma = 1/\sqrt{1 - \frac{1}{\beta^2}}$;

and τ = the lifetime of the π^+ = 2.60×10^{-8} .

The fraction of the pions which have decayed over this path is 2.7% at 119 MeV, 2.5% at 162 MeV, and 2.1% at 239 MeV. The uncertainties in these fractions are determined by the uncertainty in the pathlength and in β , and are insignificant.

It is also necessary to correct the beam flux to account for any pions which miss the target. The possible sources for this problem can be divided into two broad categories: the removal of pions from the beam and the spreading of the beam. The first of these is due mainly to nuclear interactions in the material between S_{beam} and the interaction point. For the path between the downstream end of S_{beam} to the upstream end of the gas used as the target (≈ 3 cm into the gas for the MWPC data), the total probability of an interaction was calculated by using the total nuclear interaction cross section for the material and the material's thickness. The assumption was that any nuclear interaction removed the pion from the beam. Over the length of the gas used as the target, the beam flux was slowly attenuated. The interaction probability was calculated as above, and integrated over the length of the gas to obtain an average number of pions on target. The uncertainty associated with this correction is dominated by the uncertainties in the total nuclear cross sections in the materials. As these cross sections are generally known to better than 30%, 30% of the fraction of the beam flux removed from the beam was taken as the uncertainty, which is always less than 1%.

The spreading of the beam is mainly due to multiple scattering, although non-parallel components of the beam's momentum also play a role. To estimate the fraction of the beam which hits the target, interactions in the air before and after the target were used. Events were selected which had a two track vertex from the MWPC's. The ratio of the number of events within a 2 cm radius to the total number of events was measured for 1 cm slices before and after the target. The results are shown in figure 4-11. Note that both before and after the target the ratio rises to a local maximum and then decreases again. This behavior is easy to

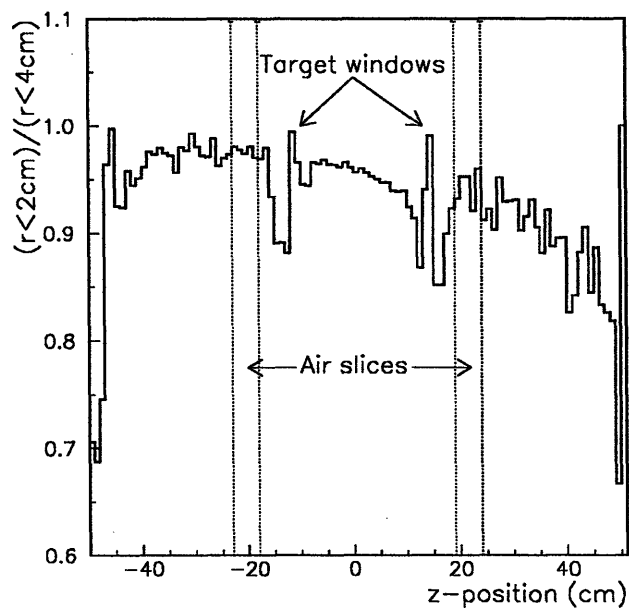


Figure 4-11: The ratio of the number of events with a vertex within 2 cm of the beam axis to the number of events within 4 cm of the beam axis, used to determine the fraction of the π^+ beam which misses the target. The data are for a 162 MeV beam and a ^4He target.

understand. Near the ends of the small chamber the acceptance of the MWPC's becomes a strong function of the radius at which the interaction occurs. This effect is much more apparent on the downstream end because of the Lorentz boost. Near the target, more particles pass at an oblique angle through the endcap windows of the target, raising the threshold for detection considerably. To calculate the fraction of the pions which passed through the target, 5 cm slices both before and after the target were used, in the vicinity of the local maxima. The average of these two values was used as an estimate of the fraction at the center of the target. The percentage of the pions missing the target varied from 4% to 9% with the target gas and the beam energy.

The systematic uncertainty in this correction factor dominates the error in the beam normalization. The reasons the results are so uncertain include the fact that a linear fit was used in the model, the lack of knowledge of how the threshold and acceptance effects described above modify the result, and the possibility that the beam has a better focus between the two air slices than in them. The uncertainty used for this factor was one-half of the average difference between the upstream and the downstream values. This varied between 1.5% and 3%, so 2.5% was used. This represents the systematic uncertainty, which is correlated between the empty and the full runs. Any particular measurement will also have an associated statistical uncertainty. However, this is usually negligible in comparison.

In summary, the total number of pions on target were calculated from the equation:

$$N_{\text{beam}} = N_{\text{beam}}^{\text{scaler}} \times f_{\text{ADC/TDC}} \times f_{\text{contamination}} \times f_{\text{decay}} \times f_{\text{react}} \times f_{\text{air}}.$$

4.8 Number of Target Scatterers

The number of target scatterers is straightforwardly calculated from the temperature and pressure of the target gas, which were both monitored during the experiment. The formula used was:

$$N_{\text{scatterers}}(\text{Nuclei}/\text{cm}^2) = \frac{N_0 p T_0 L N_m}{V_M T Z};$$

where,

N_0 = Avagadro's number;

p = pressure (atmospheres);

T_0 = 273.15° K;

L = target length = 20 cm (MWPC data) or 25.7 cm (no MWPC data);

N_m = the number of nuclei per molecule;

V_M = the molar volume at STP;

T = temperature ($^{\circ}$ K);

Z = the compressibility of the gas.

For the pressures involved in this experiment, deviations from the ideal gas law become important. The factor of compressibility, which is unity for an ideal gas, amounted to as much as a 5% correction. It does not significantly contribute to the uncertainties, however, as it has been precisely measured [91]. The uncertainty in this measurement is dependent on the precision of the pressure and temperature measurements, as well as the target length measurement. Each of these three components was tested and found to be better than 1%. Thus, 1% was the uncertainty associated with the number of target scatterers.

4.9 Dead Time and Prescale Factors

There is one more major normalization factor which plays a role. It accounts for the DAQ's dead time, mainly due to computer busy time, and for the prescale factors applied to the data. As described in section 2.7, prescale units were used to control the fraction of each trigger type written to tape. The events analyzed from the tape have to be multiplied by a factor so that they represent the actual number of such events that occurred for each run. Hardware scalers kept track of the total number of events of each trigger type that occurred during each run. A latch recorded the trigger type of each event. In the analysis, the data are divided into the different trigger types by the latch value. Each trigger type is separately analyzed, and then multiplied by a factor equal to the ratio of the hardware event type scaler to the total number of events of that type in the run analyzed. This correction accounts for both the dead time effects and the prescale factors. Because this correction is based on absolute numbers, there is no uncertainty associated with it.

4.10 Uncertainties

In any analysis this complex, the uncertainty associated with the final result is a complex combination of statistical and systematic errors, propagated through the various formulae to obtain the final uncertainty. The statistical errors are generally well understood, and the theory of their propagation is well established. The systematic uncertainties are generally much more difficult to assess accurately, as they frequently represent the experimenter's incomplete understanding of his experiment. For this reason, they are typically estimated by making "reasonable" variations in the analysis process, and determining the effects of these variations on the final result.

This section will describe the general techniques used in the error analysis. Combining all the formulae in the previous sections, the cross section is:

$$\sigma_i = [\sigma_{i,\text{full}}^{0\gamma} - f_e \times \sigma_{i,\text{empty}}^{0\gamma}] - f_{\text{SCX}} \times [\sigma_{i,\text{full}}^{>1\gamma} - f_e \times \sigma_{i,\text{empty}}^{>1\gamma}] - f_\pi \times [\sigma_{i,\text{full}}^\pi - f_e \times \sigma_{i,\text{empty}}^\pi].$$

Here,

$$f_{\text{SCX}} = \frac{(1 - \epsilon_\gamma)^2}{\epsilon_\gamma^2 + 2\epsilon_\gamma(1 - \epsilon_\gamma)};$$

$$\epsilon_\gamma = \frac{2}{2 + \frac{\sigma_{\text{full}}^{1\gamma} - f_e \times \sigma_{\text{empty}}^{1\gamma}}{\sigma_{\text{full}}^{2\gamma} - f_e \times \sigma_{\text{empty}}^{2\gamma}}};$$

$$f_\pi = \frac{N_{0\pi}^{0\gamma} - f_{\text{SCX}} \times N_{0\pi}^{>1\gamma}}{N_\pi};$$

$f_e = 1.2$ for MWPC data; 1.0 for no-MWPC data.

Now, each cross section in these equations can be written:

$$\sigma_{x,y}^z = \frac{1}{N_{\text{beam}} N_{\text{scatterers}}} \sum_{j=1}^{N_{x,y}^z} \left(\prod_{i=1}^{N_{\text{char}}^j} \epsilon_{\text{react}}(E_i^j) \right).$$

The error analysis is considerably simplified if some assumptions are made. The first is that the uncertainty in the factor f_π is uncorrelated with all other uncertainties in the problem.

The second is that the variation in:

$$\prod_{i=1}^{N_{\text{char}}^j} \epsilon_{\text{react}}(E_i^j),$$

has no effect on the statistical error associated with $N_{x,y}^z$. This assumption is justified because of the small event-by-event variation in the product (especially when the conditions include a particular charge multiplicity).

The next step is to write the cross section as a function of all of the variables for which the uncertainties are uncorrelated (from run to run, or more importantly, between the full and the empty runs). Some variables have both correlated and uncorrelated components. For example, the fraction of the beam missing the target as determined by using slices of air has a statistical uncertainty that is uncorrelated from run to run. It also has an uncertainty based on how closely the method's assumptions reflect reality. This latter error is correlated from run to run. The differences between these two errors are taken into account by constructing two functions:

$$f_{\text{air}} = f_{\text{air}}^{\text{corr}} \times f_{\text{air}}^{\text{uncorr}}.$$

$f_{\text{air}}^{\text{uncorr}}$ has a value equal to f_{air} with an error equal to the statistical, uncorrelated error in its determination. $f_{\text{air}}^{\text{corr}}$ equals one with an error equal to the systematic, correlated error in the method. This allows the cross section to be written as a function of independent variables.

Then the total uncertainty is determined from the equation:

$$(\Delta f)^2 = \sum_i \left(\frac{\partial f}{\partial x_i} \right)^2 (\Delta x_i)^2.$$

This equation is evaluated for each reported multiplicity. Some of the terms are always insignificant, and the dominant terms vary from case to case. For example, the beam normalization and target scatterers error is dominated by the error in $f_{\text{air}}^{\text{corr}}$, and the remaining uncertainties in these terms are negligible. In all cases the error in the ϵ_{react} is important, and its importance grows with the number of charged particles in the final state. The significance of other errors depends on the relative importance of the SCX, empty, and pion contamination adjustments to the cross section for the particular channel involved.

4.11 Results: Charged Multiplicities

The final results from this analysis are presented in Table 4.3. Discussion of the significance of these results, as well as graphical presentations, will be delayed until chapter 6. In addition to the final results, the components of the cross sections with and without an MWPC vertex are presented in table 4.4.

Charged Particle Multiplicities			
	118 MeV	162 MeV	239 MeV
³ He			
1C	-0.5 ± 1.0	0.3 ± 1.8	-1.0 ± 1.5
2C	20.0 ± 1.3	17.0 ± 1.4	5.9 ± 1.1
3C	5.3 ± 0.4	6.9 ± 0.5	3.2 ± 0.3
Total	24.8 ± 2.1	24.2 ± 3.1	8.1 ± 2.7
⁴ He			
1C	4.0 ± 1.2	3.3 ± 2.1	-0.9 ± 2.7
2C	38.2 ± 2.2	34.8 ± 2.0	15.7 ± 1.4
3C	7.2 ± 0.5	9.8 ± 0.7	6.9 ± 0.5
Total	49.5 ± 3.1	48.0 ± 3.8	21.9 ± 4.1
N			
1C	40.9 ± 2.8	27.2 ± 4.4	11.2 ± 5.1
2C	114.9 ± 6.2	98.7 ± 5.4	57.0 ± 3.9
3C	24.4 ± 1.7	33.8 ± 2.4	31.9 ± 2.3
4C	1.4 ± 0.1	3.6 ± 0.3	6.3 ± 0.6
Total	181.6 ± 9.9	163.4 ± 10.5	107.0 ± 9.9
Ar			
1C	134.8 ± 7.6	96.2 ± 9.6	50.7 ± 10.3
2C	222.0 ± 12.0	211.7 ± 11.5	152.2 ± 9.0
3C	34.5 ± 2.4	54.1 ± 3.8	67.9 ± 4.8
4C	1.5 ± 0.2	4.0 ± 0.4	10.3 ± 0.9
Total	393.2 ± 20.6	366.1 ± 21.8	281.8 ± 21.1

Table 4.3: The cross sections for each charge multiplicity are given in millibarns. All corrections have been applied as described in the text. No corrections have been made for missing acceptance. Both systematic and statistical uncertainties are included.

MWPC/no-MWPC			
	118 MeV	162 MeV	239 MeV
³ He			
1C	-0.2/ - 0.3	-0.2/0.5	-0.7/ - 0.3
2C	17.7/2.3	15.0/1.9	5.4/0.5
3C	5.2/0.1	6.6/0.3	3.1/0.1
Total	22.8/2.0	21.5/2.7	7.8/0.3
⁴ He			
1C	2.7/1.3	2.8/0.5	-0.4/ - 0.6
2C	35.0/3.2	31.8/3.0	14.5/1.2
3C	7.0/0.2	9.5/0.3	6.8/0.2
Total	44.8/4.7	44.3/3.8	21.0/0.8
N			
1C	34.7/6.2	22.4/4.8	9.8/1.5
2C	107.0/7.9	91.7/7.0	53.0/3.9
3C	23.8/0.6	32.8/1.1	31.0/0.9
4C	1.4/0.0	3.5/0.1	6.2/0.1
Total	166.9/14.8	150.5/12.8	100.5/6.5
Ar			
1C	114.7/20.1	80.5/15.7	39.8/10.9
2C	207.3/15.2	197.1/14.6	133.6/18.7
3C	33.4/1.1	52.3/1.7	62.4/5.5
4C	1.4/0.1	4.0/0.0	9.5/0.7
Total	356.8/36.4	334.0/32.0	246.0/35.8

Table 4.4: The MWPC and no-MWPC components of the absorption cross section (mb) are given as a fraction.

Chapter 5

Neutrons and Deuterons

Obtaining the total cross sections and the charged particle multiplicities discussed in the last chapter is only the first part of the process. Each of those multiplicities can be further broken up by numbers of accompanying neutrons, and by the numbers of protons and deuterons. For no combination of target and energy were significant numbers of final state tritons or ^3He 's identified. In this chapter the identification of neutrons and deuterons will be discussed.

5.1 Neutron Identification

The neutron's interaction with plastic scintillator is significantly different from the proton's interaction as discussed in section 2.3. A proton scatters from a large number of electrons, gradually losing its kinetic energy which is eventually converted into light. A neutron also interacts with electrons through the electromagnetic force, even though its total charge is zero. The strength of this interaction is much smaller than the proton-electron interaction, however, so the neutron transfers very little energy to the scintillator's electrons.

It is possible for the neutron to undergo a nuclear interaction with a component of the scintillator. During this interaction, kinetic energy can be transferred to a charged particle, which will in turn create a detectable signal in the scintillator. The probability of this occurring will obviously depend on the amount of scintillator the neutron traverses. It will also depend, in a less obvious manner, on the energy of the neutron. The proton-neutron scattering cross section is decreasing with increasing energy in this range, so the probability of an interaction is

decreasing. At the same time, the amount of energy transferred in an interaction is increasing with the neutron's energy. This increases the probability of the scattered charged particles being above the detection threshold. This will have an effect for very low energy neutrons, but is not as significant for higher energy neutrons. The convolution of these two effects lead to a detection efficiency that increases between zero and about 50 MeV, and then starts to slowly decrease. The maximum is about 40%, and the average is about 35%. This efficiency will be further discussed in section 5.1.3. For now it is sufficient to note that neutrons are detectable.

5.1.1 Defining a Detected Neutron

A neutral particle is identified by the trigger when light is detected in an E-block and no light is detected in the corresponding dE. This basic method is also used to identify neutrals in the analysis, but a number of modifications are applied. Some of these have been mentioned in prior sections.

First, the CTP routines (section 3.1) reconstruct particles from the sectors which have detected light. During this process, light in adjacent sectors is combined into single particles. This combination is performed because the probability that a charged particle scatters into an adjacent sector is significantly higher than the probability that a neutral is present and detected in that sector. In addition, it is possible for a single neutral to deposit light in two adjacent sectors. Since this is also a more likely occurrence than there being two neutrals, each of which deposits light in adjacent sectors, these are combined as well.

There was also a problem from charged particles slipping through the cracks between the dE's and appearing as neutrals to the detector. As described in section 4.3.3, the MWPC's were used for additional charged particle identification. Cylinder neutrals which had an associated hit in the outer MWPC, and endcap neutrals which had an associated hit in the inner MWPC, were relabeled as charged particles.

The reconstruction of adjacent blocks into single particles cleared up a large part of the problem associated with particles depositing energy in multiple sectors. Were multiple scattering the only possibility, this would probably have been sufficient. However, particles can also undergo nuclear interactions in the scintillator, which can lead to large changes in their flight paths. It is thus possible for particles to deposit light two sectors over—a possibility which is not handled by CTP. To fix this problem, neutrals which were within 30° of a charged particle were not counted. If two neutrals had an opening angle of less than 30° , only one was counted.

This restriction reduced the marginal phase space coverage of the detector with each additional particle detected. The 30° opening angle corresponds to 7% of 4π steradians. The fact that for each charged particle detected in a cylinder sector, no neutral can be identified in that sector or either adjacent sector corresponds to a reduction of 10% of 4π . These areas overlap, and for a three charged particle final state, the effective solid angular coverage of LADS for detecting neutrals is about 65% of 4π .

There are two additional restrictions imposed on detected particles. The first is that all particles have to deposit at least 2.5 MeV of light in the detector or they will be considered noise and ignored completely in the analysis. The second is that any particle with a reduced time of flight greater than 7 ns is ignored in the analysis. For a nucleon, a reduced TOF of 7 ns corresponds to 10 MeV kinetic energy. For a proton, this would be under the detector threshold and would clearly be noise. For a neutron, this is approaching the detector threshold, but this threshold is rather soft and it is possible to detect neutrons under 10 MeV.

The main reason to limit the maximum reduced TOF of the neutrons is to avoid the detection of evaporation neutrons. As discussed in section 1.2, a nucleus in an excited state will decay through a combination of nucleon and photon emission. The emitted nucleons will typically be under 10 MeV, and neutrons are more prevalent than protons due to the coulomb barrier. When a pion is absorbed on a nucleus heavier than ^4He , the residual nucleus will frequently be left in an excited state. This will decay, leading to additional energetic nucleons in the final state which did not participate in the absorption process. These evaporation nucleons must be identified and discarded. The energy threshold of the detector is high enough to stop the protons, and the TOF cut is used to veto the neutrons.

The detector's timing calibration was obtained using charged particles, which have a different distribution of energy deposited in the scintillator than neutral particles. Essentially, the flight path for a neutron from the target to the point it deposits light in the scintillator is not well known. The initial light will be deposited somewhere inside the scintillator instead of near the front edge. Therefore, the energy corresponding to a neutron's calculated TOF will be incorrect. It was experimentally determined that 7 ns corresponds to about $20 \text{ MeV} \pm 10 \text{ MeV}$ instead of 10 MeV, resulting in an effective neutron energy threshold approximately equal to the proton energy threshold.

5.1.2 Obtaining the Detected Neutron Cross Sections

Once the restrictions are applied and a detected neutron is well defined, determining the multiplicities of detected neutrons is analogous to determining the charged particle multiplicities as described in Chapter 4. Each charge multiplicity is broken up into subsets with zero, one, two, or three accompanying neutrons. In other words, the channels 1C0N, 1C1N, 1C2N, 1C3N, 2C0N, etc. are treated individually. The data are split into subsets with and without MWPC vertices. Empty subtractions are performed, and corrections for SCX contaminations are made. The details of these calculations are exactly the same as in Chapter 4, and will not be repeated.

The pion contamination correction was split between the 0N and 1N channels, with the bulk of the change to the 0N. The reason for the pion's misidentification could be that it underwent a reaction in the scintillator, which might give rise to a detected neutron. Thus, the events used to determine the pion contamination correction factor, f_π (section 4.6), were examined to determine how often there was a detected neutron in the final state. This occurred only 4% of the time. This set of events had been selected by requiring π^+ -p scattering, so the possibility of π^+ -n scattering was not included. However, the π^+ -p scattering cross section is a factor of nine larger than the corresponding π^+ -n cross section in this energy region. In addition, the neutron detection efficiency is 36% (see section 5.1.3). These effects result in an additional 4% contribution to the 1N channels. Thus, 8% of the pion contamination correction was subtracted from the 1N channels, and the remainder from the 0N channels.

There are some additional corrections that need to be made to handle other contaminations. Possible sources are SCX, charged particles slipping through the cracks and by the MWPC's, charged particles reacting in the scintillator and causing a signal in another sector with an opening angle of greater than 30° , and general noise in the detector. In all cases, the total cross section for a particular charge multiplicity will not be changed, but strength will be moved around between the numbers of detected neutrons.

When a neutral particle is detected in the scintillator, its TOF is used to determine whether it is a photon or a neutron. An example of the photon-neutron separation has previously been shown in figure 4-3. Sometimes a neutron will be misidentified as a photon or a photon will be misidentified as a neutron due to the resolution of the detector. The first of these cases is approximately corrected for by the neutron detection efficiency calculation. The magnitude of the second effect can be estimated from figure 4-3. A gaussian was fit to the distribution in the region less than the 1.55 ns cutoff. The area under this gaussian which fell above the 1.55 ns cutoff was 2% of the total. This was used as an estimate of the probability of a

mistaken identification. The probability of a mistaken identification is taken into account in the calculation of the gamma detection efficiency. Thus, this amount has already been subtracted, but from the channel with one fewer detected neutrons. Thus the correction discussed here involves subtracting 2% of the detected SCX cross section from the XC1N channel, and adding this strength back into the XC0N channel. It should be noted that even in the case of ^3He at 239 MeV where the ratio of detected SCX to the absorption cross section is the highest, this effect is small.

The probability of a charged particle slipping through the cracks between the dE's is on the order of 1%. The MWPC's will catch well over 50% of these, so the total magnitude of the remaining effect is less than 0.5%. In addition, a lot of the remaining magnitude is due to a π^+ slipping through the cracks after quasi-elastic scattering. The restriction of phase space coverage discussed in section 4.3.3 (if only one charged particle is detected, it must have over 35 MeV of light), also greatly reduces the magnitude of this effect. Thus, the magnitude of a correction would be on the order of 0.1%. This is small, and any associated uncertainties are small, so it will be neglected.

The last two possibilities will be considered together. The correction for detected neutrals arising from either particles reacting in the scintillator or background noise in the detector should be proportional to the cross sections for detecting the same number of charged particles and one fewer neutrons; *i.e.*:

$$\sigma_{\text{XCYN}} = \sigma_{\text{XCYN}}^{\text{detected}} - f \times \sigma_{\text{XC(Y-1)N}}$$

If the contamination were due to reactions, f would be proportional to the number of actual particles, or $X+Y-1$. To determine the magnitude of the correction, use will be made of the fact that there are no neutrons in the final state following absorption of a π^+ on ^3He . When the magnitude of XC1N is compared to the magnitude of XC0N, it is found that the number of neutrons is brought closest to zero by subtracting $0.016 \times \sigma_{\text{XC0N}}$ from the XC1N cross section and adding the same amount to the XC0N cross section. Thus, the best fit has A constant, so the contamination is most likely due to general noise in the detector. This is consistent with figure 5-1 from the next section which indicates that there is background noise at all opening angles.

The above corrections were performed for all channels, and the results appear in tables 5.1 and 5.2.

^3He			
	118 MeV	162 MeV	239 MeV
1C0N	-0.4	-0.4	-1.0
1C1N	-0.1	0.6	0.0
1C2N	0.0	0.1	0.0
1C3N	0.0	0.0	0.0
2C0N	20.1	16.8	5.8
2C1N	-0.1	0.1	0.1
2C2N	0.0	0.0	0.0
2C3N	0.0	0.0	0.0
3C0N	5.4	6.9	3.2
3C1N	0.0	0.0	0.0
3C2N	0.0	0.0	0.0
3C3N	0.0	0.0	0.0

^4He			
	118 MeV	162 MeV	239 MeV
1C0N	2.8	2.6	-1.4
1C1N	1.1	0.7	0.4
1C2N	0.0	0.0	0.0
1C3N	0.0	0.0	0.0
2C0N	35.9	32.3	14.0
2C1N	2.3	2.5	1.6
2C2N	0.0	0.0	0.1
2C3N	0.0	0.0	0.0
3C0N	6.4	8.7	6.0
3C1N	0.8	1.1	1.0
3C2N	0.0	0.0	0.0
3C3N	0.0	0.0	0.0

Table 5.1: Detected neutron multiplicities (mb). All corrections described in the text have been made with the exception of that for the neutron detection efficiency.

N			
	118 MeV	162 MeV	239 MeV
1C0N	30.7	19.8	6.5
1C1N	9.7	6.8	4.2
1C2N	0.6	0.6	0.5
1C3N	0.0	0.0	0.0
2C0N	101.2	83.9	45.2
2C1N	13.2	13.9	10.8
2C2N	0.6	0.8	1.0
2C3N	0.0	0.0	0.0
3C0N	22.0	29.5	25.9
3C1N	2.3	4.2	5.5
3C2N	0.1	0.2	0.4
3C3N	0.0	0.0	0.0
4C0N	1.3	3.2	5.2
4C1N	0.1	0.4	1.0
4C2N	0.0	0.0	0.1
4C3N	0.0	0.0	0.0
Ar			
	118 MeV	162 MeV	239 MeV
1C0N	95.0	61.0	25.2
1C1N	36.4	30.6	21.0
1C2N	3.3	4.4	4.2
1C3N	0.2	0.2	0.4
2C0N	183.3	163.5	105.2
2C1N	36.6	43.5	40.5
2C2N	2.6	4.6	6.1
2C3N	0.1	0.2	0.4
3C0N	30.0	44.7	50.9
3C1N	4.2	8.7	15.3
3C2N	0.2	0.7	1.7
3C3N	0.0	0.2	0.1
4C0N	1.3	3.5	8.2
4C1N	0.1	0.5	1.9
4C2N	0.0	0.0	0.1
4C3N	0.0	0.0	0.0

Table 5.2: Detected neutron multiplicities (mb). All corrections described in the text have been made with the exception of that for the neutron detection efficiency.

5.1.3 The Neutron Detection Efficiency

The neutron detection efficiency is sensitive to a variety of characteristics of the detector which affect the detection threshold. It is therefore preferable to calculate the efficiency directly from the data. The method used is similar to that used for determining the reaction detection efficiency as discussed in section 4.5. A set of events which include neutrons with known momenta are isolated. The fraction of these neutrons which are detected can then be determined as a function of a set of underlying variables, such as the neutron's energy or polar angle.

To obtain the set of events, data were used from the interaction of 239 MeV π^+ 's with ^4He . Events were selected in which three charged particles were detected, each of which had MWPC information and was labelled a proton by PID. The event vertex was restricted to the target region. A missing mass cut was applied to ensure that an absorption reaction occurred, PID identified the protons correctly, and there was no energy lost due to reactions. The energy and momentum of the neutron were then calculated from the initial pion momentum and the momenta of the three detected protons.

Now, a neutral detected with an opening angle of less than 30° from a charged particle is ignored, as described in section 5.1.1. This effect should not be included in the neutron detection efficiency as its degree of importance depends on the characteristics of the particular event in question. It is particularly important to consider it when using this method for calculating the efficiency, since the distribution of neutrons following multi-nucleon absorption on ^4He shows the effects of soft-FSI interactions which enhance the cross section for small neutron-proton opening angles. Therefore only events in which the missing momentum has an opening angle with each proton of greater than 35° were included in the set of events.

Finally, since it is known that there is some background noise in the detector, it is necessary to ensure that the detected neutral is the neutron from ^4He whose energy has been reconstructed. Therefore, an opening angle cut between the detected "neutron" and the missing momentum is used to separate good neutrons from noise. Figure 5-1 shows the opening angle between the missing momentum and the trajectory of the detected neutron. The opening angle peaks under 10° , and over 90% of the events have an opening angle of less than 30° , with a small background noise outside of this. Thus, 30° was chosen as the maximum allowed opening angle.

Figure 5-2 shows the neutron detection efficiency calculated by this method as a function of the missing energy, which equals the neutron's reconstructed energy. One can see the general

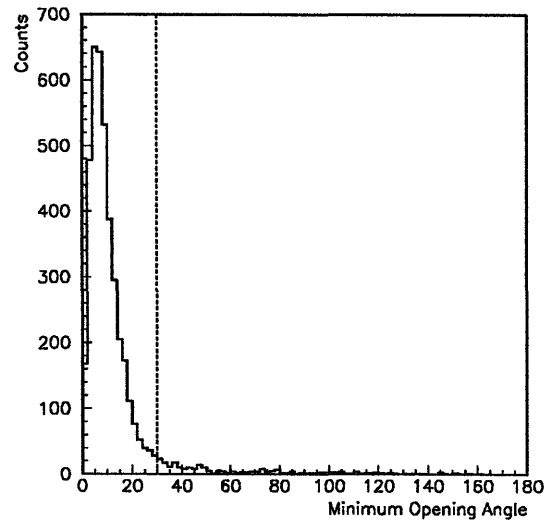


Figure 5-1: The minimum opening angle between the trajectory of a detected neutron and the missing momentum is shown. The data are from the absorption of 239 MeV π^+ 's by ^4He . The dotted line shows the 30° cutoff used when calculating the efficiency.

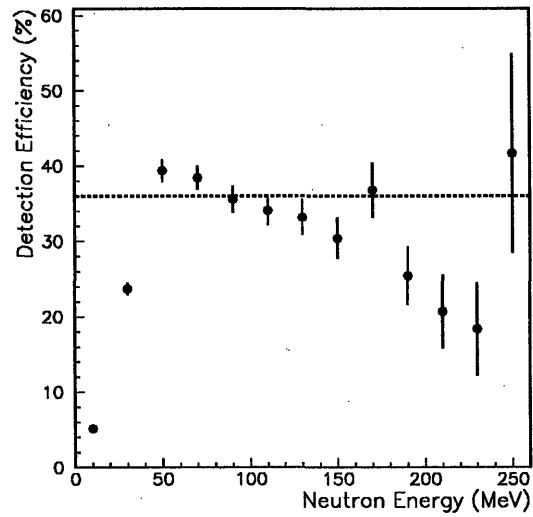


Figure 5-2: The calculated neutron detection efficiency is shown as a function of the neutron's reconstructed kinetic energy. The dotted line shows the value of the efficiency used in the analysis.

features expected in the plot. The one bin peak at 170 MeV has been closely examined for signs of contamination in the data set, but no such indications were found. The error bars are statistical. Of course, when LADS detects a neutron, its energy is unknown. It is possible to estimate its energy from its TOF, but with the short flight paths and thick scintillator blocks in LADS, this method is not particularly accurate. Thus, an attempt will be made to estimate a single value for the neutron detection efficiency, rather than a function of E . If one considers the data from the 50 MeV point and higher in figure 5-2, and takes an average of the efficiencies weighted by the number of neutrons in each bin, the result is $\epsilon_n = 36\%$. Because of the variation of this value with energy, a conservatively large systematic uncertainty of 4% will be applied to this number.

It was mentioned earlier that the neutron detection efficiency is sensitive to the detection threshold for light in the LADS detector. It is thus reasonable to question the effect of the 2.5 MeV minimum light cut used to remove noise that would otherwise be interpreted as neutrons. If this threshold is lowered to 1.5 MeV, the detection efficiency increases to 38%. If the restriction is removed completely, the efficiency only increases by another 0.5%. Therefore, the use of a minimum light requirement does decrease the detection efficiency, but not in a significant manner.

The question of the efficiency's variation with θ is still relevant. Figure 5-3 shows the detection efficiency as a function of θ for events with a missing energy greater than 40 MeV. The expected variation of the detection efficiency with the plastic thickness is visible. However, the variations with angle are small enough to remain consistent with $36\% \pm 4\%$.

5.1.4 Correcting for the Neutron Efficiency

Once the number of detected neutrons and the neutron detection efficiency are known, the procedure for determining the actual number of neutrons in the final state is straightforward. For any particular charge multiplicity (*e.g.* 1C), one starts with the maximum possible number of neutrons in the final state, N_{\max} . Then the cross section is determined from:

$$\sigma_{1CN_{\max}N} = \left(\frac{1}{\epsilon_n}\right)^{N_{\max}} \sigma_{1CN_{\max}N}^{\text{detected}}$$

The contribution from this final state to the cross sections for detecting $1, 2, \dots, N_{\max}$ neutrons is then calculated, and these values subtracted from the corresponding detected cross sections. The process is then repeated for $N_{\max}-1, N_{\max}-2, \dots, 1$ neutrons.

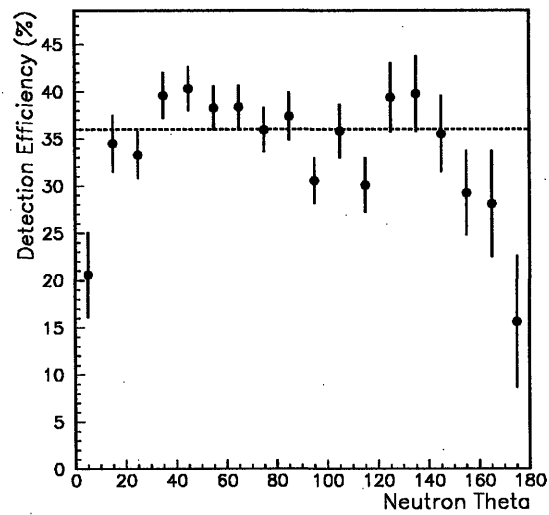


Figure 5-3: The calculated neutron detection efficiency is shown as a function of the neutron's theta, for neutrons with a kinetic energy greater than 40 MeV. The dotted line shows the value of the efficiency used in the analysis.

Neutron Efficiency Corrections						
	(a)	(b)	(c)	(d)	(e)	(f)
0N	163.5	99.3	89.4	107.7	100.0	98.6
1N	43.5	81.8	85.1	78.4	79.2	84.5
2N	4.6	25.7	30.2	22.0	29.8	21.6
3N	0.2	4.9	7.0	3.6	2.8	7.1

Table 5.3: An illustration of the correction for the neutron detection efficiency. The data are from the absorption of 162 MeV π^+ 's on Ar with two charged particles detected in the final state. Column (a) shows the detected multiplicities, and column (b) has been corrected for the neutron detection efficiency as described in the text. Columns (c) through (f) illustrate the impreciseness of this procedure. (c) and (d) have been calculated with $\epsilon_n = \epsilon_n \pm \sigma$, or 32% and 40%. (e) and (f) show the effect of changing the detected 3N cross section by ± 0.1 mb.

In the above description, the only unknown quantity is the maximum possible number of neutrons in the final state. For ${}^3\text{He}$, there are no final state neutrons, so any detected strength with neutrons has been reassigned to the zero neutron cross section. For ${}^4\text{He}$, there can be only one neutron, so this was used as the maximum number, and any strength at higher multiplicities was moved down. For N and Ar, in no cases were the cross sections for more than three detected neutrons statistically inconsistent with zero. For this reason, three is taken as the maximum number for this analysis.

Although this process is straightforward, it also proves to be somewhat imprecise because of the large effects caused by small changes in the detected cross sections for large numbers of neutrons. The procedure and its inaccuracies are illustrated in table 5.3. The data are from the absorption of 162 MeV π^+ 's on Ar with two charged particles detected in the final state.

The results from this analysis are shown in tables 5.4 and 5.5.

5.2 Detected Deuterons

The final question that needs to be answered in the multiplicity analysis is the strength of the absorption reaction with deuterons in the final state. This is an easy question to answer given the analysis machinery already discussed.

⁴ He			
	118 MeV	162 MeV	239 MeV
1C0N	0.8	1.3	-2.2
1C1N	3.2	2.0	1.2
2C0N	31.7	27.8	11.1
2C1N	6.5	7.0	4.6
3C0N	5.1	6.8	4.2
3C1N	2.1	3.0	2.7

Table 5.4: The neutron multiplicities in millibarns, after the correction for the neutron detection efficiency has been applied.

The PID curves used to identify a deuteron are shown in figures 3-4, 3-5, and 3-6. Deuterons have to satisfy the other requirements that have been described for charged particles as well. One additional restriction was applied. Deuterons tend to be rather low energy particles. The maximum possible energy a deuteron can have following three or four nucleon absorption is about 140, 175, or 230 MeV for incident pion energies of 118, 162, and 239 MeV respectively. Thus limitations were placed on the maximum deuteron energy 10 MeV higher than these values. If a particle was identified as a deuteron, but had a higher energy, the assumption was that a mistaken identification had occurred, and the particle was relabeled as a proton.

The analysis to determine the final state multiplicities was same as that described for the charged particle multiplicities. It was found that the cross sections for detecting two deuterons in the final state were negligible ($\leq 1\%$ of σ_{abs}), so the deuteron multiplicity was always at most one. The SCX correction was made using the photon detection efficiency calculated from the full analysis. Misidentified pions would usually be mistaken for protons, not deuterons, so no pion contamination correction was made. The results, before corrections for protons being mistaken for deuterons (and visa-versa) have been made, appear in table 5.6.

To correct for contamination from protons being mistakenly identified as deuterons, the fact was used that there are no deuterons in the final state following the absorption of a π^+ on ^3He . Any contamination will have the same number of detected charged particles, and so should be a function of the cross section for the same charge multiplicity. Attempting to zero the number of deuterons for the 1C, 2C, and 3C channels in ^3He at the three pion energies, it was found that the best solution was to subtract 2.7% of the corresponding cross section. That is,

$$\sigma_{\text{XCYN}}^{\text{d}} = \sigma_{\text{XCYN}}^{\text{d,detected}} - 0.027 \times \sigma_{\text{XCYN}}.$$

N			
	118 MeV	162 MeV	239 MeV
1C0N	15.3	9.4	0.3
1C1N	21.4	14.1	7.7
1C2N	4.0	2.7	2.6
1C3N	0.2	1.0	0.6
2C0N	79.4	61.5	28.8
2C1N	31.5	31.5	21.5
2C2N	3.5	5.2	5.7
2C3N	0.4	0.5	0.9
3C0N	18.0	22.6	17.3
3C1N	5.8	9.9	11.7
3C2N	0.5	1.2	2.7
3C3N	0.0	0.1	0.2
4C0N	1.2	2.5	3.6
4C1N	0.2	0.9	2.3
4C2N	0.0	0.1	0.3
4C3N	0.0	0.0	0.0
Ar			
	118 MeV	162 MeV	239 MeV
1C0N	39.7	19.7	-1.0
1C1N	72.9	45.5	26.7
1C2N	18.9	27.4	17.0
1C3N	3.3	3.6	8.0
2C0N	125.7	99.3	50.0
2C1N	79.1	81.8	63.8
2C2N	15.3	25.7	29.2
2C3N	2.4	4.9	9.2
3C0N	23.2	31.1	28.5
3C1N	9.7	18.3	28.6
3C2N	1.6	4.4	8.8
3C3N	0.0	0.3	2.1
4C0N	1.1	2.5	5.2
4C1N	0.2	1.3	4.1
4C2N	0.1	0.1	0.9
4C3N	0.0	0.0	0.1

Table 5.5: The neutron multiplicities in millibarns, after the correction for the neutron detection efficiency has been applied.

${}^3\text{He}$			
	118 MeV	162 MeV	239 MeV
1d0p	-0.1	0.0	0.1
1d1p	0.4	0.5	0.3
1d2p	0.1	0.2	0.1
Total	0.4	0.7	0.5

${}^4\text{He}$			
	118 MeV	162 MeV	239 MeV
1d0p	0.2	0.2	0.0
1d1p	2.5	2.0	0.9
1d2p	2.7	3.2	1.6
Total	5.4	5.5	2.6

N			
	118 MeV	162 MeV	239 MeV
1d0p	1.4	1.1	0.5
1d1p	12.4	10.0	5.5
1d2p	6.6	8.8	7.6
1d3p	0.6	1.6	2.7
Total	21.0	21.6	16.6

Ar			
	118 MeV	162 MeV	239 MeV
1d0p	4.7	3.5	3.3
1d1p	28.8	26.9	20.2
1d2p	8.6	13.7	17.3
1d3p	0.5	1.4	4.0
Total	42.6	45.6	45.0

Table 5.6: Multiplicities in millibarns of final states including a deuteron, before corrections for mistaken PID have been applied.

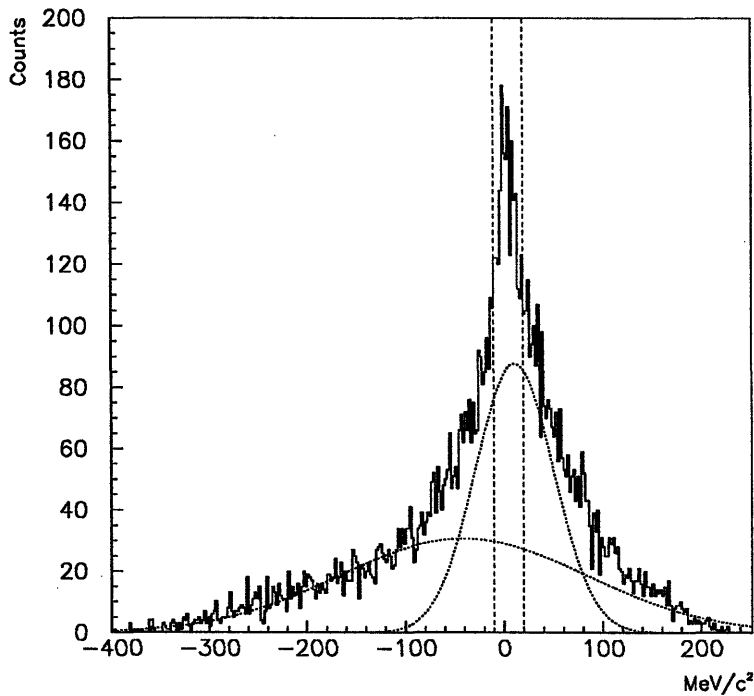


Figure 5-4: The missing mass calculated from the two known protons for a set of *ppd* events with some *pppn* contamination. The curves and lines are described in the text.

The method for determining the fraction of deuterons which were mistakenly identified as protons was similar to the calculation of the reaction correction for protons described in section 4.5. The first step was to select a set of events, each of which includes a deuteron, without using its plastic energy or timing information. Data from the interaction of 162 MeV pions with ^4He were used. Events were chosen which had three detected charged particles, and one of these was chosen at random as the test particle. The PID of the other two was checked to ensure that they were protons, and then the MWPC information was used to reconstruct the energy of the system assuming a *ppd* final state. This reconstructed energy was cut in the vicinity of the known total energy of the system in order to select *ppd* events.

Unfortunately, there is a substantial background from *pppn* final states in this set of events. In order to estimate its magnitude, the two known protons were used to calculate the missing mass. The resulting spectrum appears in figure 5-4. The two dashed lines show the cuts applied

${}^4\text{He}$			
	118 MeV	162 MeV	239 MeV
1d0p	0.1	0.1	0.0
1d1p	1.8	1.3	0.6
1d2p	3.0	3.6	1.7
Total	4.9	5.1	2.4
N			
	118 MeV	162 MeV	239 MeV
1d0p	0.4	0.4	0.2
1d1p	11.3	8.9	4.8
1d2p	7.2	9.5	8.2
1d3p	0.7	1.8	3.1
Total	19.5	20.8	16.6
Ar			
	118 MeV	162 MeV	239 MeV
1d0p	1.3	1.1	2.3
1d1p	27.6	25.6	19.5
1d2p	9.3	14.8	18.7
1d3p	0.6	1.6	4.5
Total	38.7	43.2	45.2

Table 5.7: The multiplicities (mb) of final states including a deuteron after all corrections described in the text have been applied.

to this spectrum in order to further purify the events. The two curves appearing in the figure are gaussians, the sum of which was fit to the data. The lower one was then used to estimate the $pppn$ background in the selected region, which was about 20% of the events.

In order to determine the correction for deuteron misidentification, the PID of the test particle was finally checked. By comparing the number of times a deuteron was identified to the number of deuterons present, a correction factor of 1.21 was calculated. The results incorporating these corrections appear in table 5.7.

Chapter 6

Discussion and Conclusions

The previous chapters have described the LADS experiment and the methods used in this analysis of the data. Results have also been given for the multiplicities of the various final state particles following the absorption of π^+ on a variety of targets in the energy region of the $\Delta(1232)$ resonance. In this chapter these results will be discussed, with comparisons made with other experiments. In addition, a selection of differential spectra will be examined in an attempt to understand the manner in which the absorption process changes with increasing nucleon number.

6.1 Summary of Acceptance Limitations

Before this discussion is begun, however, it is important to understand exactly what has been measured. The results reported in the multiplicity analysis are all “detected” cross sections, ostensibly of the numbers and types of the particles sharing the pion’s energy. These would correspond to actual cross sections if the detector’s coverage were complete. Because there are some limitations to the coverage, the detected cross sections will be smaller than the actual cross sections, by a factor that varies from case to case. Since the coverage is nearly complete, however, the correspondence between the reported results and the actual cross sections should be quite good.

The limitations to the detector coverage are combinations of restrictions to the solid angular coverage and to the detection threshold. For charged particles, the innate restrictions from the

detector include the energy threshold of between 15 and 20 MeV for protons (about 25% higher for deuterons) and the openings at the beam's entrance and exit windows. These openings are small enough to be ignored within the uncertainties of the quoted results. In addition there are effects from the granularity of the detector. In other words, if a proton hits one of the 28 cylinder sectors in LADS, no other particles can be detected in that sector. For each charged particle in the final state, this effect reduces the geometrical acceptance by about 3%.

Other limitations have been introduced in the software to help in the separation of particle types and in the identification of absorption events. The most important of these is the combination of hits in adjacent sectors into single particles. Because of this combination, each additional particle reduces the effective coverage of the detector by about 10% of 4π steradians. The final two major limitations are the requirement that if only one charged particle is detected, it has over 35 MeV of associated light, and that at least one charged particle be detected with a polar angle greater than about 15° (this corresponds to a reduction in coverage of less than 2% of 4π steradians). These restrictions are discussed in sections 4.1 and 4.3.3. The first helps to limit the contamination from SCX, and the second reduces contamination from elastic pion scattering.

Noise in the detector was minimized by restricting the reduced TOF of particles to a maximum of 7 ns. In the absence of resolution smearing this will not have any effect since 7 ns corresponds to 10 MeV kinetic energy for protons, which is below the detector's threshold. In addition, each particle must have a minimum of 2.5 MeV of associated light, which increases the detector threshold by approximately that amount.

For neutral particles the geometrical limitations are similar to those for charged particles. The requirement that each neutral has an opening angle of over 30° from other particles means that the effective detector coverage for neutrals is reduced by about 12% for each particle in the final state. The energy limitations have less precise effect than for charged particles because of the "soft" threshold for neutron detection arising from the dependence of ϵ_n on the neutron's energy. The 2.5 MeV light limitation causes a general reduction in detection efficiency, although the effect does become more important for lower neutron energies. A more important threshold effect is the 7 ns limitation. Because of the manner in which the detector is calibrated, this corresponds to a threshold of about 20 MeV instead of 10 MeV. The short flightpaths in the LADS detector impair the accuracy of the TOF measurements, making this 20 MeV number quite imprecise.

Now that the major acceptance restrictions have been recalled, the relationship between the detected cross section and the actual cross section can be estimated. First of all, the difference

for the total absorption cross section will be small. This difference would arise if there were only one charged particle in the detector and it had less than 35 MeV of associated light, or had a polar angle of less than 15° . The rest of the energy would have to be carried off by neutrons, by a number of charged particles under the detector threshold, or by particles travelling through the beampipe. Since absorption typically leads to two energetic charged particles in the final state, and in those channels which only have one charged particle it typically has significant energy, none of these occurrences is likely.

The effects of the detector acceptance will be more apparent in the separation of the total absorption cross section into the various multiplicities. A three-charged-particle final state may be identified as two, or a neutral will be missed. The magnitudes of these effects are difficult to determine because their likelihood is directly related to the mechanism responsible for the absorption reaction. For example, one interaction that can occur is soft-FSI. This is a final state interaction that enhances the cross section for small differences in momenta of the final state particles, especially proton-neutron pairs. Small differences in momentum vectors means small opening angles, so the neutron will probably be inside of the 30° cutoff. LADS is not particularly suited to detecting soft-FSI neutrons. This interaction is therefore best studied in kinematically complete final states where the neutron momentum can be reconstructed.

Although it is essentially impossible to determine the acceptance effects exactly, they can be estimated by assuming specific distributions and studying the detector response. For example, following the absorption of a 162 MeV π^+ , a three proton final state distributed like phase space will result in the detection of all three protons 77% of the time, only two 19%, and at least one over 99%. The chance of detecting all three would be 73% if the incident pion energy were 118 MeV, and 81% if it were 239 MeV. Thus, all of the particles are usually detected. When interpreting the results, it is important to realize that the actual cross section will be in the neighborhood of 30% larger for the higher multiplicities, and correspondingly smaller for the lower multiplicities. This fraction will continue to grow with the number of nucleons involved, however, or if the residual nucleus is left in a highly excited state. Of course, the results of any calculations or simulations can be directly compared to the data by simply applying the well-understood detector acceptance to the predictions.

6.2 The Results of the Multiplicity Analysis

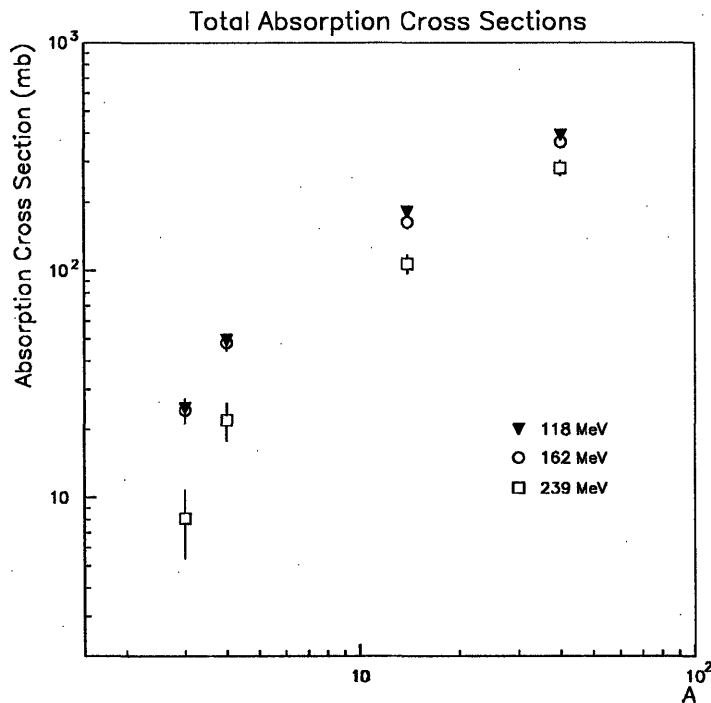


Figure 6-1: The total detected cross sections are shown as a function of A . The triangles are for an incident pion energy of 118 MeV; the circles, 162 MeV; and the squares 239 MeV. Uncertainties are included, but are frequently smaller than the size of the symbol.

The total detected cross sections reported in table 4.3 are graphed as a function of A in figure 6-1. Two things are immediately apparent from this figure. The cross sections at 118 and 162 MeV are approximately equal, with the cross section at 239 MeV being significantly smaller. This behavior was expected and has been seen by many earlier experiments. The second fact is that the cross section asymptotically approaches a power law in A . Fits to the N and Ar data give exponents of 0.73, 0.77, and 0.93 at the three energies.

Of previous experiments that measured absorption total cross sections, the most extensive was that of Ashery *et al.* [1]. Figure 6-2 shows a comparison between the current 162 MeV results and Ashery's 165 MeV results. The exponents of the power law in A are similar (Ashery measured .74), but the current results are 25% smaller than Ashery's if the power law is used to scale the results to the same A . In their experiment, measurements were made of the total reaction cross section and the pion scattering cross section. The absorption cross section was

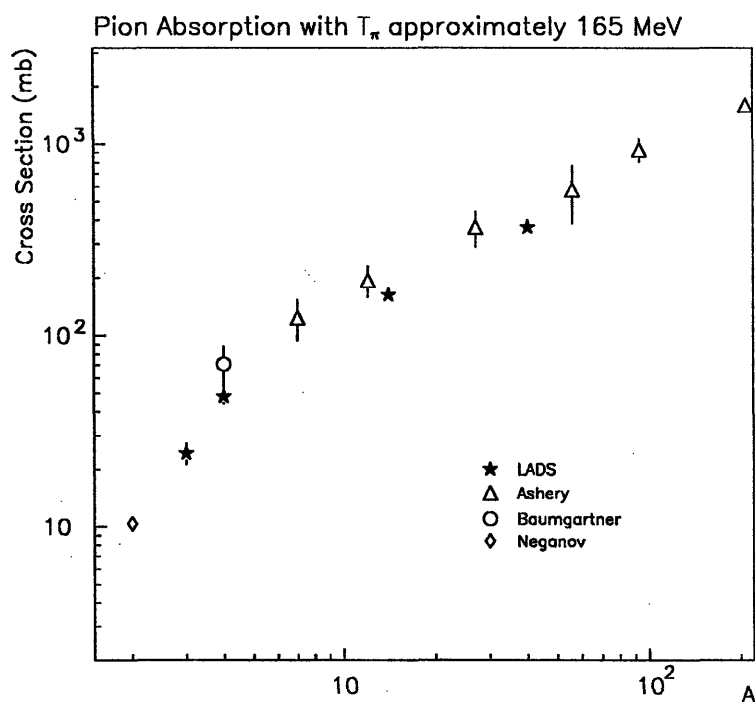


Figure 6-2: A comparison between the total absorption cross sections from this work and those from previous experiments in the vicinity of 165 MeV. The stars show the current results, the diamond is from Neganov and Parfenov [11], the circle is from Baumgartner *et al.* [12], and the triangles are from Ashery *et al.* [1].

calculated by taking the difference, and then subtracting an estimate of the SCX cross section. In this last step significant uncertainties arise. The most likely explanation of the difference, assuming no experimental errors, is that the estimated SCX cross section was significantly low.

Also shown in figure 6-2 is a measurement on ^4He at 170 MeV by Baumgartner *et al.* [12]. The difference in measured values is even more striking here, as Baumgartner's value of 70.9 mb is 50% larger than the current result. As discussed in chapter 1, the jump in the absorption cross section between ^2H and ^4He created much furor in the search for new absorption mechanisms. It now appears that the transition between the power law description of the absorption cross section and the value on ^2H has a much smoother development than previously believed. The lack of a sharp transition indicates that the onset of any possible new mechanisms is a more gradual process. The current result at 118 MeV on ^4He of 49.5 ± 3.1 is directly comparable to a measurement by Steinacher *et al.* [78]. Their value of 52.7 ± 9.0 is in good agreement.

Of the above experiments, Ashery and Baumgartner depended on subtractions of estimated SCX contributions. Measurements of the SCX cross sections made since the absorption experiments were performed [92, 93] have shown that the values used in the calculation of the absorption cross sections were in fact underestimates. If these more recent results are substituted, the measured absorption cross sections drop by almost 10%, bringing their results into better agreement with LADS's.

Figure 6-3 shows the total absorption cross section again, but as a function of the incident pion energy. The curves on this figure represent the absorption cross section on deuterium scaled by factors of 2.2, 4.3, 15, and 34. These factors were chosen to provide good fits to the 118 and 162 MeV points. It is apparent that for the He isotopes, the 239 MeV point lies on the curve; however for the N and Ar, the 239 MeV point is significantly higher than the curve. This fact is consistent with a model in which absorption is dominated by Δ -formation, since in nuclei with higher A the pion is likely to lose more energy to other processes before being absorbed. If it starts above the Δ -resonance, then it can interact multiple times and not fall below the peak of the absorption cross section.

Figure 6-4 shows the charged particle multiplicities from table 4.3. Negative values have been suppressed. In all cases the reported negative values were consistent with zero within the uncertainties. In examining the shapes one notes that the relative strength of the 1C channel is rising with A, and decreasing with energy. A major cause of the energy dependence is likely to be the threshold of the LADS detector. As more energy becomes available, the average energy

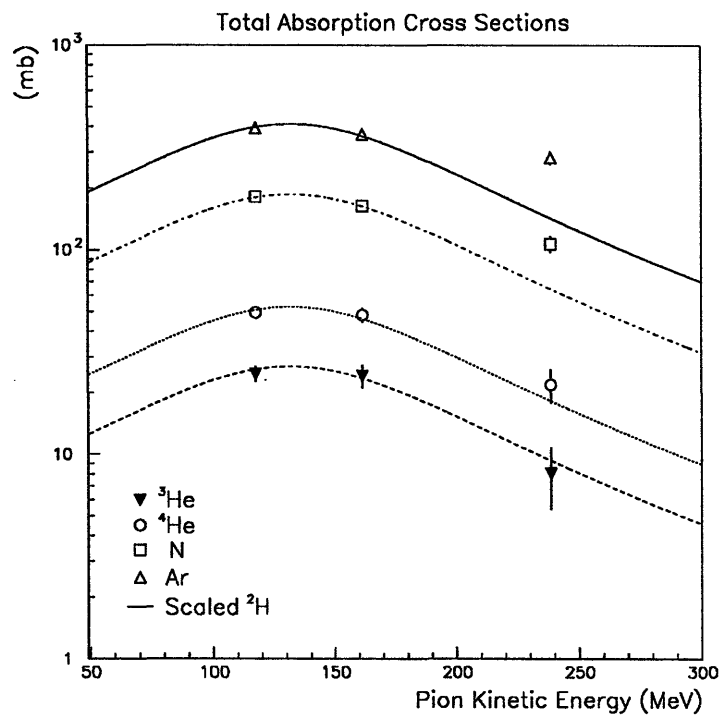


Figure 6-3: The total absorption cross sections are shown as a function of the incident π^+ energy. The solid triangles are for ${}^3\text{He}$, the circles for ${}^4\text{He}$, the squares for N, and the open triangles for Ar. The curves are a parameterization of the ${}^2\text{H}$ cross section [21].

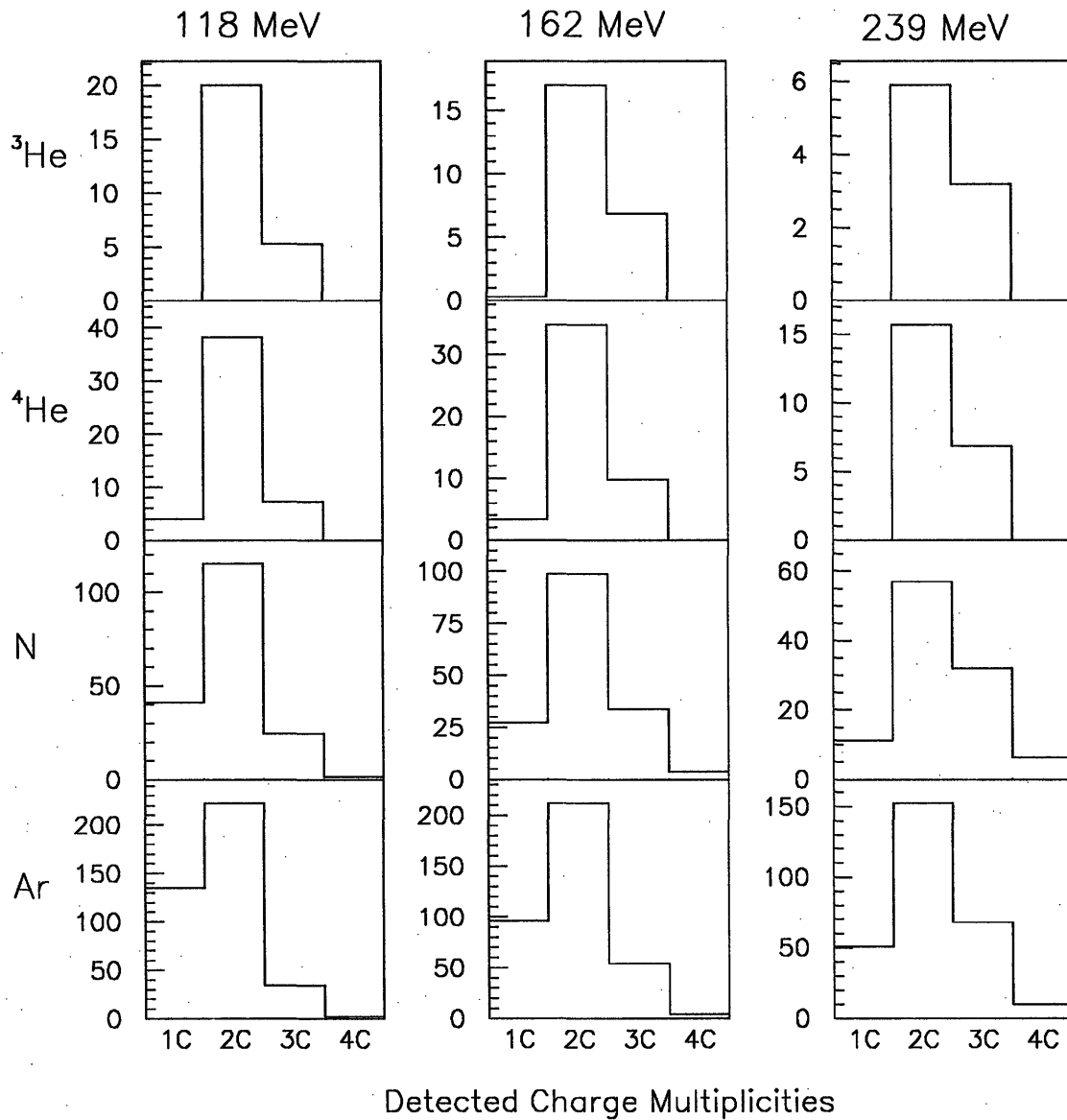


Figure 6-4: The detected charge multiplicities following the absorption of π^+ are shown in millibarns.

of the final state particles increases and more are likely to be over threshold. The dependence of the 1C cross section on A arises from a combination of the energy threshold and the fact that new absorption channels are opening up. On ${}^3\text{He}$ absorption leads to three protons in the final state. Thus, there must be at least two energetic charged particles. In ${}^4\text{He}$, it is possible to have absorption on an nn pair, leading to only one energetic charged particle in the final state. However, there are three $T=0$ pn pairs in ${}^4\text{He}$ and only one nn pair. As shown by Backenstoss *et al.* [15, 69], absorption on a $T=0$ pair is several times more likely than absorption on a $T=1$ pair. In ${}^4\text{He}$ the strength of the 1C channel is thus quite small. As A increases, the numbers of nn pairs begins to approach the number of pn pairs, which will result in increasing strength with only one energetic charged particle. In addition, $Z \neq N$ for Ar, and the possibility of different density distributions for neutrons and protons arises. The relatively high neutron density could increase the likelihood of absorption mechanisms involving only neutrons. This is unlikely to be a significant effect on Ar, however, as this nucleus is still quite light.

The experiments closest to LADS in nature are those using the BGO ball at LAMPF. This large solid angle detector has been used to study π^+ reactions for a large range of incident pion energies and target masses [84, 85, 86]. Unfortunately, the coverage is only about 77% of 4π , which limits the ability to clearly identify absorption events. Thus, its missing energy spectra are contaminated with events in which absorption did not occur, leading to large strengths at high missing energies, and making comparisons with the current results difficult. The analysis of the BGO data does make attempts to correct for these effects when quoting cross sections for various multiplicities. Still, difficult to estimate extrapolations in the vicinity of factors of 3 to 5 are needed to correct their raw data. The best point for comparison to the current experiment is a 150 MeV measurement on ${}^{12}\text{C}$ [84].

In order to compare the BGO results to the current N results, they need to be scaled up by $(14/12)^{2/3}$, and down by .9 (the ratio between absorption on ${}^2\text{H}$ at 162 and 150 MeV), which leave them unchanged. Their 2p cross section of 110 mb can include additional deuterons or single neutrons, but events with two or more detected neutrons are vetoed. Constructing the approximately equivalent result from the tables in chapters 4 and 5 gives 94 mb, which agrees within 20%. A more significant difference is found in the 3p cross section. Their result of 14 mb should be compared to 24.8 mb, which is almost a factor of 2 different. The comparison between the 2p cross sections above implies that some of the 3p strength is being identified as 2p. It is difficult to determine possible reasons for this misidentification from the description given in their papers. Finally, it should be mentioned that the cross section for detecting an energetic deuteron is also different by about a factor of two.

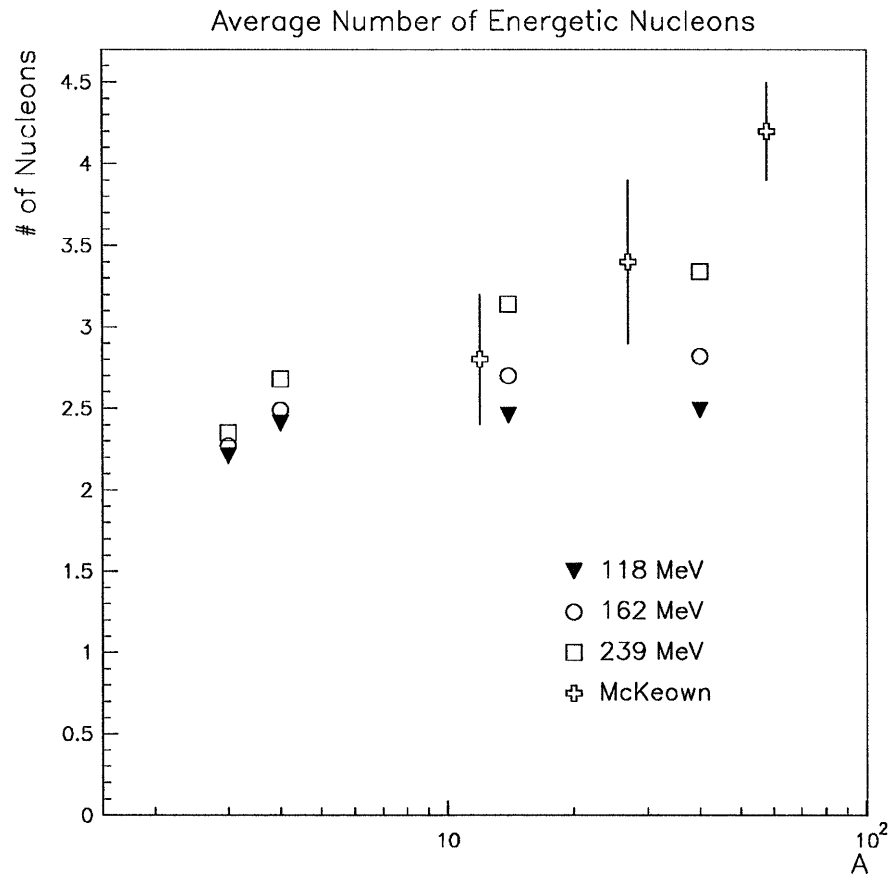


Figure 6-5: The average number of final state energetic nucleons are shown as a function of A.

Finally, figure 6-5 shows the average number of nucleons detected for each combination of target and incident pion energy. The results include corrections for the neutron detection efficiency. For ${}^3\text{He}$ one can see that the average number is approximately the same for each energy. At 118 MeV, this number stays almost constant, while at 239 MeV it is increasing. Thus, as A increases, the difference between the values increases. This trend is consistent with the above explanation of the strength of the absorption cross section at 239 MeV on N and Ar. As A increases, so does the likelihood of various initial state interactions, and thus the number of energetic final state nucleons increases as well. For the lower incident pion energies, any ISI would move the pion far off the resonance peak, and thus the larger A does not have a large effect on the average number of nucleons. Note that these explanations assume a significant ISI contribution and little hard-FSI contribution, since FSI would lead to an increasing average nucleon number at any pion energy.

Previously, the best knowledge of the number of nucleons participating in the absorption reaction for $A > 4$ came from the results of the McKeown *et al.* [10] experiment described in section 1.4. In this singles experiment, proton energy spectra were measured, and a rapidity analysis was used to extract the number of participating nucleons. The reported results, shown in figure 6-5 for comparison, were averages over incident π^+ energies of 100, 160, and 220 MeV. The McKeown results are in good agreement with the current ones for low A , but are rising at a more rapid rate, and clearly disagree for high A . This disagreement is not surprising since the rapidity analysis used by McKeown will tend to overestimate the number of participating nucleons. The probability of an event being included in their data depends on whether a proton is detected, and thus increases with the number of final state protons. Therefore, events with more protons will be weighted more strongly when calculating the average. This effect also could account for the difference between McKeown's π^+ and π^- results in figure 1-13.

6.3 Differential Investigations

The bulk of this thesis has focused on magnitudes of cross sections in a quantitative analysis. This section will be the exception. It contains differential cross sections in an attempt to gain a qualitative understanding of the absorption reaction and the manner in which it changes with increasing A . Some of the figures will lead to clear conclusions, while others will not.

The differential spectra presented are all corrected for SCX contamination and have the empty background subtracted. The events were chosen as described in chapter 4, with the

additional constraint that all charged detected particles have MWPC information. This means that at least one charged particle has to have hits in both the inner and the outer chamber in order to form a vertex, and each charged particle has to have at least one hit. The events are corrected for the MWPC's efficiency, but those final states which have no charged particles passing through both chambers are necessarily missing. The major difference between the events used in this section and the MWPC events from prior chapters is that it was not required that a charged particle have over 35 MeV of light if it was the only one detected. The effects of the contamination in this region will be clear.

Reaction corrections are performed in the manner described in section 4.5. This means that the effects of mistaken PID are accounted for. The fact that actual reactions will move strength around in spectra that depend on the measured energy of particles is not corrected. Also, there are no pion contamination corrections, but their effect would be small.

6.3.1 Total Detected Energy

Figure 6-6 shows the sum of the energies of all charged particles detected for each combination of target and energy. The shapes of the spectra are not particularly dependent on the pion energy, but show a clear trend with increasing A . ${}^3\text{He}$ has only charged particles in the final state, so the amount of missing energy is limited to about 20 MeV, or the maximum proton threshold. For larger values of the missing energy some strength is apparent, but it has the characteristic features of a reaction tail. There can be an energetic neutron following absorption on ${}^4\text{He}$, and there is correspondingly more strength in the tail, particularly for the two higher energies. That the processes leading to an energetic neutron are not particularly strong is apparent from the relative prominence of the peak with zero missing energy. By the time $A=14$, the situation has almost reversed. Most of the strength has significant missing energy, although signs of a peak with zero missing energy are still apparent, at least at 118 and 162 MeV. This trend is continued in Ar, for which the strength at zero missing energy is a minor component of the cross section. There are two possible conclusions - either neutrons always take part in the reaction, or the energy is spread among so many particles that significant numbers lie below the detector threshold.

The problems that arose when there was only one charged particle detected with under 50 MeV of energy are apparent in this figure with the negative cross section on ${}^3\text{He}$ at 239 MeV. These problems are significantly clearer in figure 6-7, repeated from chapter 4, which shows the energy of a charged particle when only one charged particle is detected. The most noticeable

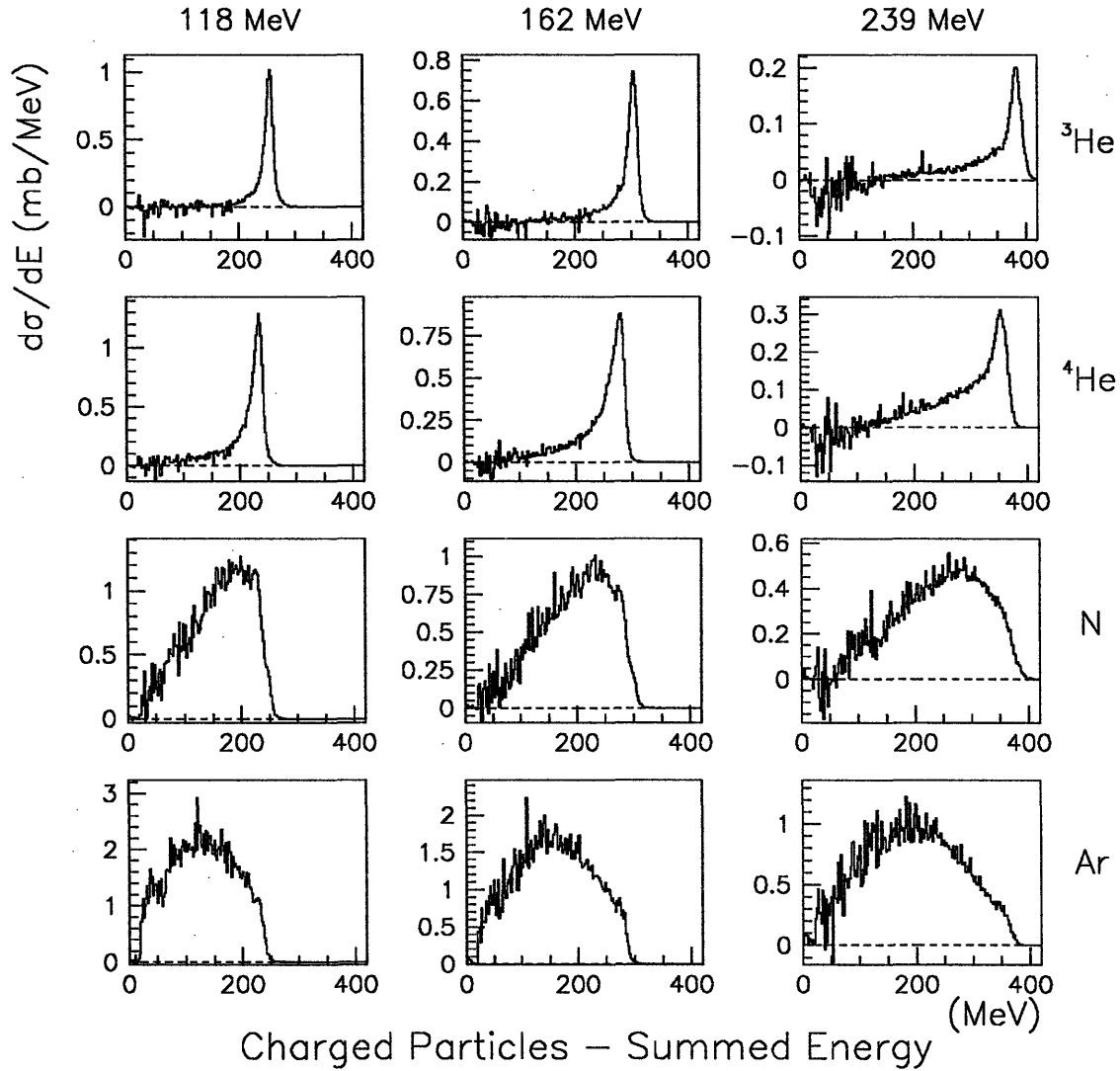


Figure 6-6: The summed energies of all charged particles.

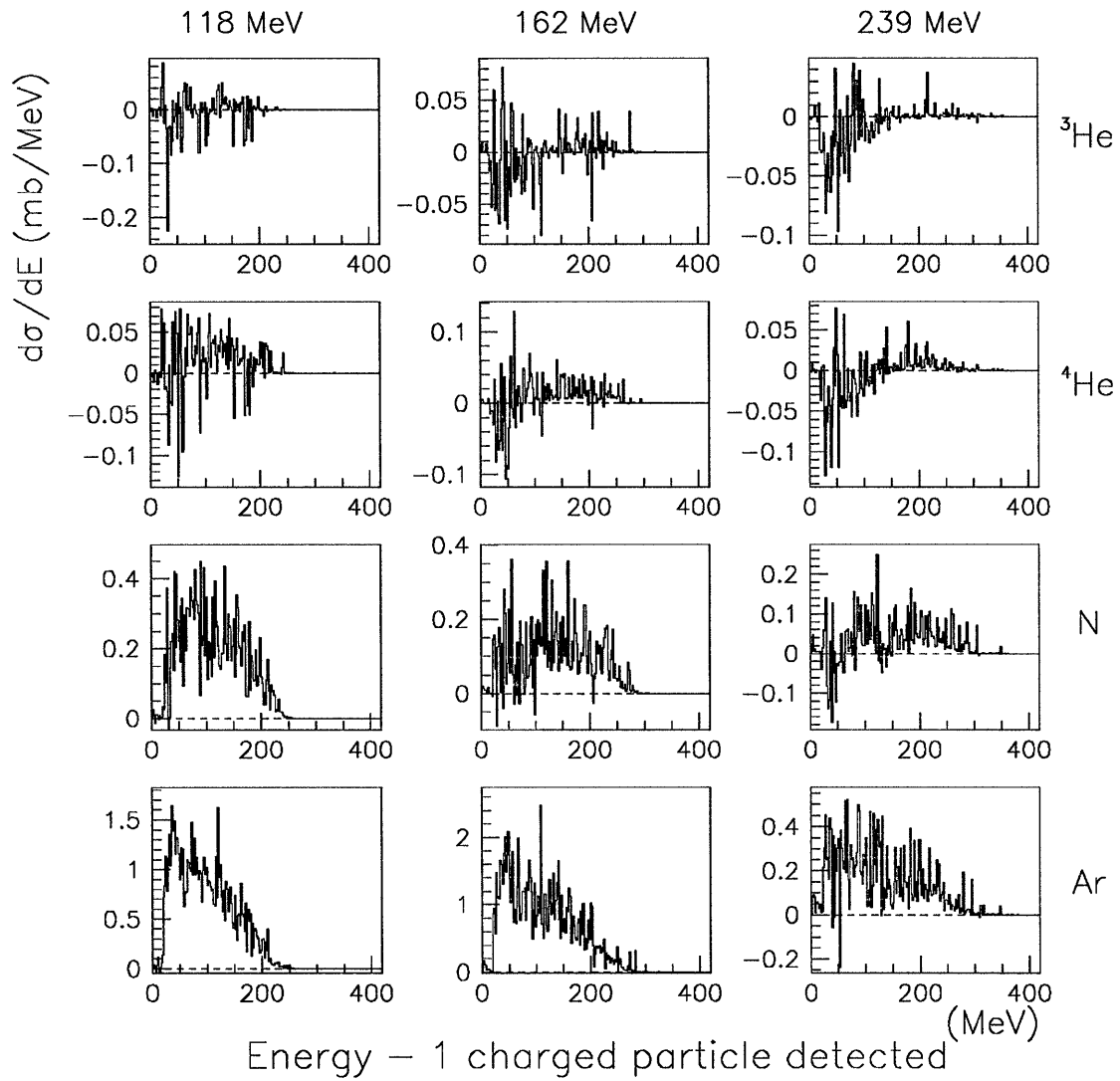


Figure 6-7: The energy of a charged particle when only one charged particle was detected.

features are the problems in the low energy region. Both the negative cross section in ${}^3\text{He}$ at 240 MeV and the peaks in this energy region that are visible on N and Ar are due to problems with the SCX contamination correction. Also visible is the trend from zero strength above 100 MeV to significant strength as A increases. This strength is indicative of the onset of absorption on groups of neutrons. Also interesting is the complete lack of a signature for the absorption on a single neutron in the nucleus. This reaction, which is possible in a nucleus with a high Fermi-momentum, was possibly identified in an early experiment by Witten *et al.* [57].

Absorption on a $T=0$ pn pair has long been thought to be the dominant absorption process in nuclei. When this reaction occurs, one expects two protons to carry away the bulk of the π^+ 's energy. It is, of course, possible for two nucleon absorption to be either preceded or followed by an interaction which results in more than two particles sharing the energy. However, one would still expect to see a signature for this reaction proceeding undisturbed, with the rest of the nucleus acting as a spectator. Figure 6-8 shows the summed energy when two charged particles are detected. The ${}^3\text{He}$ data show a clean peak due to two nucleon absorption. This peak is also present in the ${}^4\text{He}$ data, with a tail that indicates the presence of a small amount of ppn final states. In the N data at the two lower energies, a clear peak is present that is due to two nucleon absorption, but the bulk of the strength has a significant missing energy. In the high energy N data and the Ar data, a shoulder is apparent, but is completely dominated by events with large missing energy.

Figure 6-9 shows the same information when there are three detected charged particles. It also shows the same basic signatures and trends, but the signature is already almost absent by $A=14$. The conclusion is similar to that drawn above. The He isotopes show clean indications of various reaction mechanisms which appear to be well separated. The N and Ar data show some small signs of similar mechanisms, but the bulk of the data have large missing energies. Apparently the dominant final states either include the presence of energetic neutrons, or the nucleus undergoes some form of breakup in which there are many final state particles among which the pion's energy is spread.

A quantity that shares many characteristics with the summed energy is the missing momentum. Figure 6-10 shows the missing momentum calculated from the momenta of all detected charged particles. The ${}^3\text{He}$ spectra have several interesting features. First, there is the sharp peak at zero missing momentum. This corresponds to the events in which all three protons are detected. The curves rise to a peak at about 100 MeV/c and then fall quickly to zero at 200 MeV/c. The lack of strength above 200 MeV/c is due to the fact that above this momentum all final state particles are detected, so the missing momentum is zero. Between 0 and 200 MeV/c

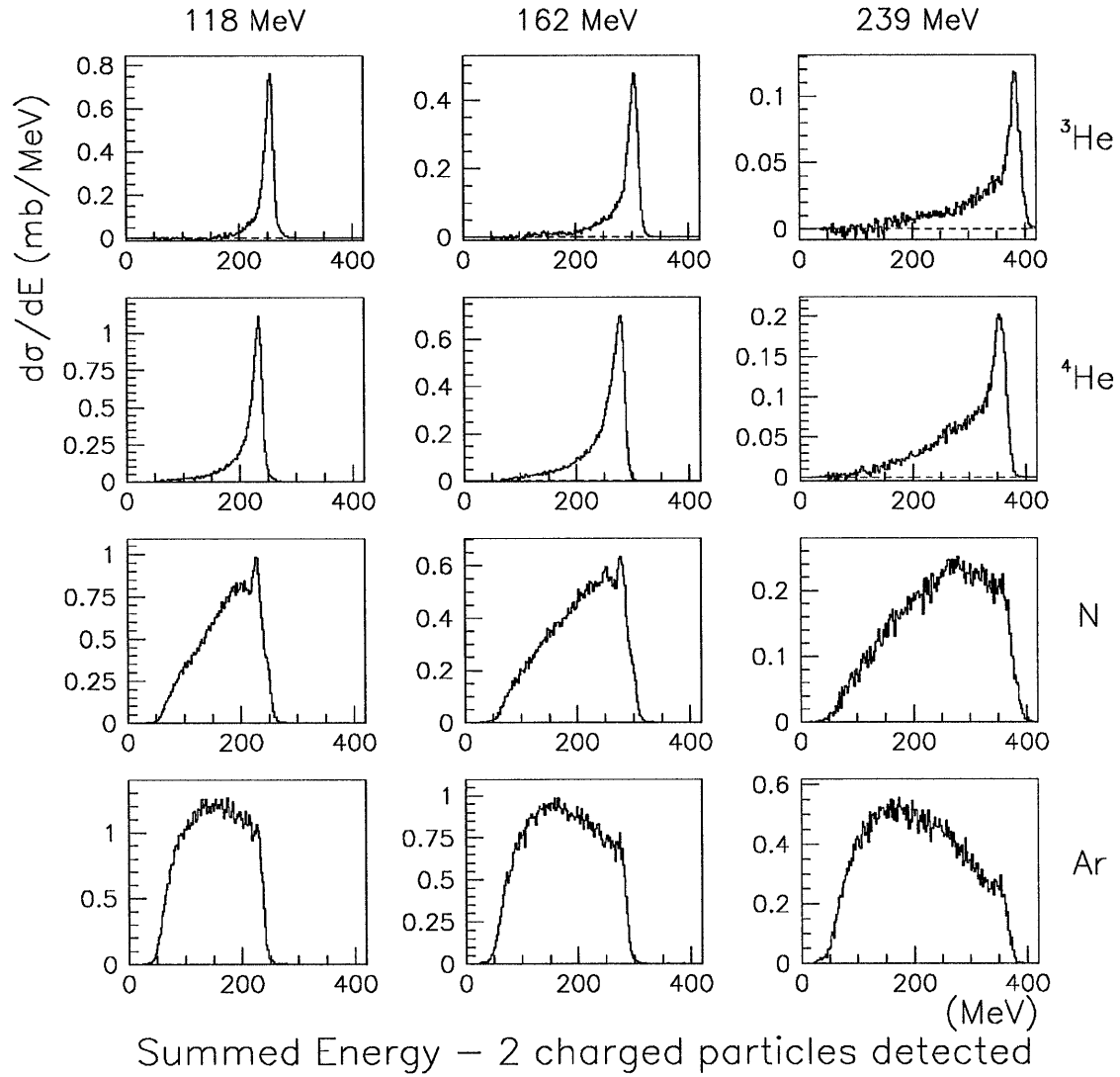


Figure 6-8: The summed energies of two charged particles when no other charged particles were detected.

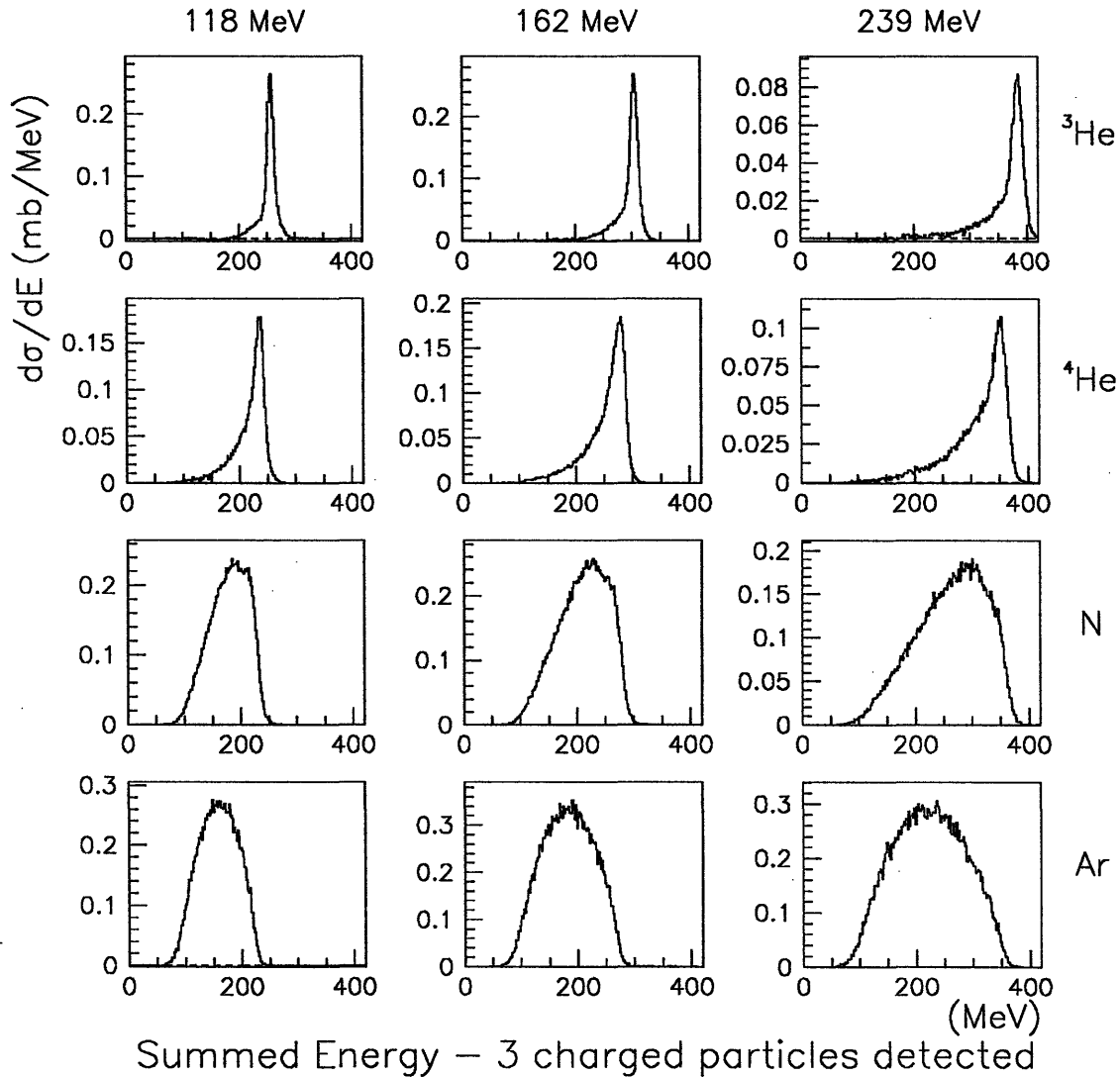


Figure 6-9: The summed energies of three charged particles when no other charged particles were detected.

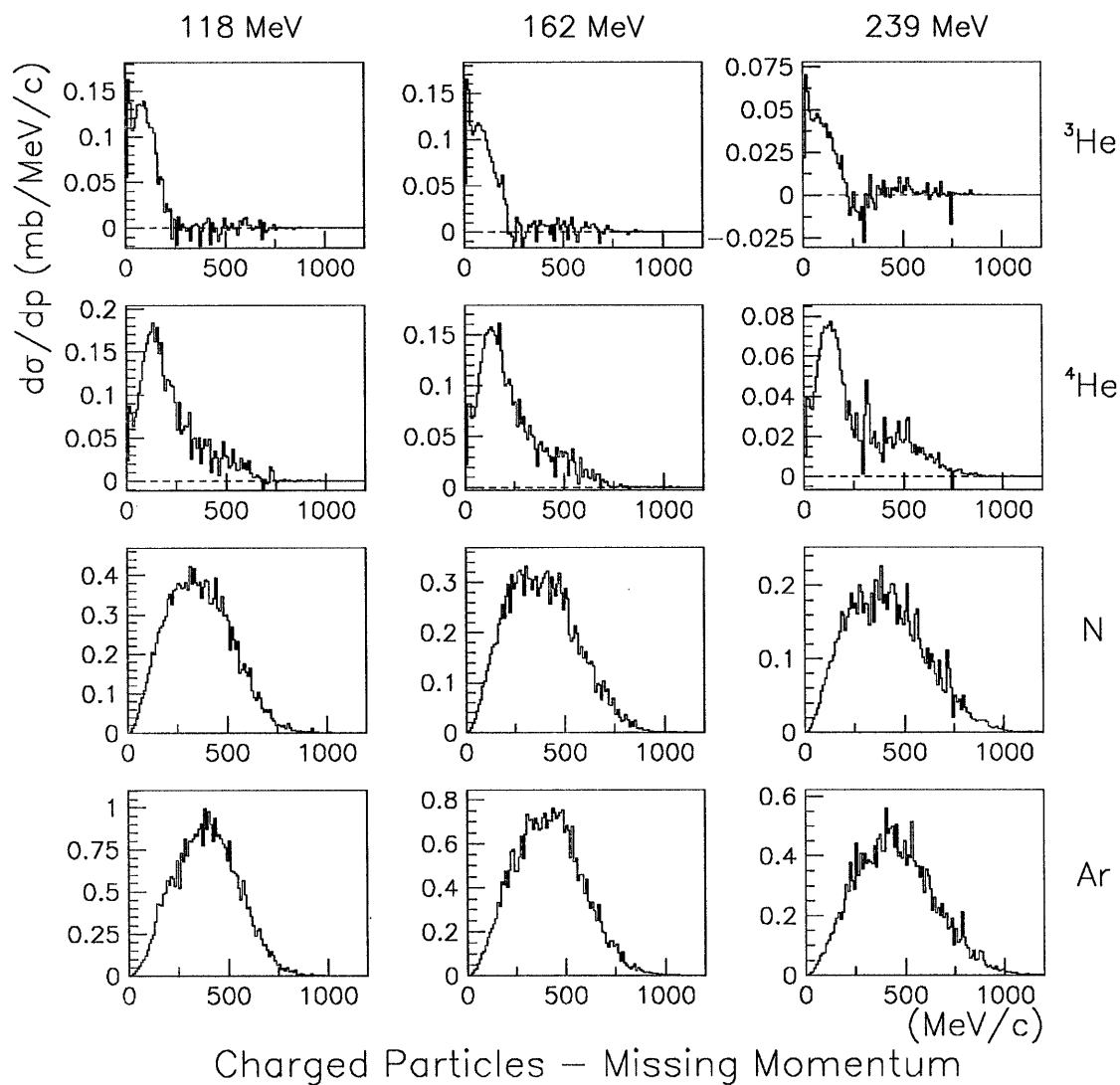


Figure 6-10: The missing momentum calculated from all of the detected charged particles.

the spectra show the Fermi-distribution in ${}^3\text{He}$, and these events correspond to two nucleon absorption with the third proton acting as a spectator. Similar behavior is seen in ${}^4\text{He}$, with the addition of a broad bump at about 500 MeV/c corresponding to a $pppn$ final state with an energetic neutron. By $A=14$ the curves are essentially featureless, due to the mixing of a variety of channels and the effects of Fermi-smearing. Distinguishing features of the reaction are not apparent.

6.3.2 The Search for ISI

The two simple processes that would explain the pion's energy being shared among more than two nucleons while still limiting the absorption process to two nucleons are initial state interactions and final state interactions. Signatures from these interactions are therefore of much interest.

In an initial state interaction, the π^+ quasi-elastically scatters from one nucleon before being absorbed by two others. Therefore, one final state nucleon should have the kinematic signatures associated with quasi-free elastic scattering, while two others will have apparently participated in absorption. The pion's energy and momenta in the intermediate state will be varied, which will obfuscate many otherwise clear signatures. In this section, two separate kinematic signatures will be examined. The first involves the scattered nucleon, looking for the momentum-theta correlations appropriate for quasi-elastic scattering. The second involves the absorbing nucleons, with an attempt to calculate the mass of the absorbed particle. Since the π^+ -p scattering cross section is significantly larger than the π^+ -n scattering cross section, and absorption on a pn pair is more likely than absorption on an nn pair, the bulk of the ISI cross section should have three energetic protons in the final state. LADS's energy and trajectory information is much better for protons than for neutrons, so this search will concentrate on the $3p$ final states.

Figures 6-11, 6-12, and 6-13 show the momentum of a proton as a function of its polar angle, θ . The data are restricted to events with three protons in the final state, each with over 30 MeV. The additional energy cut is included to reduce the contamination from two-nucleon absorption, with a third proton above the detector threshold as a result of its initial momentum (Fermi) or evaporation. With this cut in place, the expected contamination to the ${}^3\text{He}$ data at 240 MeV is on the order of 10%. This is the worst of the three ${}^3\text{He}$ cases.

The features are clearest in the 239 MeV data. The curves drawn on the plots show the relationship between momentum and angle for π -p elastic scattering. The presence of a clear

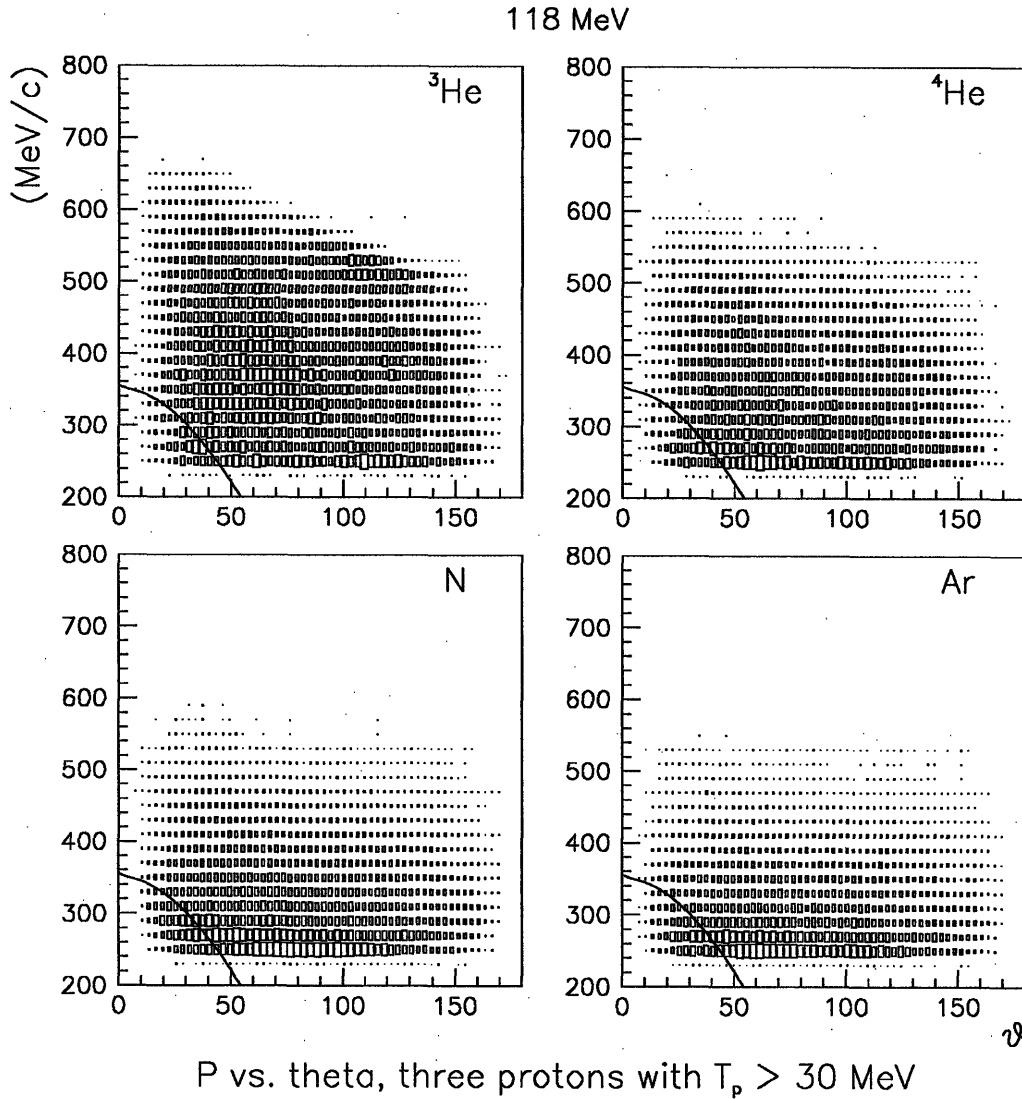


Figure 6-11: The relationship between the momenta and polar angles of the protons for events in which three protons are detected, with each $T_p > 30$ MeV. The incident π^+ energy is 118 MeV.

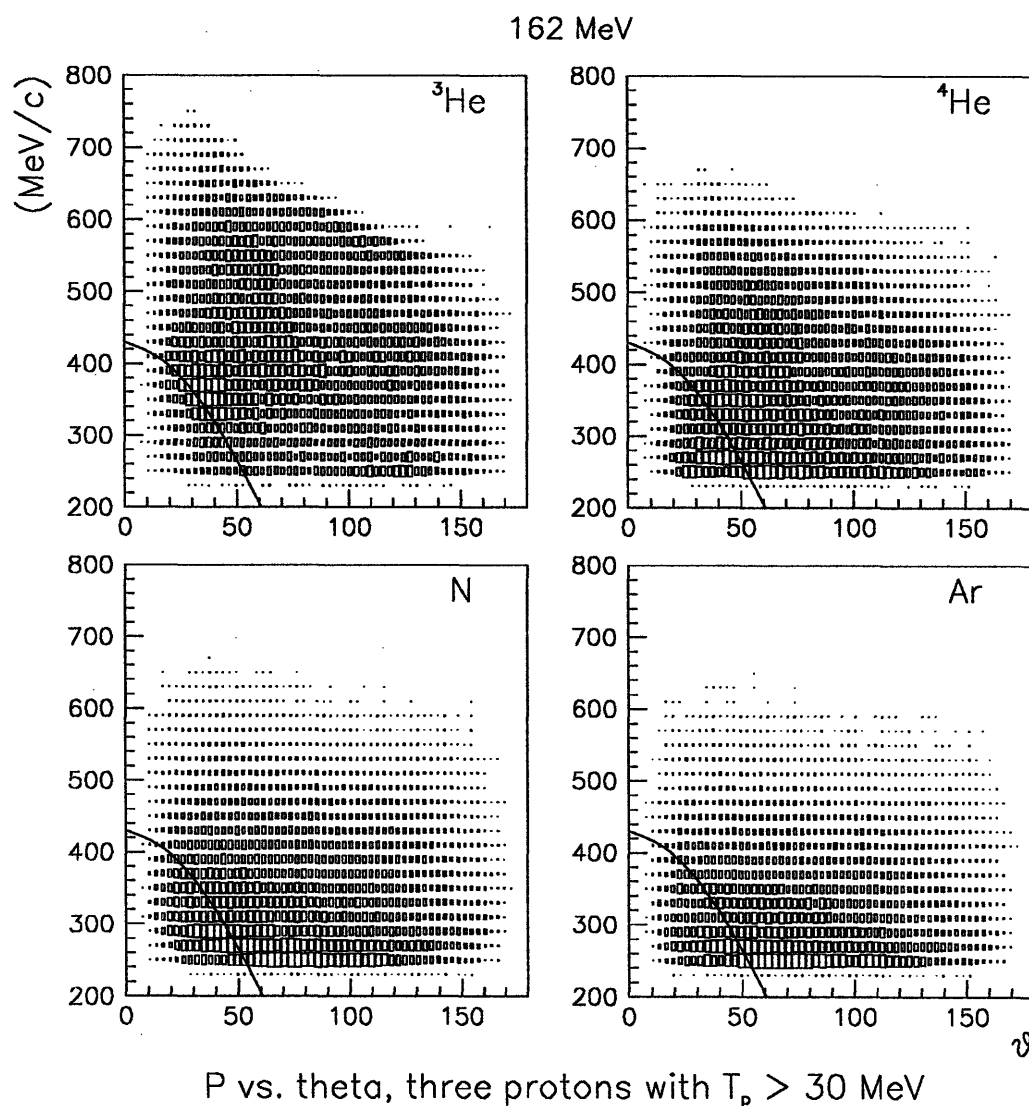


Figure 6-12: The relationship between the momenta and polar angles of the protons for events in which three protons are detected, with each $T_p > 30$ MeV. The incident π^+ energy is 162 MeV.

peak lying on the curve is apparent for the He isotopes. There is strength lying along the line for N, as well as a large peak at low momentum. For the Ar data, the large peak at low momentum and the strength along the line appear to have joined, and are hard to distinguish. The peak lying on the curve is very strong evidence for ISI. Its strength indicates that this mechanism contributes significantly to the cross section for three protons in the final state, and thus to multi-nucleon absorption. This strength appears to be shrinking with increasing A. The signature is smeared because of the larger Fermi-momentum in the heavier nuclei, but this is likely a small effect compared to the fact that other competing channels are becoming more important.

There are two other regions of slightly increased strength visible, at least in the He data. One is around 80° and 650 MeV/c, and the other is around 130° and 450 MeV/c. These correspond to the forward-backward peaks associated with two-nucleon absorption. Their strength is due to some contamination from pure two-nucleon absorption and also from two-nucleon absorption following ISI, or possibly preceding FSI.

At 162 MeV, the data show similar features. At 118 MeV, there are no clear signs of ISI. This appears to be due in part to the proximity of the boundaries and of the low momentum strength. However, for ^3He it appears that an ISI peak would be clearly visible, yet none is seen. This is more evidence consistent with the Δ -dominance argument explaining the features of the multiplicity analysis results.

The presence of the low momentum strength for the N and Ar data obscures the ISI signatures. If the p - θ correlation is replotted with the restriction that the missing energy is less than 75 MeV, this strength vanishes. As the process under examination takes place with the rest of the nucleus acting as a spectator, the three protons are expected to carry the bulk of the energy, and this cut should not remove the ISI signatures. Figures 6-14, 6-15, and 6-16 show the correlation incorporating this restriction.

The largest difference between these figures and the previous set is that the strength in the low momentum region is significantly smaller for 118 and 162 MeV, and has vanished for 239 MeV. The ISI peaks are still strong for the He isotopes, and are now clearly present at the higher pion energies for the N and Ar data as well.

It is possible to form a very rough quantitative estimate of the strength of the contribution of ISI to the fraction of the cross section appearing in the figure; *i.e.*, three detected protons, each with above 30 MeV, and $E_{\text{miss}} < 75$ MeV. This technique used is to integrate the strength under the peak, and then subtract a background determined from the strength in the vicinity

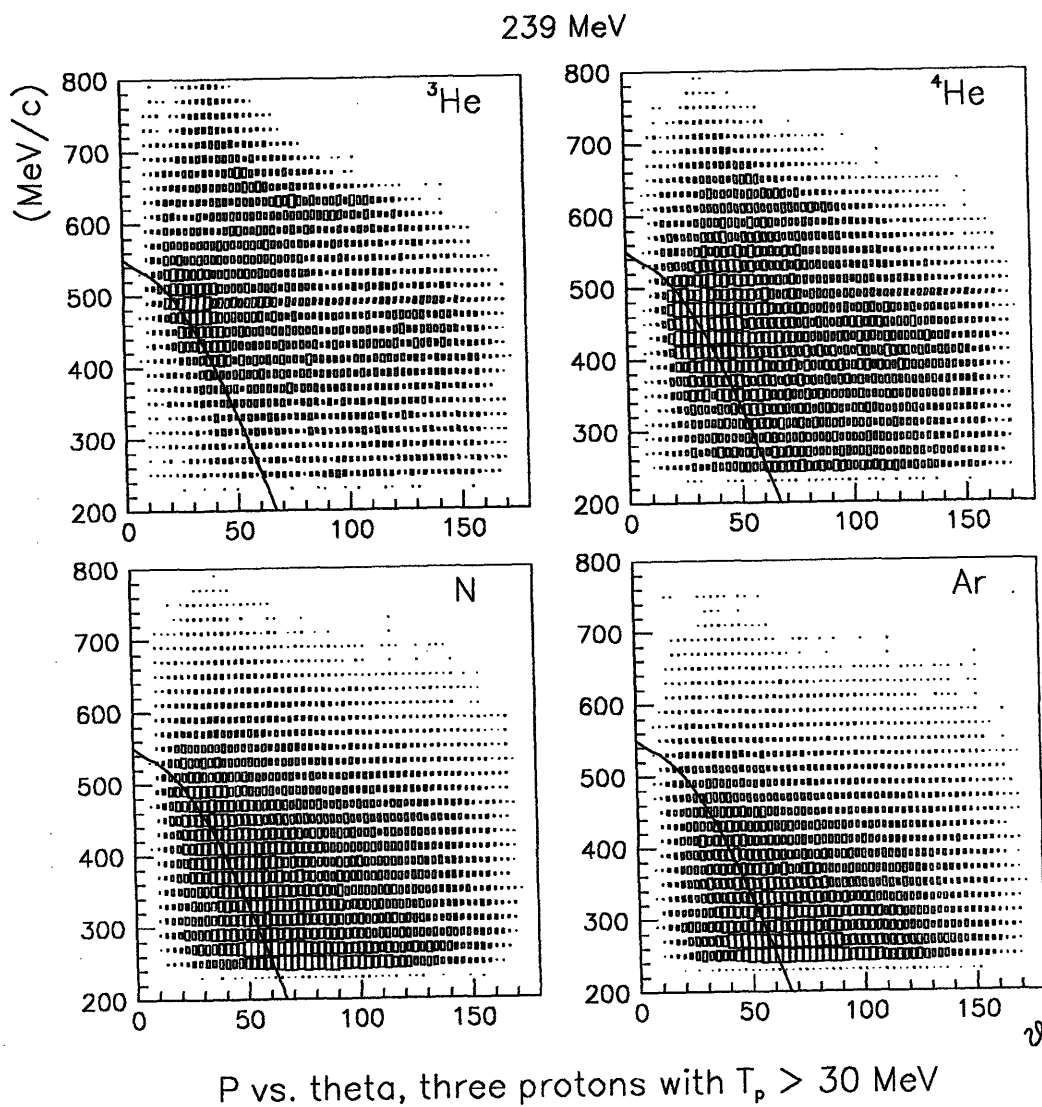


Figure 6-13: The relationship between the momenta and polar angles of the protons for events in which three protons are detected, with each $T_p > 30$ MeV. The incident π^+ energy is 239 MeV.

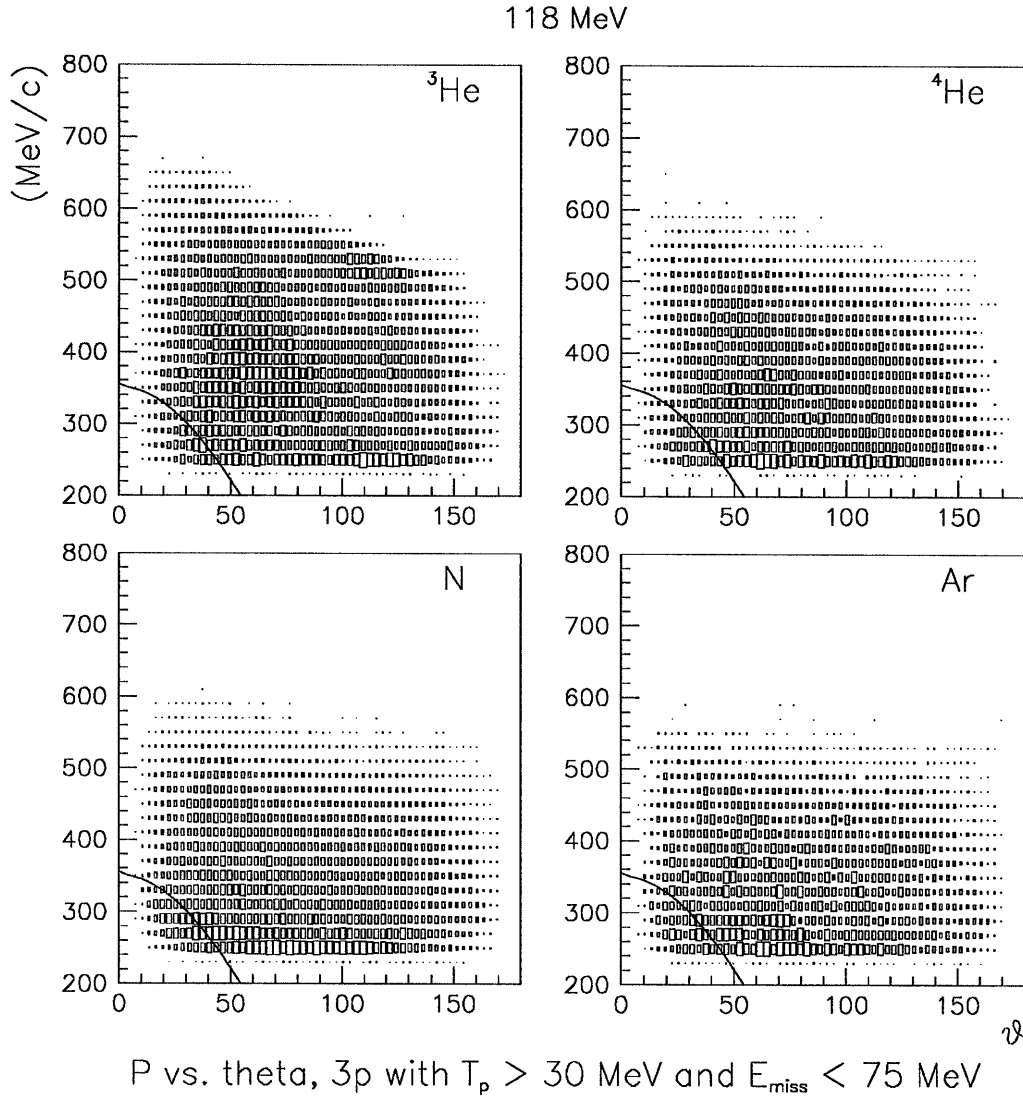


Figure 6-14: The relationship between the momenta and polar angles of the protons for events in which three protons are detected, with each $T_p > 30$ MeV. In addition, $E_{\text{miss}} < 75$ MeV. The incident π^+ energy is 118 MeV.

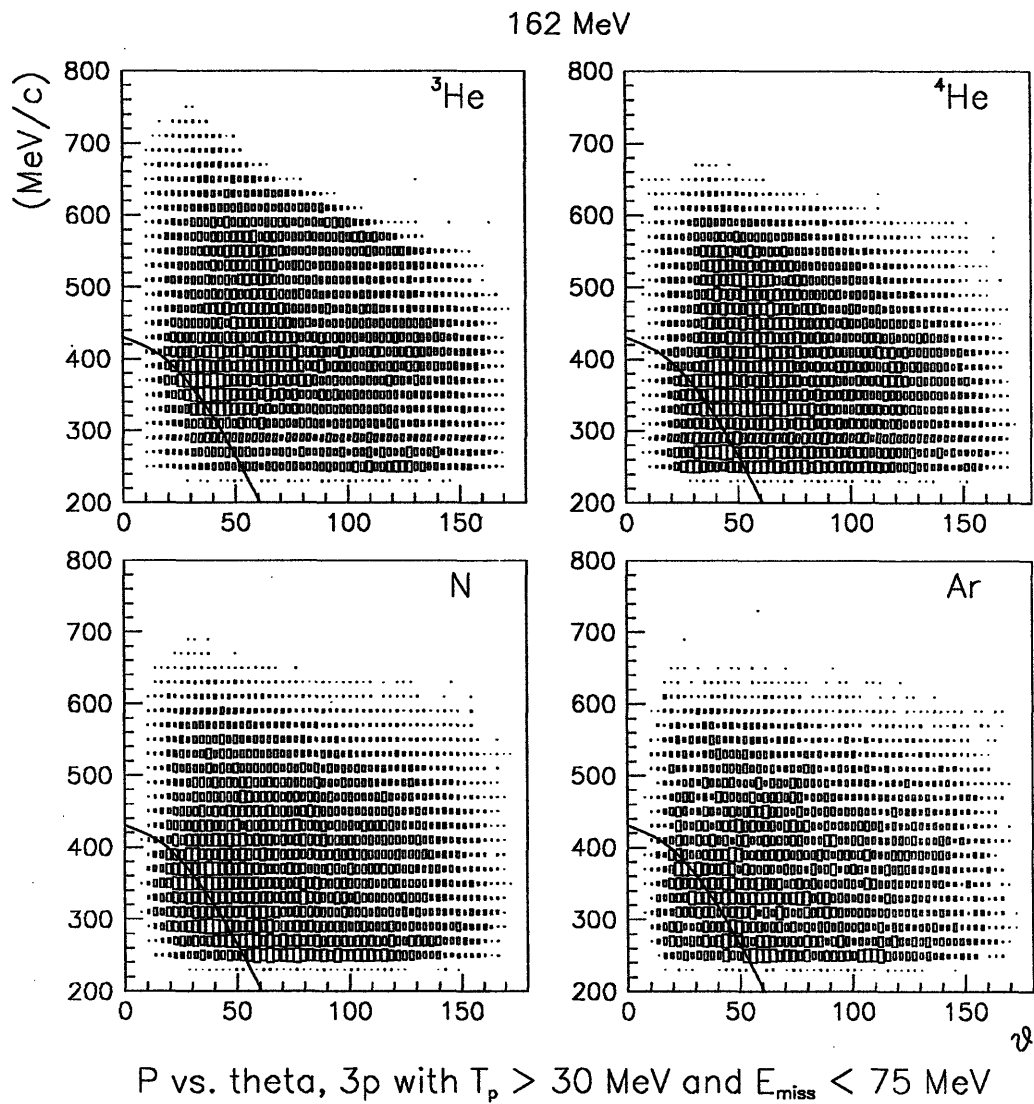


Figure 6-15: The relationship between the momenta and polar angles of the protons for events in which three protons are detected, with each $T_p > 30$ MeV. In addition, $E_{\text{miss}} < 75$ MeV. The incident π^+ energy is 162 MeV.

ISI Contribution			
	118 MeV	162 MeV	239 MeV
^3He	0%	9%	19%
^4He	0%	5%	15%
N	2%	8%	14%
Ar	6%	7%	9%

Table 6.1: Very rough estimates of the fractional contribution of ISI to the strength with three detected protons, each above 30 MeV, and $E_{\text{miss}} < 75$ MeV.

of the peak. Comparing the resulting value to the total strength in the plot (accounting for the fact that each event is plotted three times) gives the fractional contributions reported in table 6.1. As the extent of the peak and the background under it were difficult to measure accurately, these numbers are quite rough, perhaps good to a factor of two.

It is therefore established that ISI plays a role in absorption on all four nuclei. However, only a small portion of the cross section with three energetic protons is attributable to this process. The strength of the signature is increasing with E_π and decreasing with A , although the latter dependence may well be due to the signature being smeared as opposed to decreasing relative strength. For the heavier nuclei, especially Ar, the ISI's signature is dominated by a large peak at very low momentum. When the events with a proton in this peak are examined, it appears that the other two protons have a featureless p - θ correlation, implying these events are not byproducts of two-nucleon absorption unless the pion's direction was essentially randomized before it occurred.

The other signature that will be examined has proven very useful for He, especially ^3He , and very disappointing for the heavier nuclei. It is called the pseudo-invariant mass and was suggested by Salcedo *et al.* [94] to search for ISI. The definition of the pseudo-invariant mass is illustrated in figure 6-17. If a particle is absorbed by two nucleons in the nucleus, then it should be possible to estimate its mass independently of any interactions it had preceding the absorption. This is done by assuming that the two absorbing nucleons are initially at rest, and then calculating the mass of the absorbed particle directly from the momenta and energies of the two final state nucleons. If the particle was an on-shell pion, the pseudo-invariant mass will equal the pion's mass. This result will be smeared by the initial momenta of the absorbing nucleons, as well as by the fact that if an ISI occurred, the intermediate state pion need not be on-shell. If there are three energetic nucleons in the final state, and the pseudo-invariant mass

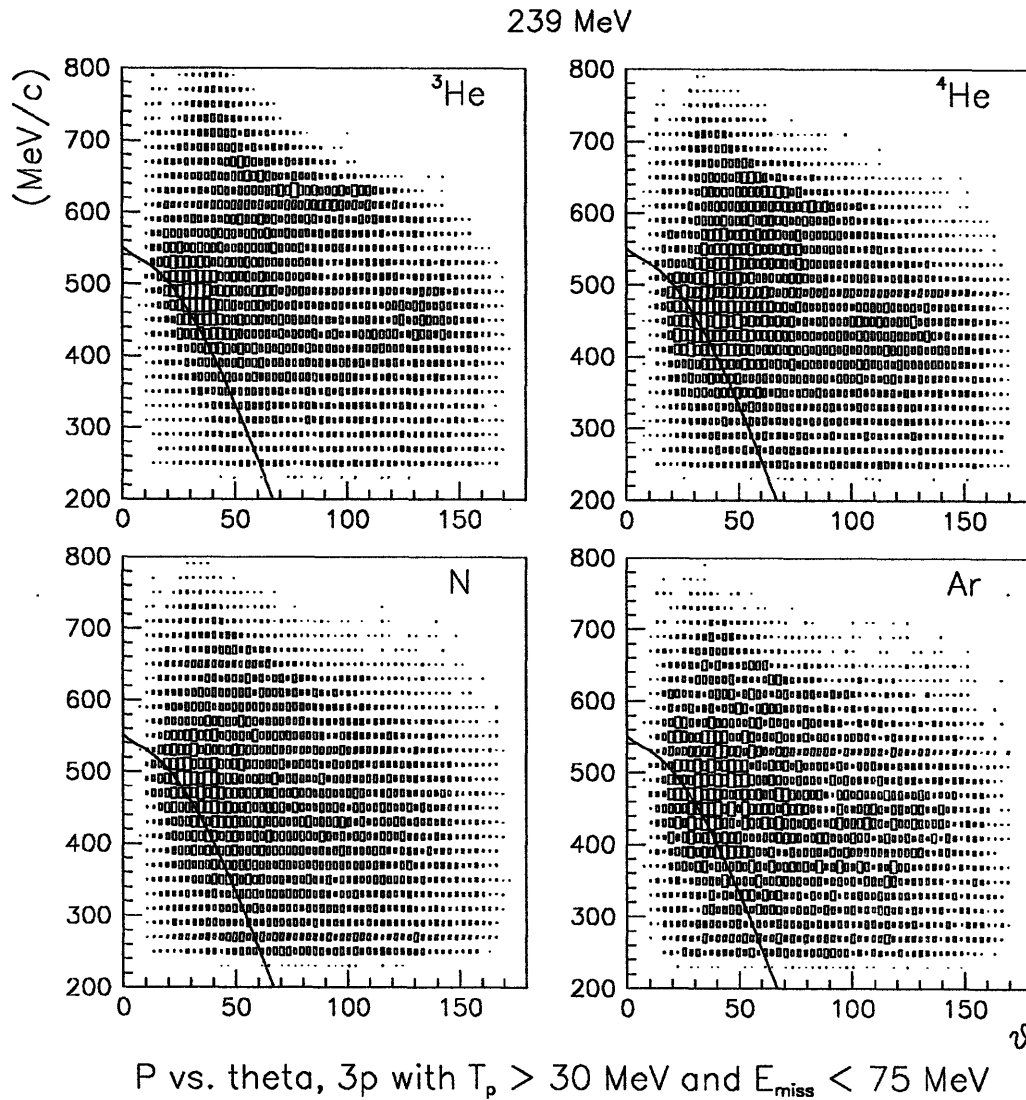
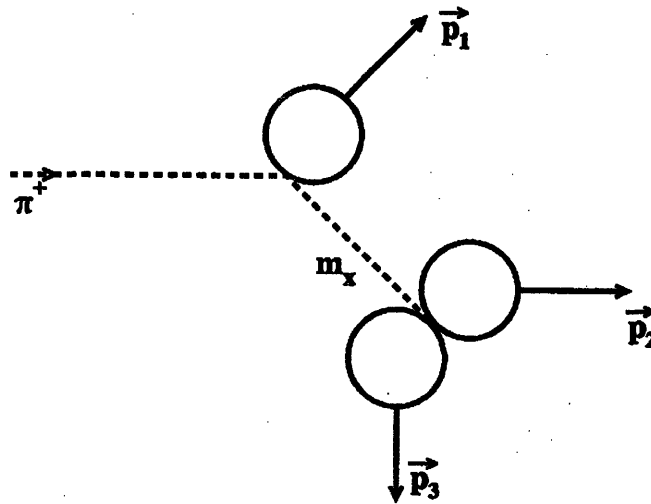


Figure 6-16: The relationship between the momenta and polar angles of the protons for events in which three protons are detected, with each $T_p > 30$ MeV. In addition, $E_{\text{miss}} < 75$ MeV. The incident π^+ energy is 239 MeV.

Pseudo-Invariant Mass



$$\begin{aligned} m_x^2 &= E_x^2 - \vec{p}_x^2 \\ &= (T_2 + T_3)^2 - (\vec{p}_2 + \vec{p}_3)^2 \end{aligned}$$

Figure 6-17: An illustration of the definition of the pseudo-invariant mass.

as calculated from one of the pairs is in the vicinity of the pion mass, then it is likely that an ISI occurred.

Figure 6-18 shows the square of the pseudo-invariant mass for the events with three detected protons, each of which is above 30 MeV. The calculation is performed for each of the three possible proton pairs, and all three results are plotted. When the two protons chosen did not actually absorb a particle, then the pseudo-invariant mass does not correspond to a physical mass, and its value is frequently imaginary. For this reason, it is more convenient to work with the square of the pseudo-invariant mass.

When the spectra are examined, peaks or shoulders in the vicinity of the square of the pion mass are apparent for the ${}^3\text{He}$ data. The peaks are actually at somewhat less than m_π^2 because of the binding energy and the effects of Fermi-momentum. For the heavier nuclei, these signatures are not visible. The assumption that the initial state particles are at rest has failed and any signature is smeared beyond recognition. These spectra have also been plotted for $E_{\text{miss}} < 75$ MeV, but there are no significant changes, so they will not be shown.

6.3.3 The Search for FSI

In hard-FSI, the pion absorbs on a pair of nucleons inside the nucleus, one of which subsequently quasi-elastically scatters from another nucleon. Hence, one can either look for one nucleon that has the characteristics associated with two-nucleon absorption, while two others have significant energy, or for two nucleons that show the characteristics of elastic scattering. In this section, both possibilities will be examined.

Figure 6-19 shows the momentum of a proton which is between 130° and 140° following the absorption of a π^+ when there are three protons detected, each has above 30 MeV, and the missing energy is less than 75 MeV. This corresponds to a one-dimensional slice from the figures 6-14, 6-15, and 6-16. In the scenario where a π^+ is absorbed on a T=0 pair near the surface of the nucleus, the backward moving proton is likely to escape the nucleus undisturbed. The forward proton has to traverse the nuclear medium, and may well undergo a FSI. When this interaction is with another proton, there will frequently be three protons above threshold which carry the bulk of the energy. In addition, the backward proton is undisturbed, and thus should have a correlation between energy and angle similar to two-nucleon absorption. The dashed lines on the figure show the momentum a proton in this angular range would have following absorption on ${}^2\text{H}$. For two-nucleon absorption in a nucleus the peak will be at a lower energy

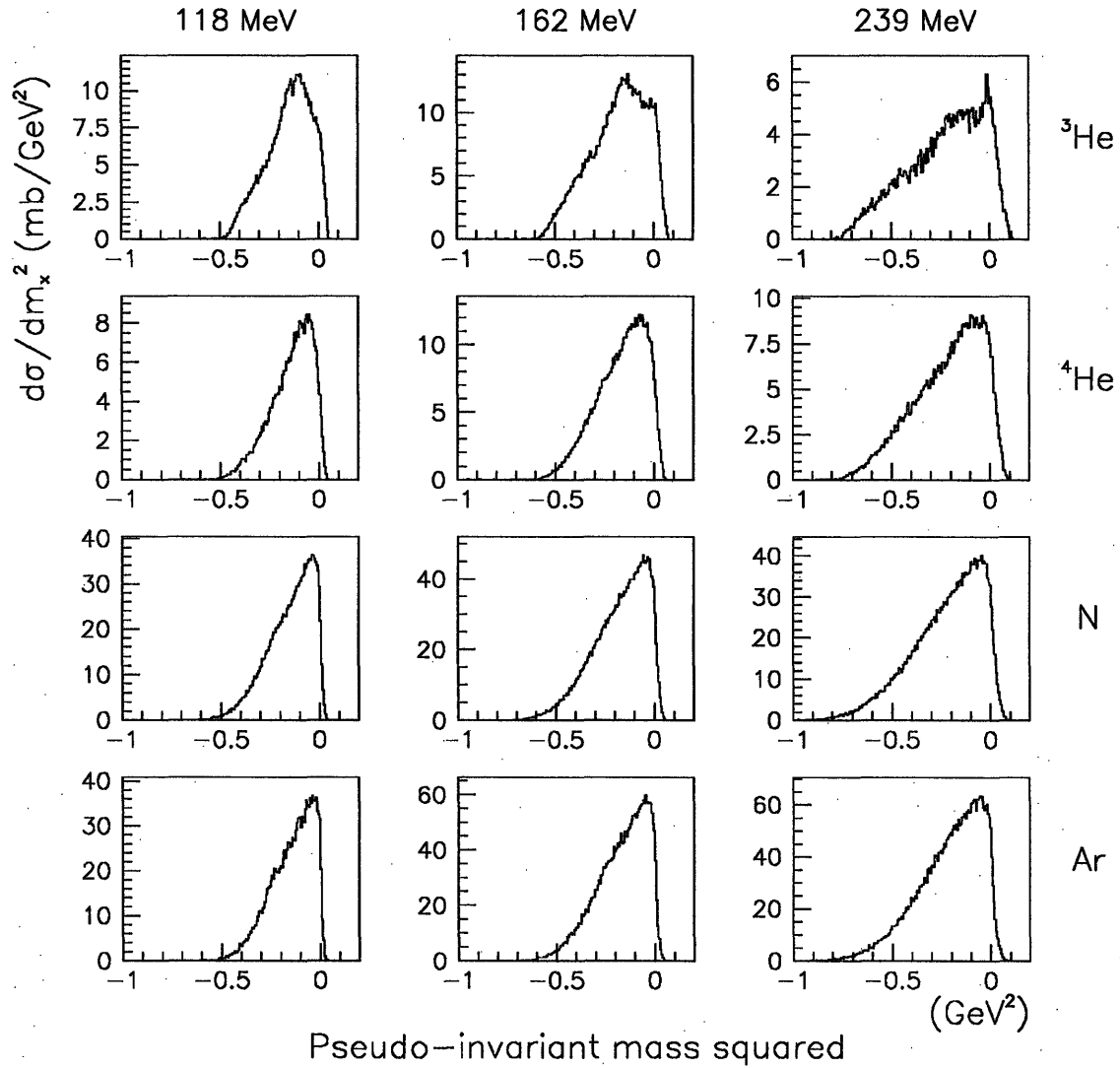


Figure 6-18: The square of the pseudo-invariant mass is shown for events with three detected protons, each over 30 MeV.

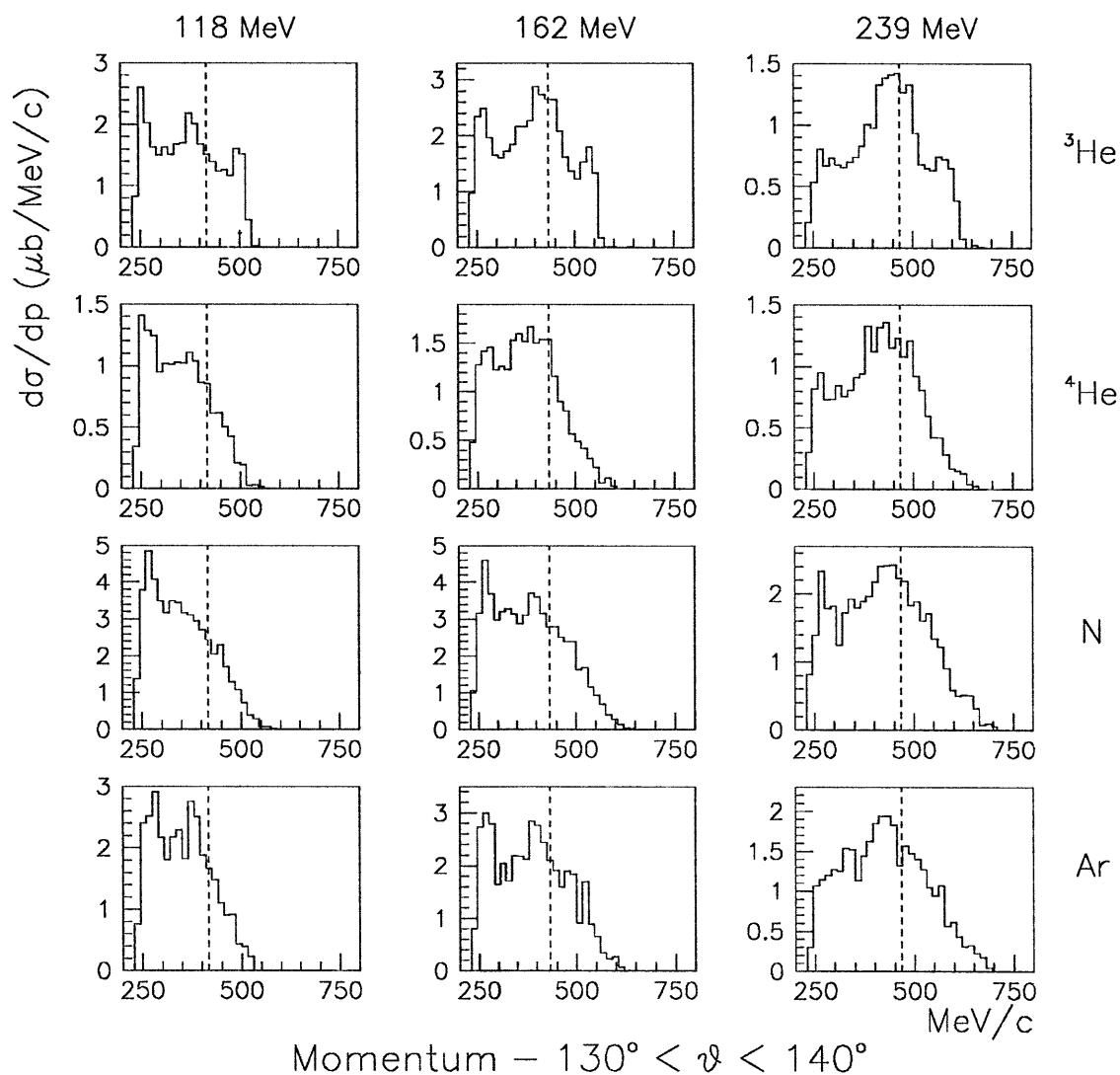


Figure 6-19: The momentum of a proton between 130° and 140° when there are three protons detected, each is over 30 MeV, and $E_{\text{miss}} < 75$ MeV.

because of the potential well, and will be wide due to Fermi-smearing. In fact, clear peaks are seen for almost all the energy-target pairings.

This is an indication of the presence of FSI in the three proton channel. Unfortunately, it is not a clear signature because other processes will give rise to strength in this region. If ISI results in a forward moving pion, then its characteristics will be similar to those of a beam pion, and the absorbing nucleons would have a peak in this region. However, the requirement that the scattered nucleon be over 30 MeV limits the contamination from this process. Also, any contamination from pure two-nucleon absorption where a third proton is above 30 MeV, whether because of its initial momentum or from evaporation, will be in this region. These possible contaminations make this figure difficult to interpret.

Another possible indication of FSI involves the two nucleons involved in the quasi-elastic scattering. When two objects of equal mass elastically scatter, the opening angle between the two momenta will be 90° in a reference frame where one was at rest in the initial state. If the initial momentum is assumed to be zero, the laboratory frame satisfies this requirement. Thus any peak at 90° in a plot of the opening angles would be a signature of FSI. This signature would be smeared by the spread of initial momenta from the Fermi-distribution. Figure 6-20 shows the opening angles when there are three detected protons, each over 30 MeV, and $E_{\text{miss}} < 75$ MeV. Each of the three possible opening angles are plotted for every event. A cursory examination indicates the presence of some minor excess strength in the vicinity of 90° , but the signature is still not clear.

Attempts were made to combine these two observables. First the peaks in figure 6-19 were cut on, then the opening angle between the two other protons was plotted. Unfortunately, the kinematic constraints this imposed on the problem created a peak at 90° for a phase space simulation, so FSI could not be clearly distinguished. Thus, behavior has been seen that would be consistent with the existence of FSI in the multi-nucleon absorption channel. The signatures are not distinct, however, and it cannot be said with certainty that it does exist.

6.4 Conclusions

The absorption of π^+ in the $\Delta(1232)$ -resonance energy region has been examined for ^3He , ^4He , N, and Ar. Total absorption cross sections are reported, along with the breakup into channels with different numbers of energetic final state nucleons. The ^4He , N, and Ar cross sections are

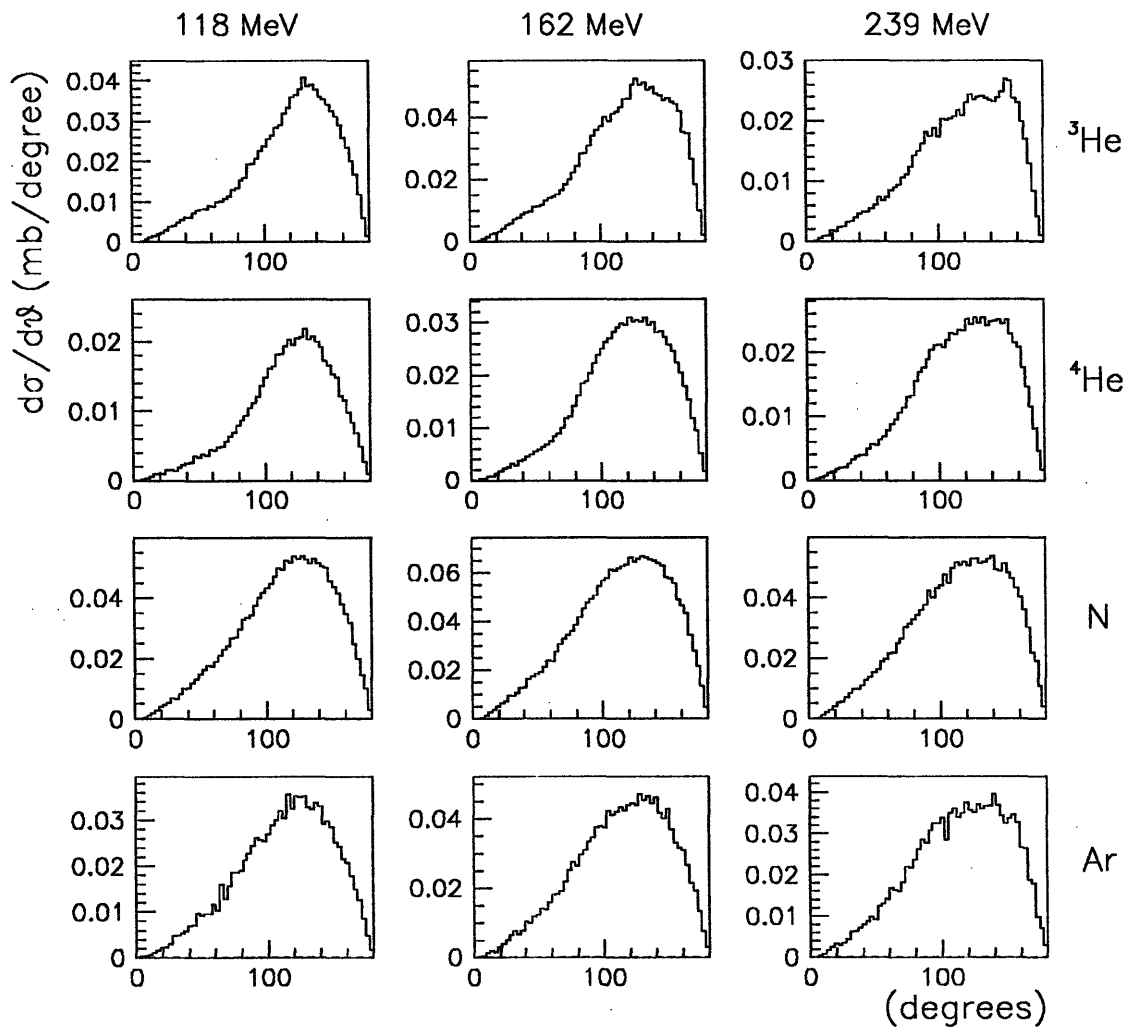


Figure 6-20: The opening angles between each of the three possible pairs of protons when there are three detected protons, each over 30 MeV, and $E_{\text{miss}} < 75$ MeV.

the most precise measurements on nuclei with $A \geq 4$ so far. The methods utilized to extract the total cross sections and multiplicities in this analysis were constrained by the requirement that they be applicable to all nuclei, in particular to N and Ar. Uncertainties associated with the SCX subtraction are minor on these two nuclei, but are significant on He, especially for the 239 MeV data. Other methods of analysis are preferable for ${}^3\text{He}$ and ${}^4\text{He}$, making use of the kinematic completeness available when two or three nucleons are detected. These in-depth examinations are in progress, and give results consistent with those reported here.

It was found that the process leading to two energetic final state protons decreases with increasing pion energy and increasing A from a high of 80% of the total absorption cross section on ${}^3\text{He}$ at 118 MeV to a low of less than 20% on Ar at 239 MeV. The remainder has some contribution from the pn channel, but the bulk has more than two energetic final state nucleons.

The major open question in this field is the identification of the mechanisms responsible for this multi-nucleon strength. The differential spectra presented in this work have demonstrated that there is a contribution from initial state interactions followed by two-nucleon absorption. These are the first significant signatures identified for this important process. However, a rough estimate of the contribution of ISI to ppp final states indicates that it accounts for well under half the strength, even though it should contribute more strongly to this channel than to any others. In addition, indications of the presence of final state interactions were seen. Unfortunately, the signatures for FSI are not clearly separated from the backgrounds, so it proved impossible to estimate the strength of its contribution precisely.

There are some interesting trends in the results of the current multiplicity analysis. The average number of nucleons participating in the absorption process increases with A from 2.2 for ${}^3\text{He}$ to 2.5 for Ar at 118 MeV, from 2.3 to 2.8 at 162 MeV, and from 2.3 to 3.3 at 239 MeV. The fact that this average has a significant increase with A at 239 MeV, while remaining almost constant at 118 MeV, has been explained by the dominance of the Δ -resonance. These numbers are consistent with the results of McKeown *et al.*'s [10] rapidity analysis for the LADS He and N data, but they increase more slowly and are significantly smaller for Ar.

Significant cross sections for four or more energetic nucleons in the final state were found, especially at 239 MeV. The fraction of the total cross section with more than three nucleons was about 20% for ${}^4\text{He}$, 35% for N, and 40% for Ar at this energy. This implies that more complicated processes than two-nucleon absorption preceded by ISI or followed by FSI are occurring. These could involve "new physics" through a multi-nucleon absorption process, or

they could be indications of multiple stage reactions with several initial state interactions and final state interactions. Unfortunately, there are no clear signatures available to differentiate these possibilities in the heavy nuclei. The most promising route is a careful study of the effects of successively adding additional nucleons to the absorbing system, and looking for fundamental changes in the absorption mechanisms.

Another interesting observation is that the number of neutrons participating in the reaction is increasing with A faster than the number of protons. This can be seen by examining the ratios of the pn to the pp final states, and the ppn to the ppp final states. The ratio of pn to pp increases from an average of about 10% on ${}^4\text{He}$, to 30% on N , and to 55% on Ar . The difference between ${}^4\text{He}$ and N is explainable in terms of the increase in the number of initial state nn pairs relative to pn pairs. A possible additional explanation for the increase between N and Ar involves the expected differences in the neutron and proton densities when $Z \neq N$, although one would only expect these variations to be significant for heavier nuclei. For ppn and ppp , the ratio goes from 2.1, to 1.8, to 3.2. The ratio thus has an interesting drop before beginning to increase with A . A possible explanation for this behavior is that following absorption on ${}^4\text{He}$, the two protons from ppn cannot pick up a neutron, so strength is not diverted into a pdn final state.

Clearly the results in this thesis would benefit from a direct comparison with a series of theoretical predictions. Unfortunately, such predictions are lacking except for a few special cases. The development of the theories has been hampered by the absence of accurate, unchanging data. The current abundant supply of precise experimental results provides a basis for new theoretical work.

This thesis has compared the characteristics of the absorption of π^+ on ${}^3\text{He}$, ${}^4\text{He}$, N , and Ar . The questions raised in the introductory chapter about the nature of the absorption mechanisms have been addressed, although the lack of clear, separable signatures has led in some cases to qualitative rather than quantitative conclusions. The existence of a genuine multi-nucleon absorption mechanism is thus still in doubt, as the possibility remains that combinations of already known processes explain the multi-nucleon strength. Further progress on this question will come from ongoing analyses of the differences between absorption on ${}^2\text{H}$, ${}^3\text{He}$, and ${}^4\text{He}$.

Bibliography

- [1] D. Ashery et al. *Phys. Rev.*, **C23**, 2173 (1981).
- [2] E. Moniz *Nucl. Phys.*, **A354**, 535 (1981).
- [3] M. Menon et al. *Phil. Mag.*, **41**, 583 (1950).
- [4] R. Marshak. *Meson Physics*. McGraw-Hill, New York, 1952.
- [5] H. Anderson et al. *Phys. Rev.*, **133**, B392 (1964).
- [6] J. Favier et al. *Nucl. Phys.*, **A169**, 540 (1971).
- [7] E. Bellotti et al. *Nuovo Cimento*, **A18**, 75 (1973).
- [8] H. Ullrich et al. *Phys. Rev. Lett.*, **33**, 433 (1974).
- [9] H. Jackson et al. *Phys. Rev.*, **C16**, 730 (1977).
- [10] R. McKeown *Phys. Rev. Lett.*, **44**, 1033 (1980).
- [11] B. Neganov and L. Parfenov *JETP Sov. Phys.*, **7**, 528 (1958).
- [12] M. Baumgartner et al. *Nucl. Phys.*, **A399**, 451 (1983).
- [13] D. Gotta et al. *Phys. Lett.*, **112B**, 129 (1982).
- [14] A. Altman et al. *Phys. Lett.*, **144B**, 337 (1984).
- [15] G. Backenstoss et al. *Phys. Rev. Lett.*, **55**, 2782 (1985).
- [16] W. Brückner et al. *Nucl. Phys.*, **A469**, 617 (1987).
- [17] R. Schumacher et al. *Phys. Rev.*, **C38**, 2205 (1988).
- [18] T. Altheholz et al. *Phys. Rev. Lett.*, **73**, 1336 (1994).

- [19] N. Gregory. *Pion Single Charge Exchange on the Deuteron*. MSc thesis, Massachusetts Institute of Technology, in preparation.
- [20] K. Wilson. *Pion Absorption on ^3He* . PhD thesis, Massachusetts Institute of Technology, 1995.
- [21] B. Ritchie *Phys. Rev.*, **C44**, 533 (1991).
- [22] H. Yukawa *Proc. Phys. Math. Soc. Japan*, **17**, 48 (1935).
- [23] C. Anderson and S. Neddermeyer *Phys. Rev.*, **50**, 263 (1936).
- [24] M. Conversi et al. *Phys. Rev.*, **71**, 209 (1947).
- [25] C. Lattes et al. *Nature*, **159**, 694 (1947).
- [26] D. Clark et al. *Phys. Rev.*, **83**, 649 (1951).
- [27] R. Durbin et al. *Phys. Rev.*, **83**, 646 (1951).
- [28] J. Hufner *Phys. Reports*, **21**, 1 (1975).
- [29] F. Adelman et al. *Science*, **111**, 226 (1950).
- [30] W. Panofsky et al. *Phys. Rev.*, **81**, 565 (1951).
- [31] G. Bernardini et al. *Phys. Rev.*, **83**, 1075 (1951).
- [32] G. Bernardini and F. Levy *Phys. Rev.*, **84**, 610 (1951).
- [33] E. Fowler et al. *Phys. Rev.*, **91**, 135 (1953).
- [34] H. Bradner and B. Rankin *Phys. Rev.*, **81**, 916 (1951).
- [35] D. Koltun. In M. Baranger and E. Vogt, editors, *Advances in Nuclear Physics*, Vol. 3, pages 71–192. Plenum Press, New York, 1969.
- [36] H. Stadler *Phys. Rev.*, **96**, 496 (1954).
- [37] C. Cohn *Phys. Rev.*, **105**, 1582 (1957).
- [38] A. Sachs et al. *Phys. Rev.*, **109**, 1733 (1958).
- [39] M. Demeur et al. *Nuovo Cimento*, **4**, 509 (1956).
- [40] S. Azimov et al. *JETP Sov. Phys.*, **4**, 632 (1957).

- [41] P. Ammiraju and L. Lederman *Nuovo Cimento*, **4**, 283 (1956).
- [42] P. Fedotov *Sov. J. Nucl. Phys.*, **2**, 235 (1966).
- [43] M. Schiff et al. *Phys. Rev.*, **122**, 225 (1961).
- [44] M. Block et al. *Phys. Rev. Lett.*, **11**, 301 (1963).
- [45] R. Bizzari et al. *Nuovo Cimento*, **33**, 1497 (1964).
- [46] M. Kozodaev et al. *JETP Sov. Phys.*, **11**, 300 (1960).
- [47] Y. Budagov et al. *JETP Sov. Phys.*, **15**, 824 (1962).
- [48] K. L. Couteur *Proc. Phys. Soc.*, **A63**, 259 (1950).
- [49] K. L. Couteur *Proc. Phys. Soc.*, **A65**, 718 (1952).
- [50] B. Anafasev and V. Ostroumov *Sov. J. Nucl. Phys.*, **1**, 463 (1965).
- [51] S. Ozaki et al. *Phys. Rev. Lett.*, **4**, 533 (1960).
- [52] M. Baladin et al. *JETP Sov. Phys.*, **19**, 27 (1964).
- [53] M. Nordberg et al. *Phys. Rev.*, **165**, 1096 (1968).
- [54] P. Fowler *Proc. Phys. Soc.*, **85**, 1051 (1965).
- [55] G. Charpak et al. page 465. Academic Press, New York, 1967.
- [56] Bressani *Nucl. Phys.*, **B9**, 427 (1969).
- [57] T. Witten et al. *Phys. Rev.*, **174**, 1166 (1968).
- [58] A. Vaisenberg et al. *JETP Sov. Phys.*, **20**, 854 (1965).
- [59] I. Shapiro and V. Kolybasov *JETP Sov. Phys.*, **17**, 185 (1963).
- [60] V. Kolybasov *Sov. J. Nucl. Phys.*, **3**, 535,704 (1966).
- [61] S. Treiman and C. Yang *Phys. Rev. Lett.*, **8**, 140 (1962).
- [62] C. Lazard et al. *Nuovo Cimento*, **A63**, 1001 (1969).
- [63] C. Ingram *Nucl. Phys.*, **A374**, 319c (1982).
- [64] R. Redwine *Nucl. Phys.*, **A434**, 239c (1985).

- [65] D. Ashery and J. Schiffer *Ann. Rev. Nucl. and Part. Sci.*, **36**, 207 (1986).
- [66] H. Weyer *Phys. Reports*, **195**, 295 (1990).
- [67] T. Ericson and W. Weise. *Pions and Nuclei*. Clarendon Press, Oxford, 1988.
- [68] D. Ashery et al. *Phys. Rev. Lett.*, **47**, 895 (1981).
- [69] G. Backenstoss et al. *Phys. Lett.*, **137B**, 329 (1984).
- [70] A. Altman et al. *Phys. Rev.*, **C34**, 1757 (1986).
- [71] R. Tacik et al. *Phys. Rev.*, **C32**, 1335 (1985).
- [72] R. Tacik et al. *Phys. Rev.*, **C40**, 256 (1989).
- [73] K. Aniol et al. *Phys. Rev.*, **C33**, 1714 (1986).
- [74] W. Burger et al. *Phys. Rev. Lett.*, **57**, 58 (1986).
- [75] W. Burger et al. *Phys. Rev.*, **C41**, 2215 (1990).
- [76] G. Backenstoss et al. *SIN Proposal R 87-13.1* (1987).
- [77] B. Ritchie et al. *Phys. Rev.*, **C30**, 969 (1984).
- [78] M. Steinacher et al. *Nucl. Phys.*, **A517**, 413 (1990).
- [79] P. Weber et al. *Phys. Rev.*, **C43**, 1553 (1991).
- [80] S. Mukhopadhyay et al. *Phys. Rev.*, **C43**, 957 (1991).
- [81] S. Hyman et al. *Phys. Rev.*, **C41**, R409 (1990).
- [82] D. Mack et al. *Phys. Rev.*, **C45**, 1767 (1992).
- [83] F. Adimi et al. *Phys. Rev.*, **C45**, 2589 (1992).
- [84] R. Ransome et al. *Phys. Rev.*, **C45**, R506 (1992).
- [85] R. Ransome et al. *Phys. Rev.*, **C46**, 273 (1992).
- [86] M. Jones et al. *Phys. Rev.*, **C48**, 2800 (1993).
- [87] Bicron Corporation, 12345 Kinsman Road, Newbury, Ohio 44065.
- [88] Dornier Ltd., P.O. Box 1420, D-88039 Friedrichshafen, Germany.

- [89] R. Madey et al. *Nucl. Inst. and Meth.*, **151**, 445 (1978).
- [90] W. Leo. *Techniques for Nuclear and Particle Physics Experiments*. Springer-Verlag, New York, 1987.
- [91] L'Air Liquide (Firm). *Encyclopedie des Gaz*. Elsevier, Amsterdam and New York, 1976.
- [92] M. Wang. *Inclusive Pion Single Charge Exchange in ^4He in the Δ -Resonance Region*. PhD thesis, Massachusetts Institute of Technology, 1994.
- [93] D. Ashery et al. *Phys. Rev.*, **C30**, 946 (1984).
- [94] L. Salcedo et al. *Phys. Lett.*, **B208**, 339 (1988).